Earth and Planetary Science Letters 570 (2021) 117066

Contents lists available at ScienceDirect

Earth and Planetary Science Letters

www.elsevier.com/locate/epsl

The 2019 Ridgecrest, California earthquake sequence: Evolution of seismic and aseismic slip on an orthogonal fault system

Han Yue [a,b,*], Jianbao Sun [c], Min Wang [c], Zhengkang Shen [a,d], Mingjia Li [a], Lian Xue [a], Weifan Lu [a], Yijian Zhou [a], Chunmei Ren [a], Thorne Lay [e]

[a] School of Earth and Space Sciences, Peking University, Beijing 100871, China
[b] Hongshan Geophysical National Observation and Research Station, Peking University, Beijing 100871, China
[c] State Key Laboratory of Earthquake Dynamics, Institute of Geology, China Earthquake Administration, Beijing 100029, China
[d] University of California, Los Angeles, CA, 90095-1567, USA
[e] University of California Santa Cruz, Santa Cruz, CA, 95064, USA

ARTICLE INFO

Article history:
Received 26 September 2020
Received in revised form 1 June 2021
Accepted 16 June 2021
Available online xxxx
Editor: J.-P. Avouac

Dataset link:
https://doi.org/10.7909/C3WD3xH1

Keywords:
Ridgecrest Earthquake
co-seismic/afterslip models
seismic and aseismic slip

ABSTRACT

Cascade-up and/or slow-slip processes are commonly believed to control interactions between foreshocks, mainshocks and aftershocks, but their relative contributions remain poorly resolved. Discrimination between these processes will shed light on the understanding of earthquake physics, which requires exceptional observations of earthquake sequences. The well-recorded July 2019 Ridgecrest, California foreshock-mainshock-aftershock earthquake sequence provides such an opportunity. We perform simultaneous inversion of the July 4th M_W 6.4 foreshock and July 5th M_W 7.1 mainshock kinematic rupture models using SAR, strong motion, and GPS data. We also invert for afterslip models following the M_W 6.4 foreshock and the mainshock, respectively, by developing an inversion method that utilizes strainmeter, SAR and daily GPS time series. The inversion results show that the overall sequence involves no less than six fault segments, which include a main northwest-trending fault and secondary faults with sub-parallel and orthogonal geometry to the main fault. Co-seismic slip and afterslip have complementary patterns on the faults. During the early post-seismic period following the M_W 6.4 foreshock and the mainshock, moment release on the southwest-trending fault is dominated by aseismic slip, in contrast to the predominantly seismic slip on the northwest-trending fault. The mainshock appears to be triggered by a cascade migration of foreshocks on a northwest-trending fault. Slip on the southwest-trending fault migrates from the fault junction at the northeast end (following the M_W 6.4 foreshock) to the southwest end (following the mainshock) during the afterslip interval. The dual-mode (seismic versus aseismic) slip phenomena appear to be driven by co-seismic stress changes produced by the major events.

1. Introduction

Earthquakes are almost always followed by smaller earthquakes (aftershocks), and some earthquakes are preceded by smaller events (foreshocks) (e.g., Jones and Molnar, 1979; Trugman and Ross, 2019; Ende and Ampuero, 2020). Foreshock sequences are a precursory phenomenon that could potentially be used to forecast the mainshock occurrence, yet the triggering mechanism is not fully understood. The behavior of foreshock sequences can be classified into two end-member groups, i.e. the "cascade-up" model and the "slow-slip model". From an observational perspective, the cascade-up model assumes "earthquakes produce earthquakes", and emphasizes stress interactions between adjacent foreshocks, that finally lead to the rupture of the mainshock (e.g., Ellsworth and Bulut, 2018; Yoon et al., 2019). The slow-slip model assumes that "slow-slip produces earthquakes" (Dieterich, 1979) and identifies stress loading by slow-slip as the dominant process driving foreshocks, which in turn provide indicators of the slow-slip (e.g., Kato et al., 2012). In practice, afterslip following a large foreshock can act as a slow-slip process driving the foreshock sequence, even if no slow-slip preceded the first foreshock. In laboratory experiments, both contributions can be important for controlling the occurrence time of a mainshock (McLaskey, 2019). The accumulated case studies of earthquake sequences over the past few decades suggest that both foreshock processes can operate and may comparably account for basic seismic and geodetic observations (Ruiz et al., 2014; Schurr et al., 2014). However, it is generally

* Corresponding author at: School of Earth and Space Sciences, Peking University, Beijing 100871, China.
E-mail address: yue.han@pku.edu.cn (H. Yue).

https://doi.org/10.1016/j.epsl.2021.117066
0012-821X/

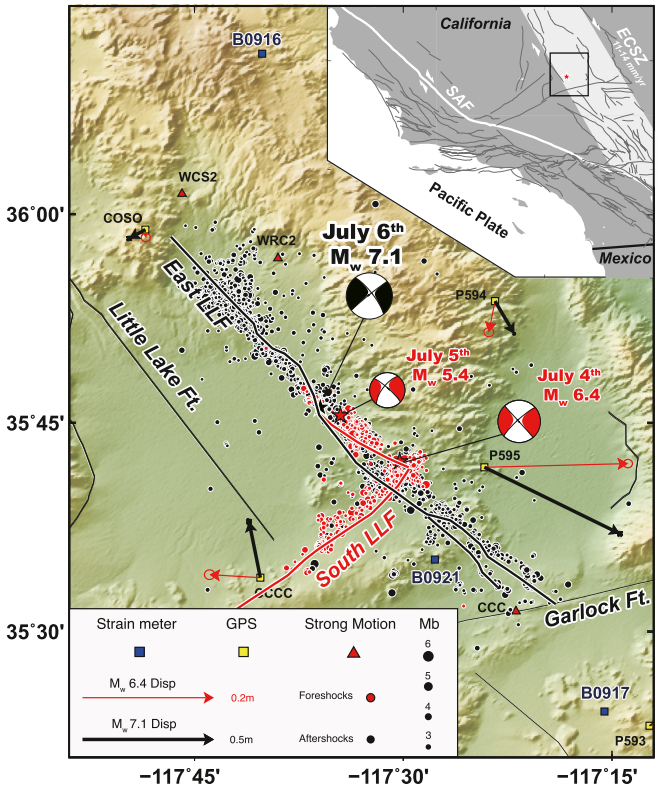

Fig. 1. Regional tectonic map and earthquake information. GCMT solutions for the M_W 6.4 and 5.4 foreshocks and the mainshock are plotted with red- and black-filled focal mechanisms, respectively. Foreshocks and aftershocks are plotted with red- and black-filled circles, respectively. Identified foreshock and mainshock fault traces are plotted as red and black curves, respectively. Strainmeters (blue squares), GPS (yellow squares), and strong motion stations (red triangles) are plotted. GPS horizontal displacements of the M_W 6.4 foreshock and the mainshock are plotted in red and black arrows, respectively. Regional faults are plotted as black curves and labeled. The regional tectonic map for southern California is plotted on the top right. The main figure area is indicated by a black box. The Eastern California Shear Zone (ECSZ) is indicated by a white swath. The northwest-trending fault is now called the Eastern Little Lake Fault (East LLF), and the southwest trending fault is now called the Southern Little Lake Fault (South LLF). (For interpretation of the colors in the figure(s), the reader is referred to the web version of this article.)

difficult to discriminate the contribution of either mechanism for specific earthquake interactions.

Here, we study the July 2019 Ridgecrest, California (RC) earthquake sequence, which involved a foreshock sequence rupture of two mutually perpendicular faults. Exceptional data indicate that during the foreshock sequence, both cascade-up and slow-slip processes occurred, but distinctly on the orthogonal faults. The cascade process appears to have been the dominant mechanism involved in mainshock triggering along the primary fault system, while the slow slip process (afterslip of the largest foreshock; no earlier slow slip has been detected) is the dominant mechanism driving deformation and aftershocks on the perpendicular fault.

The RC sequence (Fig. 1) initiated with an M_W 6.4 foreshock, followed by numerous aftershocks, including an M_W 5.4 event that occurred to the northwest of the foreshock epicenter with ~ 19-hour delay. The M_W 7.1 mainshock occurred near the M_W 5.4 hypocenter ~ 15 hours later. The mainshock is the largest earthquake in California in the last 20 years. The Ridgecrest earthquake caused an economic loss of about five billion dollars (Hough et al., 2020). The three largest events have strike-slip focal mechanisms consistent with a right-lateral sense of offset for a northwest-striking fault. The aftershock distribution indicates the overall rupture extent and demonstrates that the M_W 6.4 foreshock likely ruptured two orthogonal faults, while the mainshock occurred on a ~ 50 km long NW-trending segmented fault system.

The seismogenic faults are situated in the Indian Wells Valley in eastern California, and the two orthogonal faults, which were not recognized prior to the 2019 sequence, are now named the NW-trending Eastern Little Lake and SW-trending Southern Little Lake faults. These faults are among an ensemble of faults in the Eastern California Shear Zone (ECSZ), which is a deformation belt ~ 100 km wide extending from the Mojave Desert in southern California to northwestern Nevada (Dokka and Travis, 1990; Savage et al., 1990; Unruh et al., 2003). Dextral shear motion of ~ 11-14 mm/yr has been measured by GPS across this part of the ECSZ, but the strain is broadly distributed in the deformation zone, and its partitioning among faults has been a subject of investigation (e.g., Gan et al., 2000; McClusky et al., 2001; Miller et al., 2001). No anomalous strain gradient had been detected previously across the two faults involved in the RC sequence, which were only partially mapped before this event.

Rupture processes of the RC earthquake sequence have been investigated using seismic and geodetic observations jointly or separately, (e.g., Chen et al., 2020; Goldberg et al., 2020; Liu et al., 2019; Magen et al., 2020; Ross et al., 2019; Wang et al., 2020). Because the foreshock and mainshock deformation is mingled in SAR images, it is challenging to incorporate this high-resolution data in the joint inversion. Wang et al. (2020) and Chen et al. (2020) used similar strategies, which invert for one major event first and then invert for the other event using the remnant displacement field. Magen et al. (2020) and Goldberg et al. (2020) concatenate Green's functions of the mainshock and foreshock in a uniform matrix and perform simultaneous inversion using SAR and optical images and static GPS data, while seismic data are also used by Goldberg et al. (2020). The interactions between foreshock co-seismic slip, afterslip and seismic events following the M_W 6.4 foreshock, and the mainshock can shed light on earthquake physics, and require an integrated analysis of the slip processes. We perform simultaneous linear inversion to resolve the kinematic rupture process of both major events by the joint use of GPS, SAR, and strong motion observations. We consider the afterslip following the M_W 6.4 foreshock and mainshock as quasi-static processes and develop a linear inversion method to invert for the temporal evolution. The relationship between these processes and associated physics in this complicated fault system is discussed.

2. Data and methods

2.1. Fault model construction

The RC earthquake sequence occurred in a densely instrumented area of California. Seismic waves from the M_W 6.4 foreshock and the M_W 7.1 mainshock ruptures were recorded by regional strong-motion and high-rate GPS (hr-GPS) stations, and cumulative static displacements of the sequences were captured by daily GPS and synthetic aperture radar (SAR) measurements. For performing linear inversions for space-time slip distributions a predetermined fault geometry is required to calculate Green's functions. Alternatively, geometrical fault parameters also need to be inverted using a non-linear approach. In this study, we adopt a similar strategy to Yue et al. (2017), relying on surface fault traces and depth distribution of aftershocks to parameterize a multi-segmented and curved fault system used in linear inversions.

The SAR satellites scan the ground periodically, and the deformation that occurs between two scans can be derived from the data, providing the highest spatial resolution among all available data. For the RC earthquake sequence, all SAR measurements were made before the foreshock and after the mainshock, such that the interferograms depict the superimposed co-seismic displacement

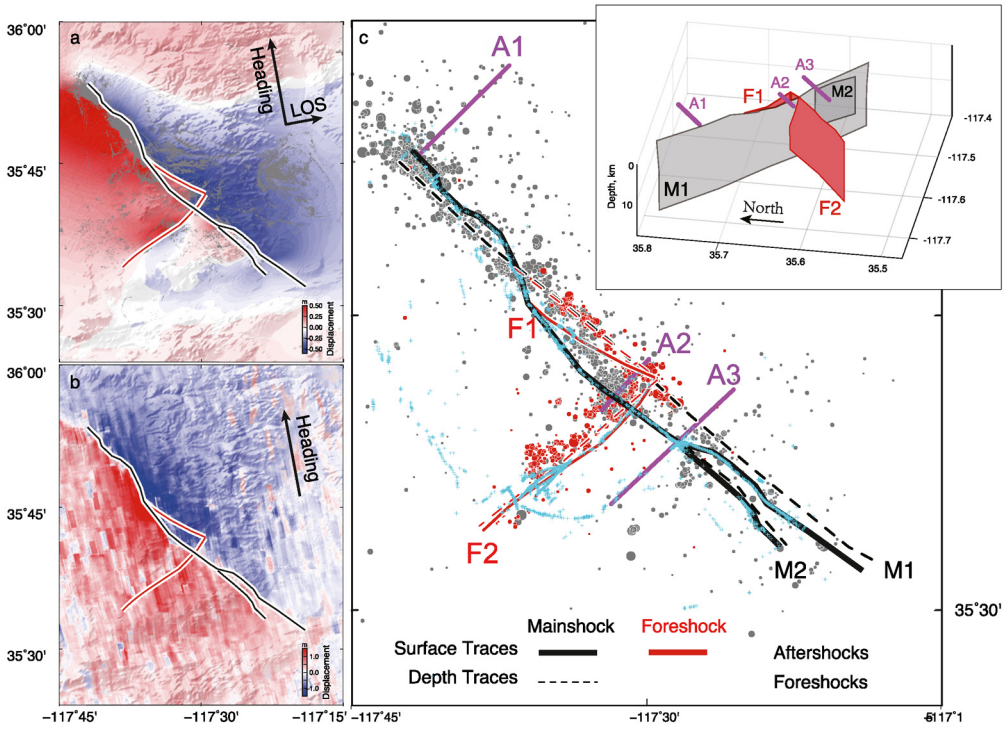

Fig. 2. Fault surface trace and 3D geometry. **a, b** Example **A064** S1 ascending SAR interferogram and azimuth offset data (see Fig. S2 for additional data). The cumulative deformation in the interferometric pair date from July 4 to July 10 (Table S1) displacement field projected to the SAR Line-of-Sight and heading direction is plotted with a blue to red color scale. The satellite heading and look directions are plotted with black arrows. **c.** Foreshocks and aftershocks are plotted as magenta and gray filled circles, respectively. In all three panels, surface fault traces are plotted as red and black curves, respectively. Field-observed surface ruptures are marked as cyan crosses. Deep edges of the foreshock and mainshock faults are plotted as red and black dashed curves, respectively. Inferred 3D fault planes are plotted as red and gray filled planes in the top-right inset.

field of the foreshock, the mainshock, and their early aftershocks, along with any aseismic slip during the interferometric pair dates (see Table S1). We use both the C-band SAR data from Sentinel-1 (S1) satellites of the European Space Agency (ESA) and the L-band PALSAR-2 data of ALOS-2 satellite from the Japanese Aerospace Exploration Agency (JAXA). Interferometry (Strozzi et al., 2008) and offset tracking (Leprince et al., 2007) methods were used to process SAR images to obtain co-seismic ground deformation. Surface rupture traces are manually picked from azimuth-offset images. Details of SAR data processing are described in the supplementary materials. Surface ruptures measured by field investigation (DuRoss et al., 2020) are consistent with the surface offsets depicted by SAR images (Fig. 2).

The observed surface offsets are used to parameterize the fault model; however, many smaller features may be very shallow secondary fractures triggered by the mainshock. Including these trivial structures provides very limited information about the mainshock rupture and expands the model space to explore, which is inconvenient for inversion and parameter tuning. We desire the fault model to capture the primary rupture pattern without emphasizing secondary surface ruptures to keep the slip model relatively simple and representative of the robust faulting at depth. Three criteria are considered when dismissing secondary fault traces:

(1) traces less than 5 km long.
(2) traces located further than 5 km from the main rupture trace.
(3) traces lacked seismicity lineation.

Following these criteria, we identify four major surface rupture traces from field observations and SAR images and use them to parameterize the fault model. We consider these four traces as primary fault segments hosting the foreshock and mainshock (Fig. 2).

We use seismicity locations to determine fault geometries at depth. The catalog of Shelly (2020) is used to construct the fault model and calculate seismic moment release since it is the first catalog available to us. We assume the foreshock occurred on two fault segments F1 and F2 (Fig. 2), both showing about 10 km lateral extent and forming an orthogonal structure. The mainshock aftershocks cover a larger lateral extent (∼ 30 km). The mainshock involves two NW-SE trending faults M1 and M2, where M2 is a smaller branch at the southeast end of M1. The surface trace of segment M1 is curved in its central segment, but its profile at depth is relatively straight.

Two additional fault planes, A1 and A2, are included in the afterslip model with respect to the observed offsets on the ground surface. They are connected to fault M1 at its northwestern end and cut M1 in the center (Fig. 2), respectively. The main fault plane (M1) extends to 29 km depth for afterslip modeling, in comparison with a shallow depth limit (20 km) for the co-seismic fault model. This parameterization allows us to explore deep afterslip beneath the seismogenic depth. Details of the fault geometry are documented in the supplementary materials (Table S3), and the detailed sub-fault parameters are provided in the inversion results. Several studies include segment A2 in the kinematic rupture process inversion, e.g., Ross et al. (2019), Wang et al. (2020), and Goldberg et al. (2020). Seismicity on A2 was most active during the aftershock sequence rather than in the foreshock sequence, indicating that this structure was activated by the mainshock rupture. In comparison with the extended slip on M1 and M2 during the mainshock, this short structure is not a significant feature. Thus we do not include this segment in our co-seismic slip model.

2.2. Joint inversion of M_W 6.4 foreshock and mainshock rupture processes

We conduct a joint inversion for the kinematic rupture process of the foreshock and mainshock. Eight SAR images obtained by interferometry, range-offset, and azimuth offset of Sentinal-1 and

ALOS2 satellite are used in the joint inversion. Because the time intervals of these SAR images span the occurrence of both M_W 6.4 and 7.1 events, they depict the cumulative ground deformation produced by both major events. We also use static and high-rate GPS data in the joint inversion technique. Three-component ground displacements of 31 and 42 static GPS stations are used to invert for the foreshock and mainshock co-seismic slip distributions, respectively. Three-component ground displacement time series from 5 and 20 hr-GPS stations are used to constrain the rupture processes of the foreshock and mainshock, respectively. The original displacement time-series are converted to velocities before use in the inversion algorithm. The velocity waveforms are band-pass filtered with corner frequencies of 0.02 and 0.25 Hz, and cut with 50 s long time-windows starting at the earthquake initial time at one sps interval. We also use three-component acceleration recordings from 10 strong-motion stations and calculate ground velocity waveforms by integrating the original data. The strong motion data are filtered between 0.05 and 0.25 Hz. Details of data processing and visualization are available in the supplementary materials.

Joint use of SAR, GPS and seismic data exploits their respective resolution of different source rupture features, and thus can provide a more robust slip model (Yue et al., 2020). However, it is not straightforward to directly adopt all data types in the inversion because the displacement fields of the M_W 6.4 foreshock and the M_W 7.1 mainshock are superimposed in the SAR images, yet separated in the GPS and kinematic observations. Based on a traditional multi-time-window inversion algorithm (Hartzell and Heaton, 1983), we design a linear inversion algorithm to simultaneously invert for the foreshock and mainshock space-time slip evolution using the above available data. This algorithm uses respective static and kinematic data to constrain the rupture process of individual events, while still keeping summation of their co-seismic displacements to be consistent with the SAR observations. We parameterize the ruptured faults as the foreshock and mainshock segments and then calculate Green's functions of each observation for the inversion parameters. Green's functions of the foreshock and mainshock are concatenated at diagonal locations of the inversion matrix to enable respective fits to GPS and strong motion data of either event, while SAR Green's functions are concatenated in the row direction to account for the cumulated contribution to the SAR observations. This inversion design is similar to that used by previous studies (Yue et al., 2017; Goldberg et al., 2020; Magen et al., 2020). Details of the inversion matrix design and relative data weighting are described in detail in the supplementary materials. The mainshock hypocenter is set at 3 km depth, as reported by Shi et al. (2019), who calibrated the initial arrival time using a regional event. The choice of hypocenter depth at 3 km does not influence the slip model significantly, but improves waveform fits to the initial strong-motion arrivals relative to deeper positions. We also incorporate damping operation for slip spatial roughness and boundary slips. The boundary damping reduce slips near the fault side and bottom edges, where model resolution is relatively low. Although slips on most boundaries are cleaned by the boundary damping, we consistently resolve some slips at the bottom of F2 near its junction side under the same damping level. This phenomenon indicates such rupture patch may be required to fit data, while more studies are needed to discuss its implication for rupture dynamics.

2.3. Strainmeter time series of deformation following the M_W 6.4 foreshock

To investigate the triggering mechanism between the M_W 6.4 foreshock and the mainshock, we make use of the regional strainmeter recordings to resolve the slip process during this period. The slip that occurred between the M_W 6.4 foreshock and the mainshock is comprised of both seismic slip (additional foreshocks) and aseismic afterslip. Resolving slow slip evolution requires ground deformation measurements that capture quasi-static responses to fault slip recorded at a high temporal sampling rate. This requirement excludes the use of seismic and SAR data for this purpose. We also do not find GPS displacement signals above the noise level in the period between the M_W 6.4 foreshock and the mainshock (as also reported by Wang et al., 2020). Fortunately, the deformation during the foreshock sequence was clearly recorded by near-field strainmeter stations (Fig. 1). Station B0916 is located north of F1, and station B0921 is close to F2; thus, their strain measurements are primarily sensitive to the slip history of F1 and F2, respectively. Each strainmeter records time series of 3 plane strain components of the full 6 component strain tensor, e; $\varepsilon_{ee}, \varepsilon_{nn}$, *and* ε_{en}. The plane strain tensors are shown as rotated "cross" symbols in Fig. 4, which depict pairs of eigenvalues oriented in the directions of orthogonal eigenvectors. We use three stations including B0916 and B0921 to analyze the slow-slip process following the M_W 6.4 foreshock.

The data from B0916 clearly show several sharp jumps. In contrast, the time series at B0921 show a smooth logarithmic decay (Figs. 4 and 5). Considering the locations of B0916 and B0921, these time series data suggest that deformation on F1 and F2 following the M_W 6.4 foreshock may be dominated by episodic "cascade slip" and steady "slow slip", respectively (Fig. 1). We isolate strain jumps caused by the M_W 5.4 event in the two strainmeter observations, and use a point source focal mechanism to predict similar strain tensors to the observations as a test. We also perform a linear inversion for slip distribution on F1, which estimates an M_W 5.36 event at the northwest end of F1, consistent with the actual M_W 5.4 event location (Fig. S20). The reasonable results found for that event give us confidence to use the strain observations to quantitatively determine the overall deformation process including any slow-slip. We adopt the full time series inversion method to these strainmeter data to investigate the afterslip following the M_W 6.4 foreshock. Details of the inversion method are presented in later sections.

2.4. Observations of post-seismic deformation

We also investigate the afterslip process that occurred within six months after the mainshock (July 6th - Dec 31st, 2019). Three types of data are used in this inversion, including GPS, SAR interferogram, and strainmeter time series. We use daily solutions of ground displacements recorded by 21 regional GPS stations, with a time window starting 50 days (May 17th, 2019) before the mainshock and ending 150 days (Dec 3rd 2019) after the mainshock. The daily GPS time series are recorded by the plate boundary observatory network (PBO) and accessed through UNAVCO. The original solutions are fitted by a combination of several synthetic functions, i.e. a linear trend, co-seismic steps of the foreshock and mainshock, and a post-seismic (logarithmic) trend. The linear trend and co-seismic steps are then removed from the original displacement time series. The GPS data for the days of the foreshock and mainshock are not used in the inversion, because it requires separate processing to estimate the displacements before and after the events.

The SAR images include 27 and 22 frames for ascending and descending orbits, respectively. The original SAR images are downsampled into 576 and 686 pixels for the ascending and descending orbits, respectively, using the identical sampling method as the co-seismic images. For each of the SAR images, we correct the linear trend referenced to GPS displacements. The vertical components of the GPS data are not used for the ramp estimation, because errors of the vertical components are often greater than the sig-

nal, and their inclusion may cause larger error (Fig. S22) in the ramp estimation (Shen and Liu, 2020). In addition to the afterslip, viscous relaxation also contributes to the post-seismic ground deformation, which needs to be accounted for before performing slip inversions. We use a regional visco-elastic model (Liu et al., 2020) to simulate the post-seismic relaxation caused by the mainshock. The relaxed displacement field is calculated by a 1D-layer simulation code (Wang et al., 2006) at the GPS/SAR data sampling locations, and then removed from the GPS/SAR time series. A comparison between the synthetic relaxed and corrected displacement fields is plotted in Figs. S21 and S23.

To resolve the deformation that occurred immediately after the mainshock, we adopt the three-component plane-strain time series of station B0921 in the afterslip inversion. The other two stations were either not functioning (B0916) or dominated by slip on the Garlock fault (B0917), thus they are not used in the inversion. Original strain time series of station B0921 are cut from 1 hour after the mainshock to 16 hours after the mainshock to enable monitoring of early afterslip. The strain data processing is identical to that used in the slow-slip inversion after the M_W 6.4 foreshock.

2.5. Full time series inversion for afterslip following the M_W 6.4 foreshock and afterslip following the mainshock

SAR time series provide the highest spatial resolution and lowest temporal resolution. GPS data are daily sampled at discrete locations. Strainmeter data provide immediate monitoring of afterslip at 1-minute level sampling, though its long-term recording may suffer from baseline shifts. Incorporating different types of ground deformation time series introduces a challenge to the task of afterslip inversion. Traditional inversion algorithms treat the time series as segmented data, which extract the differential displacements from displacement time series to invert for the associated slip pattern (e.g., Bedford et al., 2013; Moreno et al., 2010), or decompose the displacement time series as principal components, which separates signal and noise in different components (e.g., PCAIM, Kositsky and Avouac, 2010). For the afterslip inversion following the M_W 6.4 foreshock, we test the PCAIM algorithm in our initial attempt but find that the sparse spatial sampling of strainmeter stations does not allow a complete separation of deformation signal and noise in different principal components. For the post-seismic period, these data have different sampling times and temporal coverage, introducing challenges to incorporate principal component analysis. Thus we develop a full time series inversion (FTI) algorithm, which assumes a uniform slip evolution function for all patches and uses all sample points of the time series in the inversion. The evolution function is described by Equation (1):

$$\boldsymbol{S}(\boldsymbol{t}) = \boldsymbol{S}(\boldsymbol{t}, \boldsymbol{t_0}, \boldsymbol{\tau}) = \begin{cases} \mathbf{0}, & \textbf{for } \boldsymbol{t < t_0} \\ \log\left(\frac{\boldsymbol{t}-\boldsymbol{t_0}}{\boldsymbol{\tau}} + \mathbf{1}\right), & \textbf{for } \boldsymbol{t > t_0} \end{cases} \quad (1)$$

where $\boldsymbol{t_0}$ is the earthquake initiation time and $\boldsymbol{\tau}$ is the characteristic decay time. Since the source evolves slowly in the afterslip period, we adopt the quasi-static approximation and calculate the displacement/strain evolution function at the data sample time, for the purpose of combining different datasets in a linear inversion framework. "Full" in the acronym is reflected in two aspects: firstly, all sampling in a time series can be used instead of segmented time; secondly, data with different temporal samples or spans can be adopted in a joint inversion framework. The characteristic decay time $\boldsymbol{\tau}$ is the only hyper-parameter that needs to be assumed before performing an inversion. We can perform inversion under different decay times and obtain the optimized value from a trade-off curve of the smooth level versus residual RMS (Fig. S24-S25). This approach resembles that used to determine rupture velocity in the multi-time-window inversion. A similar strategy assuming logarithmic decay functions to realize the time series inversion was initially proposed by Liu and Xu (2019), which combined a Heaviside and logarithmic function to perform joint inversion of co-seismic and post-seismic slip using SAR time series. Our tests find that the advantages of the FTI inversion include:

1. Using full time series reduces the estimation errors. If the assumed source evolution function is a valid representation of afterslip processes, the adopted inversion technique essentially uses all sample points to estimate one parameter (total amplitude), which is more robust to the observational errors in comparison with segmented data inversion.
2. The FTI inversion is more flexible to incorporate different data in a joint inversion. Because the evolution function can be arbitrarily calculated at different sample times, it is straightforward to combine strainmeter, GPS, and SAR data in a joint inversion scheme. To determine early afterslip of the RC sequence requires combining the early afterslip sampling of strainmeter data, long base-line displacement recording of GPS data, and high spatial sampling of SAR data in a joint inversion scheme, which is the main motivation for developing this inversion technique.
3. The FTI inversion allows handling slow-slip processes with different initial times and decay time scales. Such inversion can be realized by parameterizing Green's functions with different source evolution functions and perform simultaneous linear inversion under the same framework. We also test two-process afterslip inversion for the RC sequence, which is discussed in the following sections.

Besides the common evolution function assumption, special treatments of SAR image correction and initial frame error correction are made in the inversion matrix reconstruction. We include more details of inversion matrix correction in the supplementary materials.

We adopt the FTI inversion algorithm and use the strainmeter time series of stations B0916, B0917, and B0921 to invert for the afterslip on the foreshock faults (F1 and F2) following the M_W 6.4 foreshock. The strain step-change associated with the M_W 5.4 event is removed from the original strain time series, and station B0921 presents a smooth evolution curve demonstrating that it is valid to use a presumed logarithmic decay function. Because the strainmeter data are limited, with only three stations and three components at each station being available, regularization is adopted in the inversion, including Laplacian smoothing of slip. We assume that slip on the sub-faults ruptured by the M_W 6.4 foreshock is limited to the period between the M_W 6.4 foreshock and the mainshock; thus we include slip damping for these sub-faults.

3. Results and discussion

3.1. Kinematic slip model of foreshock and mainshock

The kinematic slip models of the M_W 6.4 foreshock and the M_W 7.1 mainshock are visualized in Fig. 3. The kinematic slip models demonstrate that the M_W 6.4 foreshock initiated at the junction between F1 and F2, in the vicinity of a slip concentration on F1. The foreshock rupture expanded to the southwestern end of F2, with a heterogeneous slip distribution. The mainshock shows a downward and bilateral rupture propagation dominated by southeastward expansion. The peak slip is approximately 8.0 m at $\sim$ 7.0 km depth in the vicinity of the hypocenter. The total seismic moment of the mainshock is 5.4×10^{19} N·m, which gives $M_W = 7.09$, consistent with the long-period point-source magnitude. The rupture velocity of the mainshock is determined to be

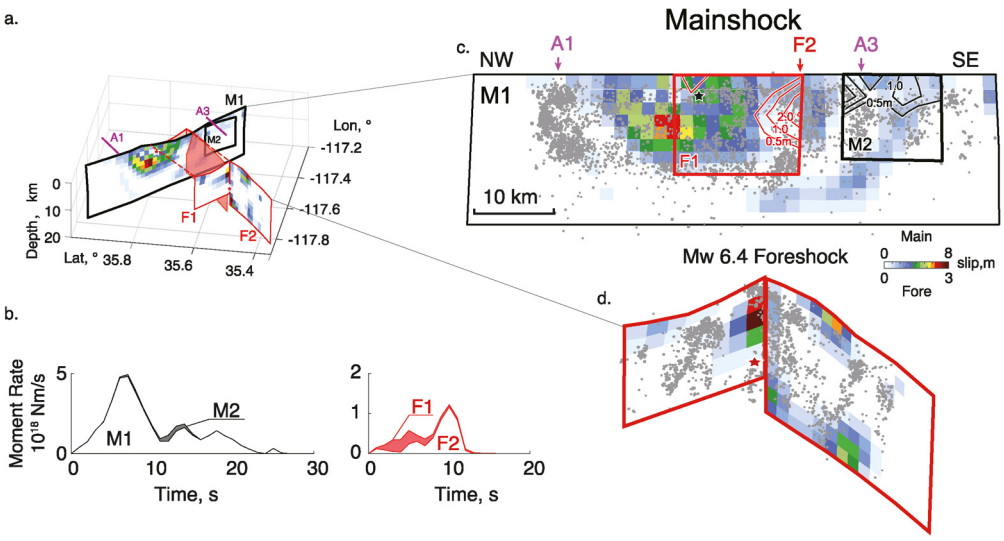

Fig. 3. Spatial and temporal slip evolution. **a.** Foreshock and mainshock slip distributions are plotted in color in a 3D view. The M_W 6.4 foreshock model is shifted for better visualization. **b.** Moment rate functions of the mainshock and M_W 6.4 foreshock are plotted with black and red polygons, with the contribution of each segment labeled. Contributions of slip-on M2 and F1 are plotted as gray and red filled polygons. **c.** Slip distribution for the M_W 7.1 mainshock on fault M1 is plotted as a base color map. The mainshock hypocenter is indicated by the black star. Aftershocks are projected onto the slip pattern. Slip on F1 and M2 are plotted as red and black contours projected onto M1. **d.** The M_W 6.4 foreshock slip distribution on F1 and F2 is plotted in a 3D view. The M_W 6.4 hypocenter is indicated by the red star. The hypocenters of the M_W 5.4 and mainshock are plotted as black stars. Small foreshocks are plotted as gray-filled circles projected on the slip pattern.

$\sim$ 1.8 km/s, which is relatively low for strike-slip events. Hypocentral locations of the smaller seismicity (including foreshocks and aftershocks) are largely complementary to the slip distributions of the foreshock and the mainshock (Fig. 3). The overall slip pattern is consistent with those reported by other groups (e.g., Chen et al., 2020; Goldberg et al., 2020; Liu et al., 2019; Magen et al., 2020; Ross et al., 2019; Wang et al., 2020), although subtle details differ, in part due to varying fault parameterizations and data selection. Although shallow slip deficits are significant above the concentrated slip area, e.g., near the hypocenters of the M_W 6.4 foreshock and mainshock; many segments have peak slip at shallow depths, e.g., at the northwest ends of the main and parallel faults (M1 and F1) and the central segment of the orthogonal fault (F2). Several slip voids are observed on the main fault, the loci of which are associated with cross faults. The mechanism causing such slip voids is discussed later. We also make a forward prediction for the lateral displacements observed by several near-field campaign GPS stations (Floyd et al., 2020) using our kinematic slip models (Fig. S17). The foreshock co-seismic displacements are generally well predicted by our foreshock slip model. There are minor discrepancies between the predictions and observations for the mainshock displacements. Detailed analysis is available in the supplementary materials.

3.2. Slip following the M_W 6.4 foreshock and cascade triggering of the mainshock

Inversion results for slow deformation following the M_W 6.4 foreshock are shown in Fig. 4, with most slip located on the SW-trending fault (F2) near its junction with the NW-trending fault (F1). Moderate slip is obtained on F1 and near the southwest end of F2, yielding a total moment magnitude of $M_W = 5.64$. In order to test the data sensitivity, we divide the foreshock faults into three segments (Fig. 4): Seg1 (whole F1), Seg2 (NE half of F2), and Seg3 (SW half of F2), and perturb the total moment on each segment to test for the impact on data fits. When perturbing slip of each segment, we keep the slip pattern of each segment unchanged and multiply a scaling factor to all sub-fault slip values to generate slip models with different moments. The associated synthetics are then compared with the observations. The residual

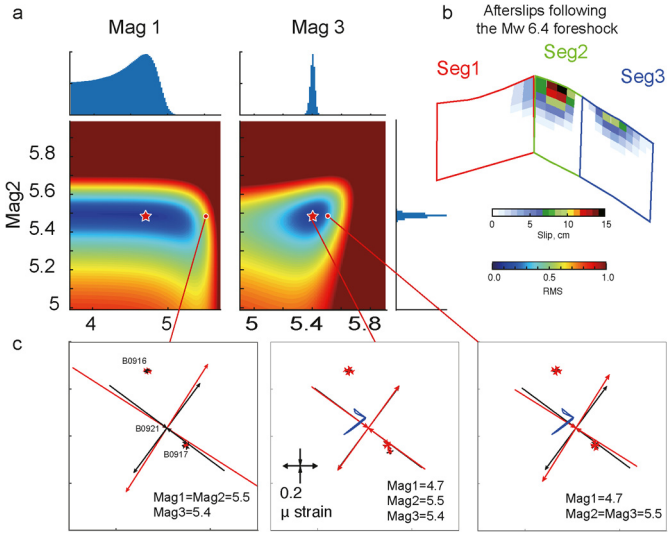

Fig. 4. Inversion results for afterslip following the M_W 6.4 foreshock. **a.** Residual distributions are plotted in a blue-red color scale in the segment distribution domain for Mag1 versus Mag2 and Mag3 versus Mag2 in the left and right panels, respectively. Scales of each segment are denoted in Fig. 4b. The marginal distributions of the magnitude of each segment are plotted as histograms in the top and right panels, respectively. **b.** Afterslip distribution (M_W 5.5 event removed) is plotted as a white-black color scale. **c.** Synthetic plane strain tensors computed by different combinations of segment magnitudes are plotted as red arrows in each panel. Observed plane strain tensors are plotted as black arrows. The equivalent magnitudes of each segment are labels and connect to the location in Fig. 4a.

distribution and synthetic comparisons are plotted in Figs. 4a and 4c. The preferred moment magnitudes on the three segments are 4.7, 5.5, and 5.4, respectively. Setting the moment magnitude of segments 1 and 3 (Mag1 and Mag3) to 5.5 (matching the magnitude of segment 2, Mag2) produces significant amplitude change and rotation of the B0921 strain tensor; thus the slip resolution on each segment mainly originates from the direction and amplitude at station B0921. We assume the observational error is about 10% of the maximum strain amplitude and calculate the probability density function of each magnitude and the residual distribution (Fig. 4a). The marginal distributions of magnitudes show

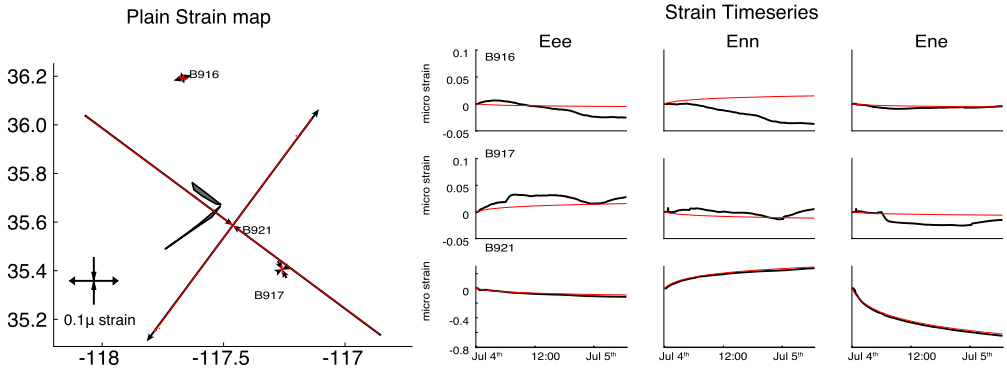

Fig. 5. Strainmeter data and model fitting. **a**. Observed and synthetic plane strain tensors plotted as black and red arrows, respectively. The foreshock fault planes (F1 and F2) are plotted as black polygons. **b**. Observed and synthetic strain time series are plotted as black and red curves, respectively. Row panels plot the strain time series of each station, and column panels plot the strain time series of each component, respectively.

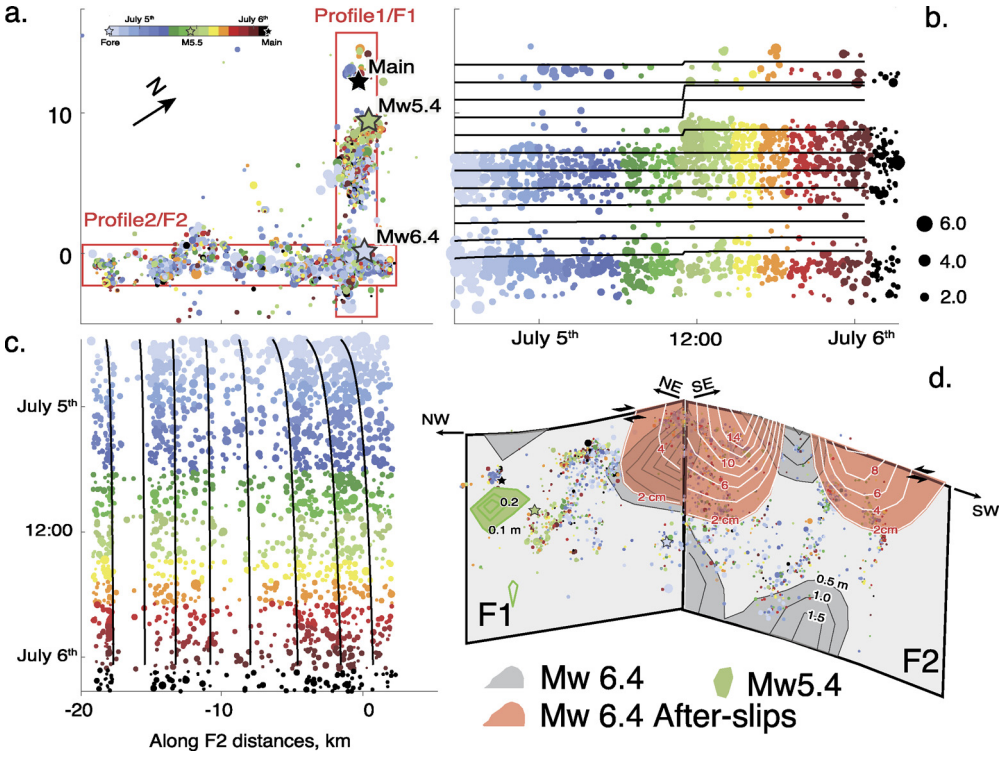

Fig. 6. Spatio-temporal evolution of seismicity and slip on faults during the foreshock period. **a.** Foreshocks are plotted as dots, color-coded by their occurrence time. Map orientation is rotated to the strike direction of F1. Two profiles are drawn along F1 and F2 to visualize their respective seismicity evolution. **b**. Foreshock distribution along the F1 strike direction is plotted as dots with occurrence time marked by color. Accumulated moment of the fault slip inverted by strainmeter time series is integrated along depth and plotted along the strike direction as black curves. **c.** Similar to **b** for the foreshock distribution along F2. **d.** M_W 6.4 foreshock slip and the post-M_W 6.4 slip are plotted as gray and red slip areas, respectively. The slip pattern of the M_W 5.5 foreshock is plotted as green contours. The foreshocks are plotted as dots, color-coded by their occurrence time with the same color scale as in **a**.

that Mag2 is well constrained between 5.45 and 5.55. Mag1 shows larger uncertainty, while the upper limit of Mag1 is constrained to be < 5.1. Thus slip on F1 (Mag1) is significantly smaller than that on F2 (Mag2+Mag3). Data fitting of the strainmeter observations is plotted in Fig. 5 in both map view and with temporal evolution function. It is noted that the strain amplitude of B0921 is one order of magnitude larger than that of the other two stations, which provides most constraints on the afterslip following the M_W 6.4 foreshock. The strain time series of B0916 and B0917 suffer from local noise, and the model only fits the general shape and amplitude.

Recalling that the M_W 5.4 event is removed from the strain time series and the remnant slip on F1 is less than M_W 5.1, we find that the M_W 5.4 event dominates the total moment release on F1 in the period between the M_W 6.4 event and the mainshock. To compare the seismic and aseismic slip in the period between the M_W 6.4 event and the mainshock, we plot the foreshock distribution and migration on F1 and F2 in Fig. 6, which shows different foreshock migration patterns along the strikes of the two faults. The foreshocks on F2 initiated immediately after the M_W 6.4 foreshock along its full length (Fig. 6c). No significant jumps are found in the lateral aftershock migration pattern on F2. The foreshock activity on F2 decayed with time following a typical power-law decaying pattern (Omori law) up to the time of the mainshock when activity on F2 abruptly reduced. The stress control on F2 seismic activity is discussed in a later section. The foreshock activity on F1 was concentrated at its southeast half in the first 19 hours after the M_W 6.4 foreshock. The M_W 5.4 event ruptured a previously quiescent segment on the northwest edge of F1 and increased the surrounding seismic activity (Fig. 6). The

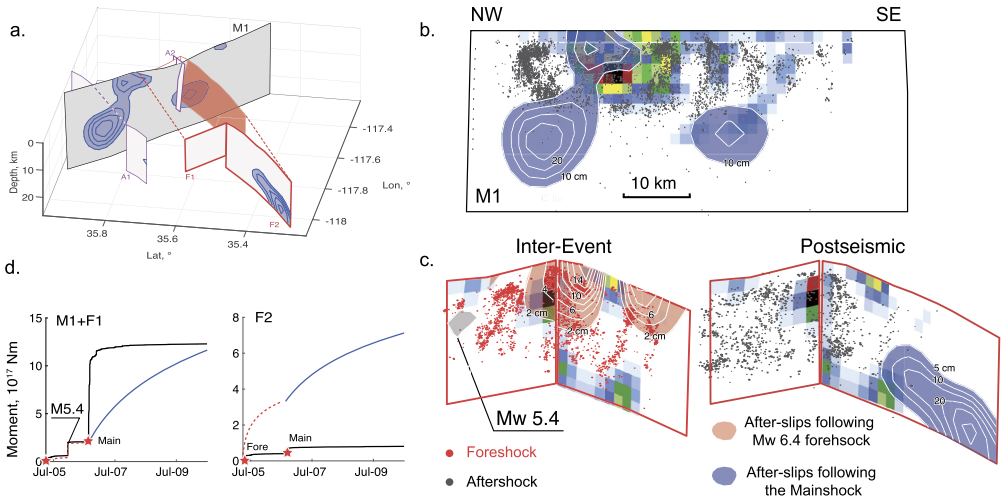

Fig. 7. Spatio-temporal evolution of seismicity and slip on faults from foreshock to post-seismic period. **a.** Spatial geometry of faults used in the post-seismic slip model is plotted as black (M1 and M2), red (F1 and F2) and magenta (A1, A3) polygons. The main afterslip areas are illustrated by blue contours. **b** and **c.** Similar to Fig. 3b and 3c. Afterslip areas are marked as blue contours. Afterslip areas following the M_W 6.4 foreshock are plotted as red contours. Foreshocks and aftershocks are plotted as red and black dots, respectively. **d.** Evolution functions of moment release on NW trending faults (M1 and F1) and SW trending faults (F2) are plotted in each panel, respectively. Catalog moment release is plotted as black curves. Moment release of afterslip models following the M_W 6.4 foreshock and the mainshock are plotted as red dashed and solid blue curves, respectively.

mainshock occurred about 16 hours after the M_W 5.4 foreshock near its hypocenter (Fig. 6). It thus appears likely that the M_W 5.4 foreshock played a key role in triggering the mainshock. In this study, we assume that the M_W 5.4 event occurred on F1, though Shelly (2020) reported a northeastward lineation of aftershocks of the M_W 5.4 event and inferred the ruptured fault plane is the NE striking nodal plane orthogonal to F1. Dislocations on either nodal plane produce identical strain patterns, thus we cannot discriminate between these two possibilities from the strain observations. An alternative to the interpretation of Shelly (2020) is that the M_W 5.4 event ruptured on F1, yet triggered aftershocks on an orthogonal fault. Analysis related to the dynamic rupture directivity of the M_W 5.4 event may be important to determine its orientation. Jin and Fialko (2020) conducted a Coulomb stress calculation at 7 km depth and reported that the nucleation of the mainshock hypocenter may be discouraged by the M_W 5.4 event. Because the Coulomb stress varies significantly near the ruptured fault plane and the M_W 5.4 event is close to the mainshock hypocenter, the uncertainty related to its location, orientation, and dimension, as well as the uncertainty of mainshock hypocentral location need to be considered when evaluating the stress interactions between the M_W 5.4 event and the mainshock. Our analysis assumes that the M_W 5.4 event occurred on F1, but there is uncertainty in the mechanism and location of this event, which affects quantification of the triggering mechanism between the M_W 5.4 event and mainshock. Rupture during the M_W 6.4 event did not reach the northwest end of F1 and the seismic activity closest to the mainshock hypocenter was promoted by the M_W 5.4 event. The total moment release on F1 after the M_W 6.4 foreshock is dominated by the M_W 5.4 event, thus our interpretation is that it is likely that the M_W 5.4 event promoted the nucleation process of the mainshock due to its proximity and relative moment release.

The distinct slip behavior on F1 and F2 can be interpreted in the context of an "asperity model". Asperities are portions of fault surfaces that are strongly locked during stress loading and rupture with large slip during earthquakes (e.g. Lay et al., 1982). Cascaded triggering can be produced by sequential rupturing of large asperities (Lay et al., 2012). The M_W 6.4 and 5.4 foreshocks ruptured different asperities on F1 (Fig. 6). Since the mainshock hypocenter is located close to the M_W 5.4 event and the slip on F1 is dominated by the seismic slip of the M_W 5.4 event, the sequential rupturing of asperities during the foreshocks appears to be the controlling mechanism of the foreshock to mainshock triggering on F1. The co-seismic slip distribution on F2 indicates that most asperities ruptured co-seismically, leaving the rest of the fault to displace in afterslip with a dominant component of aseismic slip. This phenomenon is further evident in the comparison of afterslip models following the M_W 6.4 foreshock and the mainshock.

3.3. Seismic vs. aseismic moment release of the orthogonal fault system

The FTI inversion results of the afterslip evolution are plotted in Fig. 7 in comparison with the co-seismic models. During the investigated period (July 5-Dec 31, 2019), considerable afterslip occurred with an equivalent slip moment of $M_W = 6.4$. On the main fault plane (M1), the afterslip forms a significant complementary pattern with the co-seismic slip. Most afterslip occurred near the two ends of M1 and is partially overlapped with aftershocks. The most significant afterslip occurred to the northwest of the co-seismic slip at ~ 20 km depth with a maximum slip of ~ 0.3 m. Shallow afterslip occurred above the major slip area of the mainshock, which is consistent with the shallow-slip deficit in the co-seismic model. Limited afterslip occurred beneath the co-seismic slip area. This pattern is validated with single fault plane inversion (only M1), single data type inversion, step displacement inversion, and inversions without viscous relaxation corrections, with the pattern holding up in all tests. Although stress changes are concentrated at the lateral ends and bottom edge of the co-seismic slip, lateral variation of rate-and-state dependent frictional properties may drive afterslip to be released faster on velocity strengthening patches. These patches commonly present "weak" frictional property and behave as barriers for dynamic ruptures. For example, the 2016 Kumamoto earthquake was stopped by the Aso volcano (Yue et al., 2017); meanwhile the volcano area presented significant afterslip and viscoelastic deformation (Moore et al., 2017). The 2019 Ridgecrest earthquake also stopped at the Coso geothermal area (Ross et al., 2019), where the most significant afterslip occurred. This observation resembles that of the 2016 Kumamoto earthquake and reflects the influence of a "barrier" introduced by velocity strengthening frictional properties.

The relative ratio of seismic versus aseismic slip is important for analyzing slip budget and future seismic hazard. We use the

earthquake catalog and slip models to represent the seismic versus total moment release on each fault plane. We assume events within 2 km from the fault plane occurred on the fault plane and share an identical focal mechanism, and the moment evolution is plotted in Fig. 7d. The afterslip models include all types of moment release on the fault plane, and we sum moments of all patches to calculate the total moment on each fault plane and scale the total moment by the source evolution function $S_0(t)$ to represent "total" release functions. Because the M_W 5.4 event was excluded from the strain time series when performing slip inversion for the period between the M_W 6.4 event and the mainshock, we assign the M_W 5.4 event slip model (Fig. S20) using a Heaviside (step) function and add that to the moment release function for F1. In Fig. 7d, the moment evolution in the first three days after the mainshock is plotted. The comparison of two moment evolution functions (from catalog and slip model) reveals distinct releasing patterns on parallel and orthogonal faults in both afterslip periods. For all the NW-trending faults (parallel faults including F1, M1, and M2), the seismic moment is comparable to the total moment in periods after the M_W 6.4 foreshock and the mainshock. Moments recovered by slip-models include both seismic and aseismic release, which is expected to be higher than pure seismic release. However, in the beginning epoch of the post-seismic period, the seismic moment increased faster than that of the slip model. This may be attributed to either off-fault aftershocks in the catalog being summed or the mechanism varies significantly in the catalog events, thus producing artificially high seismic moment summation. Although similar bias may hold for other fault planes, the seismic versus total moment history we observe on fault F2 (orthogonal faults) is distinct from that observed on NW-trending faults. The seismic moment accounted for is about 11% of the total moment from the slip models in afterslip following both the M_W 6.4 foreshock and the mainshock. This analysis clearly shows that dual slip modes are distinct on NW trending and SW trending faults. This phenomenon is also consistent with the cascade triggering mechanism of the fore-to-main-shock relationship. We also invert for the afterslip evolution using two processes. Though the "fast" and "slow" processes show clear spatial separation, it is not clear whether this effect is caused by uneven data coverage or by distinct physical processes. We include related discussion in the supplementary materials, yet cannot draw a definitive conclusion based on these analyses.

The seismic moment release didn't increase significantly after July 7th. Thus, it is anticipated that over a long-term (longer than about a week), the aseismic moment release would dominate on both fault systems. This phenomenon is consistent with the aseismic slip dominated post-seismic moment releases observed in many subduction zone earthquakes, e.g., the Maule earthquake (Lin et al., 2013), the Nias earthquake (Hsu et al., 2006), and the Tohoku earthquake (Diao et al., 2014). The exceptional observations of the Ridgecrest earthquake provide an opportunity to look into the very early post-seismic period, and we observe aseismic slip overtaking the seismic release several days after the mainshock. This indicates that the seismic response to the co-seismic shaking or stress changes associated with the cascade model may be a dominant factor in the early stage of post-seismic responses, while aseismic release account for a more important part over a longer time. The slow-slip driving model (Hsu et al., 2006; Perfettini et al., 2018) assumes afterslip drives aftershocks, which predicts that the cumulated number of aftershocks exhibit a similar evolution pattern as that of afterslip. In this study, we quantitatively compare the seismic versus total moment release in the post-seismic period, and the observed overtake pattern suggests that two competing mechanisms influence the aftershock sequence of the Ridgecrest earthquake; but in the early stage it is the earthquake rupture, not the slow-slip, that was the dominant driving mechanism.

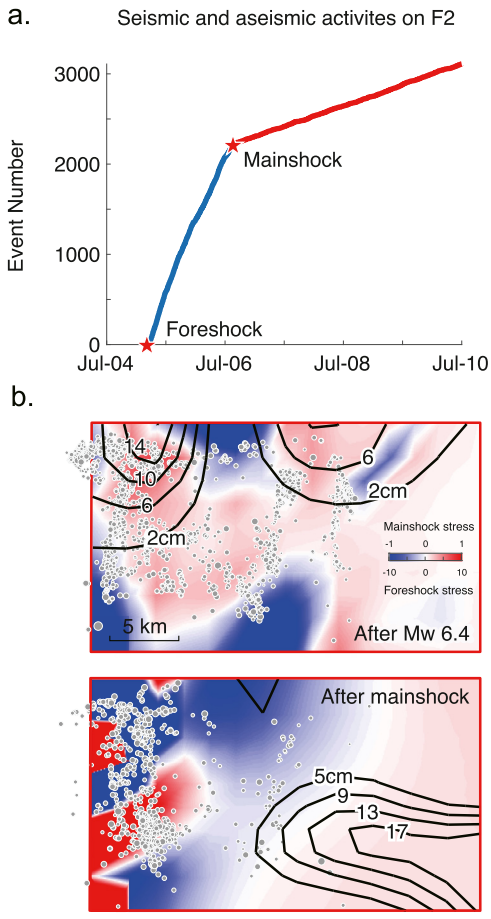

Fig. 8. Seismic and aseismic activities on F2 from the afterslip period following the M_W 6.4 foreshock and mainshock. **a.** The Cumulative number of foreshocks and aftershocks near fault F2 plotted as blue and red curves, respectively. **b.** Co-seismic Coulomb stress changes produced by the M_W 6.4 and mainshock are plotted in the top and bottom panels, respectively, using different color scales. Foreshocks and aftershocks on F2 are plotted as gray filled dots. Afterslip on F2 following the M_W 6.4 foreshock and the mainshock are plotted in the top and bottom panels, respectively.

3.4. Driving mechanism of afterslip following the M_W 6.4 foreshock and the mainshock

It has been noted that seismicity on F2 shows a significant decrease after the mainshock (https://temblor.net/earthquake-insights/ridgecrest-earthquake-shut-down-cross-fault-aftershocks-9249/), which drops from 1499 events per day during the period between the M_W 6.4 foreshock and the mainshock to 228 events per day within three days after the mainshock (Fig. 8). This sharp drop of seismicity appears to be counter-intuitive, because the mainshock is expected to cause a large stress change on F2. We calculated the Coulomb stress change produced by the M_W 6.4 foreshock and mainshock on F2, in which a frictional parameter of 0.4 was used to relate normal and shear stress changes. The Coulomb stress changes on F2 are calculated in reference to the M_W 6.4 foreshock slip direction, which is then compared with foreshock/aftershock activity and afterslip following the major events (Fig. 8). Foreshocks and aftershocks locate within the Coulomb stress increase areas produced by the M_W 6.4 foreshock and mainshock, respectively. These stress increase areas are also correlated with afterslip areas. The area at the center of F2 shows intensive foreshock activities, with both seismic and aseismic slip. This area is covered by a shadow of Coulomb stress decrease produced by the mainshock; thus, it seems the afterslip/aftershock activities are damped by mainshock stress changes. On the con-

trary, the Coulomb stress on the southwest end of F2 is elevated by both major events, thus is likely to increase afterslip. These comparisons indicate that co-seismic stress change may be an important factor controlling the slow-slip behaviors on F2. Thus the afterslip models can be used to investigate the frictional property of regional faults under some constitutive relationships relating to slow-slip velocity and stress changes. The rate-state friction laws may be a promising candidate to perform such an analysis.

Abundant aftershocks on orthogonal structures are reported for the Ridgecrest earthquake sequence, which draws attention to the aftershock hazard on such structures (e.g. Ross et al., 2019). In this study, we investigate moment release on these orthogonal structures and find that for the most significant SW-trending fault (F2), aseismic slip dominates the moment release in the period following the M_W 6.4 foreshock and the mainshock. Other SW-trending faults (A1 and A2) also present similar phenomena with significant afterslip ($M_W = 5.6$ for A1 and $M_W = 5.1$ for A2), although the seismic moments on these structures are difficult to quantify. Aseismic slip behavior may be a common feature for the SW-trending faults near the Ridgecrest earthquake.

The main fault (M1) shows limited co-seismic slip near the crossing point of these SW-trending faults. For example, the mainshock slip terminates at the junction between M1 and A1. Two voids of the mainshock slip are spatially correlated with cuts of off-fault structures (F2 and A3). For other strike-slip fault systems, the background seismicity on orthogonal or conjugate structures is also pervasive during the inter-seismic loading, such as the orthogonal faults near the San Jacinto fault, and the Xiaojiang Fault (Zhou et al., 2020). These observations indicate that stress is partially released on these perpendicular faults when the whole area is subject to shear loading in the inter-seismic period. The spatial and temporal clustering of these off-fault events indicates that they are likely to be driven by aseismic slip (Zhou et al., 2020). Thus these orthogonal structures regularly release stress loading and produce stress shadows on the main fault resulting in stress barriers (e.g., Yue et al., 2017). The relatively low rupture velocity of the Ridgecrest earthquake also indicates that the rupture encountered several barriers inhibiting continuous rupture. The feasibility of such fault interactive mechanisms requires validation by dynamic rupture modeling. The stress release behavior of these off-fault structures also requires creep-related dynamic fault modeling algorithms to validate.

The orthogonal fault system is the result of a unique tectonic environment in eastern California. The major slip on the NW trending fault produces plentiful small orthogonal faults in this broadened deformation zone, illuminated by the Ridgecrest earthquake sequence. Detailed afterslip data show quasi-regular spaced perpendicular strips along the M1 fault, implying the fault intercepting with multiple orthogonal weak fault segments. Wrench-style shear motions of the fault systems over geological time weakened the off-fault region and promoted secondary sub-parallel faults, producing a grid of faults/sub-faults as illuminated by the Ridgecrest earthquake sequence. This interpretation may also help our understanding of tectonic deformation in other parts of the world with orthogonal fault systems such as in SW China, where the Xiaojiang fault intercepts with the Red River fault, and produced the 1970 M_W 7.1 Tonghai earthquake.

4. Conclusions

We utilize the abundant seismic, geodetic, and strainmeter observations to construct a 3D fault model and co-seismic slip models and afterslip models following the M_W 6.4 foreshock and the mainshock to analyze the slip behavior and stress interactions of the Ridgecrest earthquake sequence. Our key findings include:

1. The M_W 6.4 foreshock ruptured an orthogonal fault system while the mainshock mainly ruptured a NW-trending fault. The foreshock, mainshock, and afterslip distributions have complementary slip distribution patterns on the fault planes.
2. The mainshock was likely triggered by the foreshock through a cascade of events on a short fault branch parallel to the main fault plane. The moment release on this fault is dominated by seismic slip. An M_W 5.4 event appears to be the key foreshock triggering the mainshock.
3. Overall slip on parallel and orthogonal faults involves different balances of seismic and aseismic slip. Seismic slip dominates the post-mainshock slip of the NW-trending faults, while aseismic slip dominates the post-foreshock slip on the SW-trending orthogonal fault. This is indicated by afterslip models following both the M_W 6.4 foreshock and the mainshock.
4. Abundant secondary orthogonal faults were activated during the Ridgecrest earthquake sequence. Their locations are correlated with gaps in the mainshock slip model. Seismic activities on the major north-east trending fault (F2) show significant change after two major events, which appear to be controlled by the stress change of two major events.

CRediT authorship contribution statement

The credit of authors is stated as follows:

Han Yue is in charge of Seismic data preparation, inversion, algorithm design and development, manuscript writing.
Jianbao Sun is in charge of SAR data processing, inversion theory and scientific problem discussion.
Min Wang is in charge of GPS data processing, inversion theory and scientific problem discussion.
Zhengkang Shen is in charge of GPS data processing, inversion theory, tectonic and scientific problem discussion.
Lian Xue is in charge of Strain data processing, inversion theory and scientific problem discussion.
Weifan Lu and Yijian Zhou are in charge of seismicity detection.
Chunmei Ren is in charge of regional velocity model extraction.
Mingjia Li is in charge of post-seismic SAR time series processing.

Declaration of competing interest

The authors declare that they have no known competing financial interests or personal relationships that could have appeared to influence the work reported in this paper.

Data and materials availability

GPS data are recorded by plate boundary observatories (PBO) and made available by UNAVCO. The strong motion network is operated by Southern California Seismic Network (SCSN) (https://authors.library.caltech.edu/34628/) and made available by Southern California Earthquake Data Center at Caltech (SCEDC Caltech Dataset, https://doi.org/10.7909/C3WD3xH1). Strainmeters stations are operated by the GAGE facility and made available by UNAVCO. This work contains Copernicus data from the Sentinel-1 satellites provided by ESA, and ALOS-2 data from JAXA through ALOS-2 RA 6 project (PI No. 3381002).

Acknowledgements

We thank Prof. Shengji Wei for helping with the strong motion data processing, Lei Zhang from Hong Kong Polytechnic University and Jinghui Fan from China Geological Survey for helping on ALOS-2 data analysis. This work is supported by the National Key Research and Development Program of China (2018YFC1504203 H.Y.),

the National Natural Science Foundation of China (42021003 H.Y. & L.X., 41774043 J. S.), and the Dragon Project (32341 J.S.). Southern California Earthquake Center publication #XXXX. (Z.S.) and US National Science Foundation (EAR1802364 T. L.).

Appendix A. Supplementary material

Supplementary material related to this article can be found online at https://doi.org/10.1016/j.epsl.2021.117066.

References

Bedford, J., Moreno, M., Baez, J.C., Lange, D., Tilmann, F., Rosenau, M., Heidbach, O., Oncken, O., Bartsch, M., Rietbrock, A., 2013. A high-resolution, time-variable afterslip model for the 2010 Maule $M_W = 8.8$, Chile megathrust earthquake. Earth Planet. Sci. Lett. 383, 26–36.

Chen, K., Avouac, J.-P., Aati, S., Milliner, C., Zheng, F., Shi, C., 2020. Cascading and pulse-like ruptures during the 2019 Ridgecrest earthquakes in the Eastern California Shear Zone. Nat. Commun. 11, 1–8.

Diao, F., Xiong, X., Wang, R., Zheng, Y., Walter, T.R., Weng, H., Li, J., 2014. Overlapping post-seismic deformation processes: afterslip and viscoelastic relaxation following the 2011 M_W 9.0 Tohoku (Japan) earthquake. Geophys. J. Int. 196, 218–229.

Dieterich, J.H., 1979. Modeling of rock friction: 1. Experimental results and constitutive equations. J. Geophys. Res., Solid Earth 84 (B5), 2161–2168.

Dokka, R.K., Travis, C.J., 1990. Role of the eastern California shear zone in accommodating Pacific-North American plate motion. Geophys. Res. Lett. 17, 1323–1326.

DuRoss, C.B., Gold, R.D., Dawson, T.E., Scharer, K.M., Kendrick, K.J., Akciz, S.O., 2020et al.. Surface displacement distributions for the July 2019 Ridgecrest, California, earthquake ruptures. Bull. Seismol. Soc. Am. 110 (4), 1400–1418.

Ellsworth, W.L., Bulut, F., 2018. Nucleation of the 1999 Izmit earthquake by a triggered cascade of foreshocks. Nat. Geosci. 11 (7), 531–535.

Ende, M.P.A., Ampuero, J.-P., 2020. On the statistical significance of foreshock sequences in Southern California. Geophys. Res. Lett. 47, 3.

Floyd, M., et al., 2020. Survey and Continuous GNSS in the vicinity of the July 2019 Ridgecrest earthquakes. Seismol. Res. Lett. 91, 2047–2054.

Gan, W., Svarc, J.L., Savage, J., Prescott, W., 2000. Strain accumulation across the Eastern California Shear Zone at latitude 36 30′ N. J. Geophys. Res., Solid Earth 105, 16229–16236.

Goldberg, D.E., Melgar, D., Sahakian, V.J., Thomas, A.M., Xu, X., Crowell, B.W., Geng, J., 2020. Complex rupture of an immature Fault zone: a simultaneous kinematic model of the 2019 Ridgecrest, CA earthquakes. Geophys. Res. Lett. 47, e2019GL086382.

Hartzell, S.H., Heaton, T.H., 1983. Inversion of strong ground motion and teleseismic waveform data for the fault rupture history of the 1979 Imperial Valley, California, earthquake. Bull. Seismol. Soc. Am. 73, 1553–1583.

Hsu, Y.-J., Simons, M., Avouac, J.-P., Galetzka, J., Sieh, K., Chlieh, M., Natawidjaja, D., Prawirodirdjo, L., Bock, Y., 2006. Frictional afterslip Following the 2005 Nias-Simeulue earthquake, Sumatra. Science 312, 1921–1926.

Hough, S.E., Thompson, E., Parker, G.A., et al., 2020. Near-field ground motions from the July 2019 Ridgecrest, California, earthquake sequence. Seismol. Res. Lett. 91 (3), 1542–1555.

Jin, Z., Fialko, Y., 2020. Finite slip models of the 2019 Ridgecrest earthquake sequence constrained by space geodetic data and aftershock locations. Bull. Seismol. Soc. Am. 110 (4), 1660–1679.

Jones, L.M., Molnar, P., 1979. Some characteristics of foreshocks and their possible relationship to earthquake prediction and premonitory slip on faults. J. Geophys. Res., Solid Earth 84, 3596–3608.

Kato, A., Obara, K., Igarashi, T., Tsuruoka, H., Nakagawa, S., Hirata, N., 2012. Propagation of slow slip leading up to the 2011 M_W 9.0 Tohoku-Oki earthquake. Science 335 (6069), 705–708.

Kositsky, A., Avouac, J.P., 2010. Inverting geodetic time series with a principal component analysis-based inversion method. J. Geophys. Res., Solid Earth 115.

Lay, T., Kanamori, H., Ammon, C.J., Koper, K.D., Hutko, A.R., Ye, L., Yue, H., Rushing, T.M., 2012. Depth-varying rupture properties of subduction zone megathrust faults. J. Geophys. Res., Solid Earth 117.

Lay, T., Kanamori, H., Ruff, L., 1982. The asperity model and the nature of large subduction zone earthquakes. EPR, Earthqu. Predict. Res. 1, 3–71.

Leprince, S., Barbot, S., Ayoub, F., Avouac, J.-P., 2007. Automatic and precise orthorectification, coregistration, and subpixel correlation of satellite images, application to ground deformation measurements. IEEE Trans. Geosci. Remote Sens. 45, 1529–1558.

Lin, Y.-n.N., Sladen, A., Ortega-Culaciati, F., Simons, M., Avouac, J.-P., Fielding, E.J., Brooks, B.A., Bevis, M., Genrich, J., Rietbrock, A., Vigny, C., Smalley, R., Socquet, A., 2013. Co-seismic and post-seismic slip associated with the 2010 Maule Earthquake, Chile: characterizing the Arauco Peninsula barrier effect. J. Geophys. Res., Solid Earth 118, 3142–3159.

Liu, X., Xu, W., 2019. Logarithmic model joint inversion method for co-seismic and post-seismic slip: application to the 2017 M_W 7.3 Sarpol Zahāb earthquake, Iran. J. Geophys. Res., Solid Earth 124 (11), 12034–12052.

Liu, C., Lay, T., Brodsky, E.E., et al., 2019. Coseismic rupture process of the large 2019 Ridgecrest earthquakes from joint inversion of geodetic and seismological observations. Geophys. Res. Lett. 46 (21), 11820–11829. https://doi.org/10.1029/2019GL084949.

Liu, S., Shen, Z., Bürgmann, R., Jónsson, S., 2020. A thin crème brûlée model for the Eastern California Shear Zone. Geology, in press.

Magen, Y., Ziv, A., Inbal, A., Baer, G., Hollingsworth, J., 2020. Fault rerupture during the July 2019 Ridgecrest earthquake pair from joint slip inversion of InSAR, optical imagery, and GPS. Bull. Seismol. Soc. Am. 110, 1627–1643.

McClusky, S.C., Bjornstad, S., Hager, B.H., King, R., Meade, B.J., Miller, M., Monastero, F., Souter, B., 2001. Present day kinematics of the eastern California shear zone from a geodetically constrained block model. Geophys. Res. Lett. 28, 3369–3372.

McLaskey, Gregory C., 2019. Earthquake initiation from laboratory observations and implications for foreshocks. J. Geophys. Res., Solid Earth 124 (12), 12882–12904.

Miller, M.M., Johnson, D.J., Dixon, T.H., Dokka, R.K., 2001. Refined kinematics of the Eastern California shear zone from GPS observations, 1993–1998. J. Geophys. Res., Solid Earth 106, 2245–2263.

Moreno, M., Rosenau, M., Oncken, O., 2010. 2010 Maule earthquake slip correlates with pre-seismic locking of Andean subduction zone. Nature 467, 198–202.

Moore, J.D., Yu, H., Tang, C.-H., Wang, T., Barbot, S., Peng, D., Masuti, S., Dauwels, J., Hsu, Y.-J., Lambert, V., 2017. Imaging the distribution of transient viscosity after the 2016 Mw 7.1 Kumamoto earthquake. Science 356, 163–167.

Perfettini, H., Frank, W.B., Marsan, D., Bouchon, M., 2018. A model of aftershock migration driven by afterslip. Geophys. Res. Lett. 45 (5), 2283–2293.

Ross, Z.E., Idini, B., Jia, Z., Stephenson, O.L., Zhong, M., Wang, X., Zhan, Z., Simons, M., Fielding, E.J., Yun, S.-H., 2019. Hierarchical interlocked orthogonal faulting in the 2019 Ridgecrest earthquake sequence. Science 366, 346–351.

Ruiz, S., Metois, M., Fuenzalida, A., Ruiz, J., Leyton, F., Grandin, R., Vigny, C., Madariaga, R., Campos, J., 2014. Intense foreshocks and a slow slip event preceded the 2014 Iquique M_W 8.1 earthquake. Science 345, 1165–1169.

Savage, J., Lisowski, M., Prescott, W., 1990. An apparent shear zone trending north-northwest across the Mojave Desert into Owens Valley, eastern California. Geophys. Res. Lett. 17, 2113–2116.

Schurr, B., Asch, G., Hainzl, S., Bedford, J., Hoechner, A., Palo, M., Wang, R., Moreno, M., Bartsch, M., Zhang, Y., 2014. Gradual unlocking of plate boundary controlled initiation of the 2014 Iquique earthquake. Nature 512, 299.

Shelly, D., 2020. A high-resolution seismic catalog for the initial 2019 Ridgecrest earthquake sequence: foreshocks, aftershocks, and faulting complexity. Seismol. Res. Lett. 91 (4), 1971–1978.

Shen, Z.K., Liu, Z., 2020. Integration of GPS and InSAR Data for Resolving 3-Dimensional Crustal Deformation. Earth Space Sci. 7, e2019EA001036.

Shi, Q., Wei, S., Zeng, H., 2019. The 2019 Ridgecrest M_W 6.5 and M_W 7.0 double-let: shallow and slow rupture on non-planar strike-slip faults revealed by Multiple Point Source inversions using 3D Green's functions. In: AGU Fall Meeting.

Strozzi, T., Kouraev, A., Wiesmann, A., Wegmüller, U., Sharov, A., Werner, C., 2008. Estimation of Arctic glacier motion with satellite L-band SAR data. Remote Sens. Environ. 112, 636–645.

Trugman, D., Ross, Z.E., 2019. Pervasive foreshock activity across southern California. EarthArXiv. Jun 22.

Unruh, J., Humphrey, J., Barron, A., 2003. Transtensional model for the Sierra Nevada frontal fault system, eastern California. Geology 31, 327–330.

Wang, K., Dreger, D.S., Tinti, E., Bürgmann, R., Taira, T.a., 2020. Rupture process of the 2019 Ridgecrest, California M_W 6.4 foreshock and M_W 7.1 earthquake constrained by seismic and geodetic data. Bull. Seismol. Soc. Am. 110, 1603–1626.

Wang, R., Lorenzo-Martín, F., Roth, F., 2006. PSGRN/PSCMP—a new code for calculating co- and post-seismic deformation, geoid and gravity changes based on the viscoelastic-gravitational dislocation theory. Comput. Geosci. 32, 527–541.

Yoon, C.E., Yoshimitsu, N., Ellsworth, W.L., Beroza, G.C., 2019. Foreshocks and mainshock nucleation of the 1999 M_W 7.1 Hector Mine, California Earthquake. J. Geophys. Res., Solid Earth 124 (2), 1569–1582.

Yue, H., Ross, Z.E., Liang, C., Michel, S., Fattahi, H., Fielding, E., Moore, A., Liu, Z., Jia, B., 2017. The 2016 Kumamoto $M_W = 7.0$ earthquake: a significant event in a fault–volcano system. J. Geophys. Res., Solid Earth 122, 9166–9183.

Yue, H., Zhang, Y., Ge, Z., Wang, T., Zhao, L., 2020. Resolving rupture processes of great earthquakes: reviews and perspective from fast response to joint inversion. Sci. China Earth Sci. 63, 492–511.

Zhou, Y., Yue, H., Zhou, S., Zhao, L., Yang, Z., Yao, Y., 2020. Weak off-fault structures revealed by micro-seismicity along Xiaojiang Fault Zone (China) and their implications for seismic hazard assessment. J. Geophys. Res., Solid Earth, submitted for publication.

Supplementary materials: The 2019 Ridgecrest, California earthquake sequence: evolution of seismic and aseismic slip on an orthogonal fault system

Han Yue[1*], Jianbao Sun[2], Min Wang[2], Zhengkang Shen[1,3], Weifan Lu[1], Yijian Zhou[1], Lian Xue[1], Chunmei Ren[1], Mingjia Li[1], Thorne Lay[4]

1. Peking University, Beijing 100871, China

2. State Key Laboratory of Earthquake Dynamics, Institute of Geology, China Earthquake Administration, Beijing 100029, China

3. University of California, Los Angeles, CA, 90095-1567, USA

4. University of California Santa Cruz, Santa Cruz, CA, 95064, USA

The supplementary materials provide detailed information about data processing, data analysis, inversion techniques, and data fitting results not provided in the main text.

1. SAR image data processing

1.1. SAR phase data collection and processing for Ridgecrest earthquake sequence

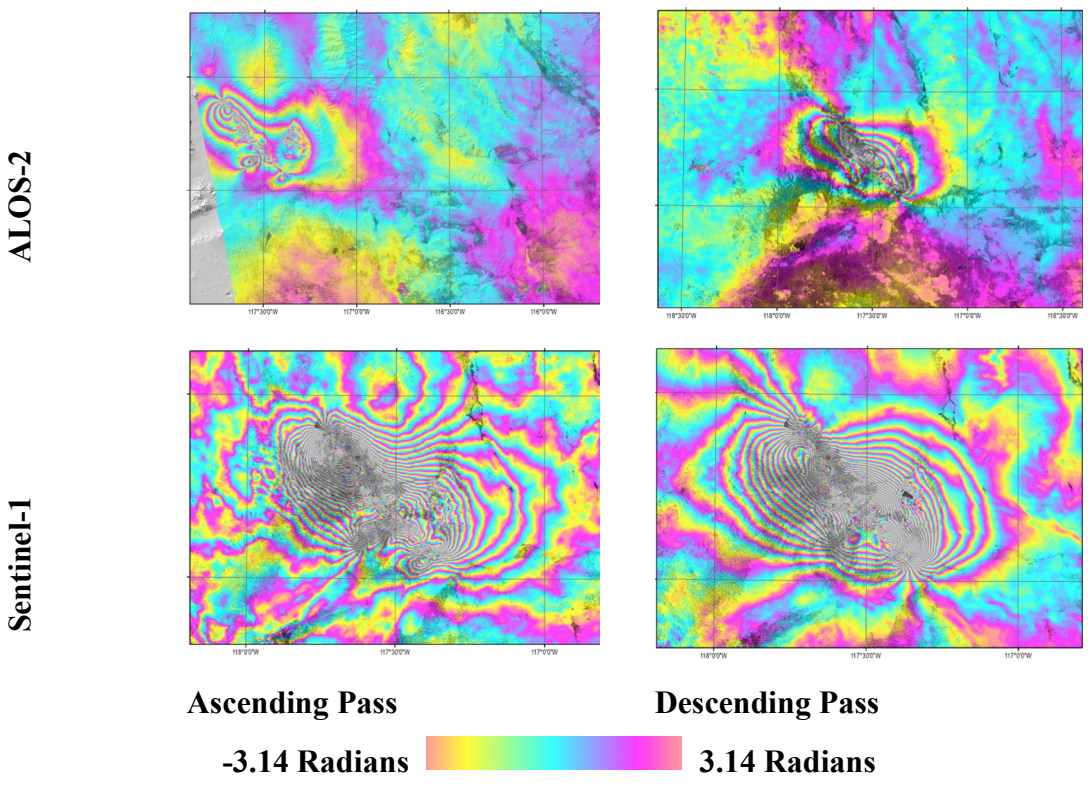

Fig. S1. InSAR data used. Wrapped and filtered InSAR phase data of ascending and descending pass data are plotted in each column, and images from ascending and descending orbits of Sentinel-1 (S1) and ALOS-2 satellites are plotted in each row, respectively. All images are plotted with the same color scale, note that the S1 wavelength is ~5.6 cm and ALOS-2 wavelength is ~23.6 cm.

The Ridgecrest earthquake sequence occurred in a region with dry condition and little vegetation coverage, and the area is ideal for Satellite Synthetic Aperture Rader (SAR) sensors to acquire detailed earthquake deformation, as the SAR signals are able to keep coherent even over a period of a few years. In this study, we use both the C-band SAR data from the Sentinel-1 (S1) satellites of the European Space Agency (ESA) and the L-band PALSAR-2 data of the ALOS-2 satellite from the Japanese Aerospace Exploration Agency (JAXA). The C-band S1 data are in the Image Wide mode, covering an area with 250-km width across the track and 300-km length along track for better capturing of the earthquake deformation and surrounding faults (two or three concatenated scenes), and the L-band PALSAR-2 data are in ScanSAR mode, covering an area of ~350×350 km^2. The data used in this study with their spatial baselines are listed in Table S1.

We use the Gamma software from Gamma Remote Sensing (http://www.gamma-rs.ch/) for InSAR data processing, a global optimization method for phase unwrapping (*21*), and the SRTM 1-arc-second DEM for image coregistration and topographic phase removal (Farr et al., 2007). The multi-look factors of 8 in range and 2 in azimuth are adopted for a spatial average of S1 SAR signals to suppress random noise, while the factors are 3 in range and 9 in azimuth for the ALOS-2 data considering their different imaging mode and spatial resolution. We use the DEM-assistant co-registration procedures for the coregistration of both kinds of satellite data, while the Enhanced Spectral Diversity (ESD) method is used for S1 data in the burst overlap regions. A Goldstein power spectrum filter is used for wrapped phase filtering. Then the filtered phase is unwrapped by the minimum-cost-flow algorithm. A line orbital ramp and a DEM-related phase are estimated and removed from the unwrapped phase. The final results are then geocoded into a grid of the original SRTM 1-arc-second DEM data. The possible

residual orbital ramps are further estimated in the joint inversion step after the data decimation process. The wrapped InSAR phases from both satellites are plotted in Fig. S2. The different fringe density between the ALOS-2 and S1 data is due to the differences in SAR wavelength, but the fringe patterns of the ascending or descending passes are similar to each other. The unwrapped phase of the S1 data lost some information in the near-field due to strong ground displacements near the fault zone, but it was limited within a narrow zone less than 1~2 km. The different fringe patterns in ascending and descending pass data clearly reflect a right-lateral dominated motion of the fault.

Because all of the SAR data were acquired before the July 4th, 2019 M_W 6.4 foreshock and after the July 6th, 2019 M_W 7.1 mainshock, the InSAR phases include the deformation of both major earthquakes and any deformation that occurred in the imaging intervals. It is impossible to separate the foreshock and mainshock deformation from the InSAR data, but we can see a small fringe pattern trending NE-SW at around 117.5° W and 35.6° N, especially in the descending pass data, which is related to the foreshock fault motion. For the S1 data in ascending pass A064 (Table S1), we processed two pairs of SAR data, but the June 28th, 2019 and July 10th, 2019 pair is preferred for fault slip inversion because of its shorter baseline than the July 4th, 2019 and July 10th, 2019 pair. The pair of ALOS-2 A065 track data acquired on Aug. 8th, 2016, and July 8th, 2019 with about a 3-year interval; however, it still shows great coherence over the whole region affected by earthquakes because of a short baseline of 2.3 m and the dry condition of the earthquake area. The tectonic motion related to the long time interval of orbit A065 are corrected using a linear ramp during the inversion process.

Table S1. ESA Sentinel-1 SAR data and JAXA PALSAR-2 SAR data used for the 2019 Ridgecrest earthquake sequence.

Track No.*	Baseline date	Interferometric pair date	Perpendicular baseline (m)	Used in inversion
A064#	Jul 4th, 2019	Jul 10th, 2019	-133.0	☒
A064#	Jun 28th, 2019	Jul 10th, 2019	-67.0	☑

D071[#]	Jul 4th, 2019	Jul 16th, 2019	30.4	☑
A065[$]	Aug 8th, 2016	Jul 8th, 2019	2.3	☑
D166[$]	Apr 2nd, 2019	Jul 23rd, 2019	-497.0	☑

*The letters' A' and 'D' denote the ascending and descending tracks of SAR missions.

SAR sensor of Sentinel-1 satellites from ESA.

$ PALSAR-2 sensor of ALOS-2 satellite from JAXA.

1. 2. SAR amplitude offset tracking for displacements of the Ridgecrest earthquake sequence

We use the offset-tracking technique (Strozzi et al., 2008) to detect the surface displacements produced by both the foreshock and mainshock of the RC earthquake sequence. We adopt the same multi-look factors as in the InSAR processing for keeping the same coordinator grids with the InSAR phase. A window of 256 or 128 is used for the image chip search for the ALOS-2 and S1 amplitude data, respectively. After the offset-tracking processing, a minor linear ramp is also estimated using the window searching result for removing any residual long-wavelength errors after SAR data coregistration. For ALOS-2 data, only subswath-1 and subswath-3 of the ScanSAR data are processed for the ascending and descending pass data, respectively. Then the final results are obtained as interferometric phases in the line-of-sight directions and the displacements in azimuth directions.

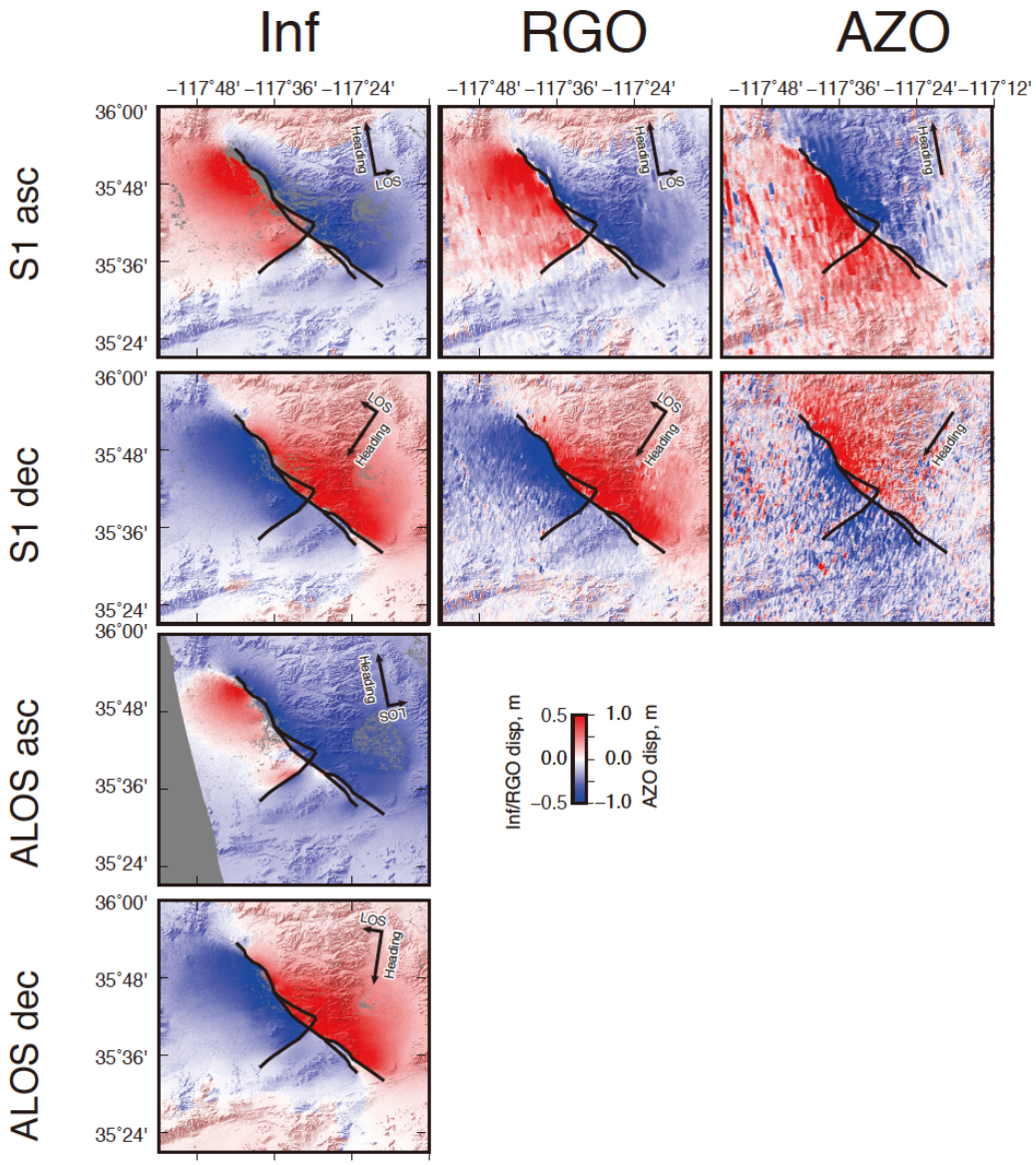

Fig. S2. Unwrapped SAR LOS interferometry, range offset (RGO), and azimuth offset (AZO) images. Images from ascending and descending orbits of Sentinel 1 (S1) and ALOS2 satellites are plotted in each row, respectively. Satellite heading and line-of-sight (LOS) directions of each image are marked. All the data are imaged with a blue-to-red color scale. Identified fault surface traces are plotted as black curves in each image.

3. Fault model reconstruction

We plot the spatial distribution of foreshocks and aftershocks at each depth range to visualize the event depth distribution. Most aftershocks are in the depth range of 5-15 km beneath the surface traces, suggesting a sub-vertical fault geometry.

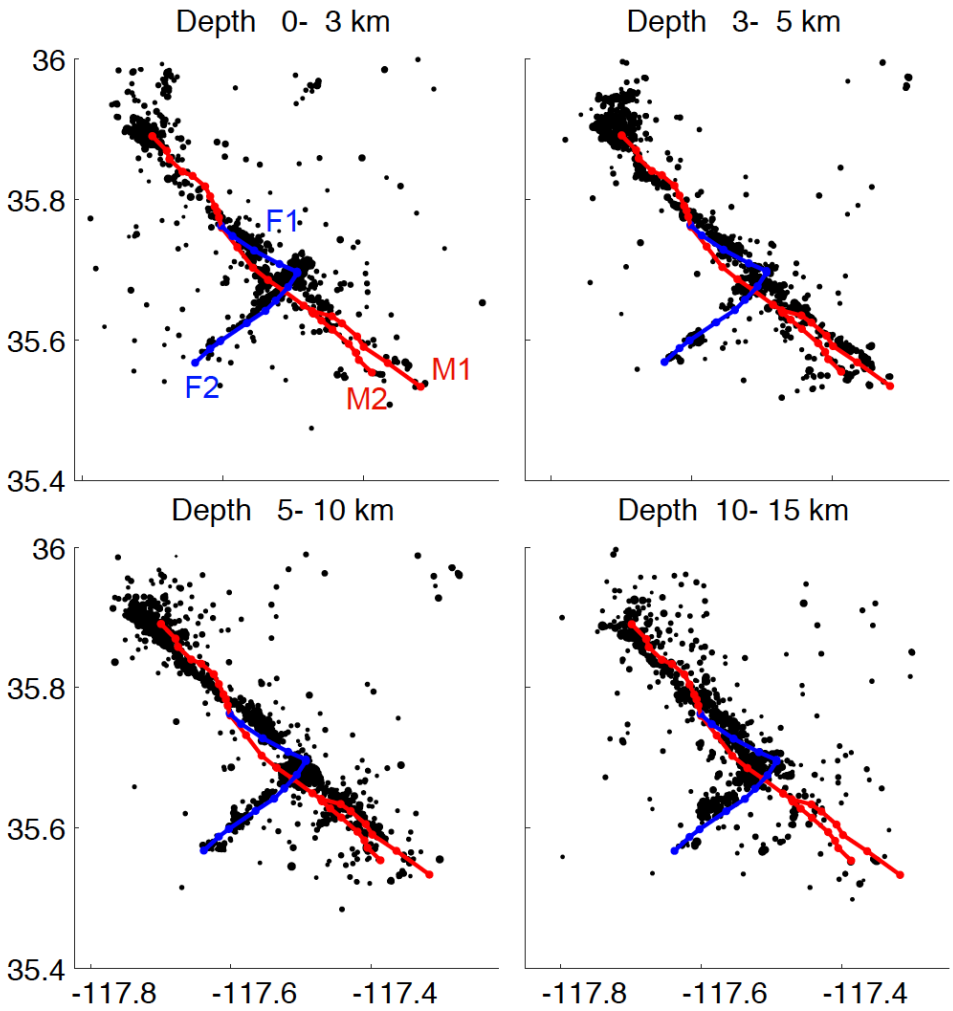

Fig. S3. Mapview of foreshocks and aftershocks lateral distribution at different depth ranges. Relocated events are plotted as black dots. Blue and red curves are fault surface traces identified as hosting the foreshock and mainshock, respectively.

A detailed fault geometry is required before performing modeling. In this study, we follow the same approach of Yue et al. (2017), relying on the field measured surface ruptures, synthetic aperture radar (SAR) images, and relocated aftershocks to determine a multi-segmented 3D fault geometry. The SAR images scan the source area with a high spatial resolution (tens of meters) and low temporal resolution (days of sampling interval); thus, they are particularly useful to determine the surface rupture traces and co-seismic slip distribution. Co-seismic ground displacements of

the RC earthquake sequence observed by SAR interferometry and azimuth offset are plotted in Fig. 2. These images essentially reflect the co-seismic ground displacement field projected to the satellite Line-of-Sight (LOS) direction. A two-regime ground displacement field is clearly revealed by these images, which is consistent with the right lateral sense of motion of the mainshock. These images reflect various localized ground deformation patterns related to the complexity of fault structures.

Plenty of surface offsets can be used to parameterize the fault model, though many of them could be shallow slip triggered by the mainshock. Including these trivial structures provides limited information to the mainshock rupture process. Furthermore, including small surface ruptures expands the model space to explore, which is inconvenient for inversion and parameter tuning. We require the fault model to capture major rupture pattern without emphasizing secondary surface ruptures to keep both the representativity and simplicity of the slip model. Thc criteria are considered when removing secondary fault traces are:

(1) traces less than 5 km long,
(2) traces located more than 5 km from the main fault
(3) traces with limited seismicity lineation.

We identify four major surface rupture traces from field observations and SAR images and use them to parameterize the fault plane. We consider these four traces as major faults hosting the foreshock and mainshock. We assume that most aftershocks occurred on the same fault planes of the foreshock and mainshock ruptures and use the aftershock locations to determine fault geometries at depth. The foreshocks occurred on two fault segments, both showing about 10 km lateral extent and forming an orthogonal structure. This structure mirrors two fault traces identified by SAR images at the surfaces (F1 and F2). The aftershocks cover a larger lateral extent (~30 km) across the main fault zone. There is a clear branching structure at the southern end of aftershock locations, which also mirrors the rupture branch images at the surface. With this mirroring between surface ruptures and aftershock distribution at depth, it is relatively easy to construct 3D fault structures for both the foreshock and mainshock ruptures. We draw four curvature lines following aftershock locations at

8-13 km depth and use them as the fault traces at depth. We then associate each trace at depth with a rupture trace at the surface to form a fault plane. We finally parameterize a 3D fault system composed of four segments (Fig. 2). The orthogonal fault structure (F1 and F2) hosts the M_W 6.4 foreshock and the following foreshocks. The mainshock is assumed to occur on two NW-SE trending faults (M1 and M2), where M2 is a smaller branch at the SE end of M1. Though the surface trace of segment M1 is curved toward SW in its central segment, its profile at depth is relatively straight.

Aftershock seismicity shows a more lineated structure at depth, which can be better visualized with depth profiles (Fig. S4). At the central segment of M1, F1 is subparallel to M1, there is one lineated aftershock distribution at about 10 km depth, and we choose this profile as the shared root between F1 and M1. This parameterization strategy essentially assumes M1 and F1 merge at 10 km depth, while the surface ruptures are the splaying structures of the same fault system. The merging depth cannot be precisely inferred from aftershock locations, and assuming a different merging depth leads to different dip angle of M1 in the central segment, with shallower merging depth implying shallower dip angle. We test parameterizing the fault model with a merging depth from 6 km to 14 km and find that different fault models yield similar slip pattern and fitting to the data (Table. S2). We finally choose a merging depth of 10 km, which appears to be most consistent with the aftershock distribution.

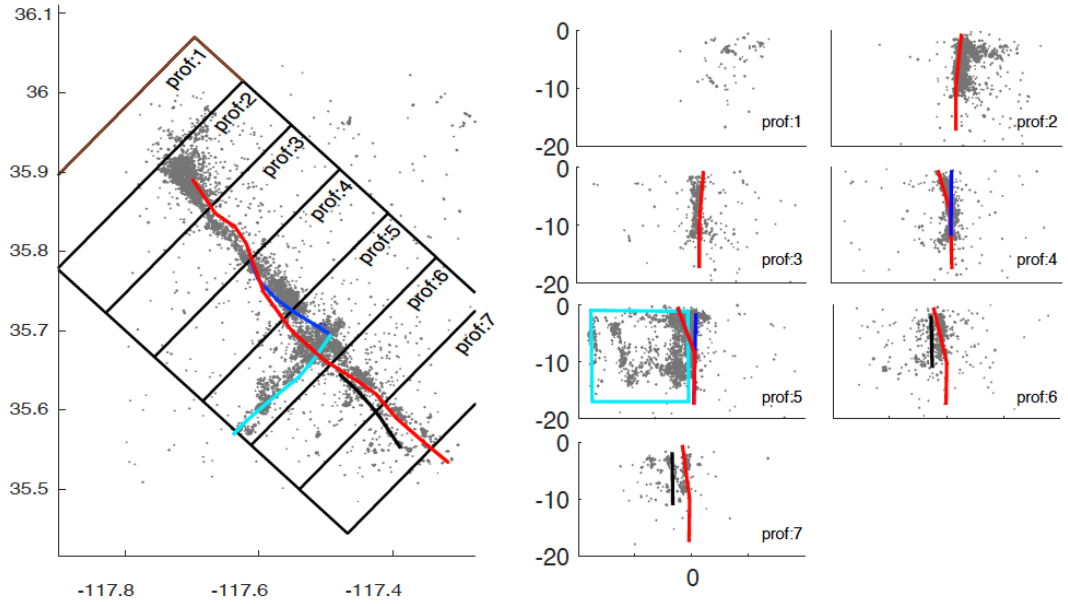

Fig. S4. Fault structure and seismicity. The left panel shows the map view of foreshock and aftershock locations. Surface fault traces are plotted as colored curves. Fault plane and aftershocks are projected along seven profiles, and their boundaries are plotted as black rectungles. The depth distribution of aftershocks and fault model for each profile are plotted in the right panel, respectively.

F1 & M1 Merging Depth	hr-GNSS	SM	GNSS	SAR
6 km	51.3%	48.2%	8.8 %	31.76%
10 km	51.3%	47.7%	8.5%	32.8%
13 km	51.3%	47.5%	8.5%	33.24%
17 km	51.8%	47.9%	9.1%	31.25

Table S2. RMS ratio to different data in terms of RMS ratio using different merging depths of F1 and M1.

SAR images and aftershock branches indicate other possibilities of fault model parameterization, and we test several different fault structures and combinations with different dip angles. We find that the current fault model performs the best in the source inversion. F1 and M1 segments share the same root at ~10 km depth and also the same surface trace north of 35° 45′ N; thus F1 and M1 essentially overlap at the NW end of F1. The M_W 5.4 foreshock occurred at this location. We choose F1 instead

of M1 as the source fault to invert for the afterslip following the M_W 6.4 foreshock here, since the M_W 5.4 foreshock and slow-slip are considered components of the post-seismic deformation on the ruptured fault F1 following the M_W 6.4 foreshock. Information of the fault geometry is listed in Table S3. The sub-fault geometrical parameters, i.e. strike/dip angle and sub-fault dimension, are adjusted with respect to the location of surrounding sub-faults. The rupture velocity is determined using "L" curves and described in the later sections. Fault parameter construction methodology is also described in the method section.

Table S3. Co-seismic fault rupture model.

	#of subfaults along strike/dip	Lateral extend of each segment (lat / lon/dep)	Maximum depth (km)	Fault dimension (in km) along strike/dip	hypocentral location (lat/lon/dep)	Rupture Velocity (km/s)
F1	8/5	35.54-35.88/ -117.70-117.32	17.4	16/14	35.69/-117.50/10	2.2
F2	8/8	35.52-35.64/ -117.47-117.36	11	16/20	35.69/-117.50/10	2.2
M1	25/8	35.70-35.78/ -117.61-117.50	12.8	50/20	35.77/-117.60/10	2.0
M2	6/4	35.58-35.69/ -117.63-117.50	16.8	15/12	35.71/117.56/5	2.0

4. GNSS static co-seismic displacement fields

4.1. Static GNSS solutions

The M_W 6.4 foreshock and M_W 7.1 mainshock of the Ridgecrest earthquake sequence occurred on July 4 and July 6, 2019, respectively, separated by 34 hours. We process GNSS data of July 2 to July 7 from 240 continuous stations in the region of (121.5^o—114.5^o W, 32.5^o—38.0^o N) to derive the co-seismic displacement fields associated with the two events. Data from another six stations (COT1, ECHO, FERN, GOSH, QUIN, and PALX) located outside of the above area are also included in the processing to help determine the reference frame. The IGS precise ephemerides of satellites are used in the data processing.

The data processing is carried out using the GAMIT/GLOBK software package (Herring et al., 2010a, b). We first process the data to produce four daily solutions of July 2, 3, 5, and 7, and 4 sub-daily solutions of July 4 and 6. Epochs of the sub-daily solutions are separated at the times of earthquake occurrences. All the solutions are loosely constrained. We then rename the sites affected by an event for the solutions after the event and use GLOBK to combine all the daily and sub-daily solutions and tie the combined solution to the ITRF2008 reference frame by performing a seven-parameter transformation of 6 fiducial station positions. In the GLOBK solution, the baseline between two positions of the same site displaced by an event is the co-seismic displacement of that site. The final co-seismic displacement solutions

231 are obtained after several iterations run. In each run, we check if a station should be
232 renamed or have the original name restored depending on the significance of its
233 co-seismic displacement or its neighborhood co-seismic displacements. Such a
234 practice helps resolve subtle co-seismic displacements and establish a reliable
235 reference frame for the solution.
236
237 We derive the co-seismic displacement fields of the M_W 6.4 foreshock and M_W 7.1
238 mainshock under the assumption that there is no significant deformation between the
239 two events. In fact, an M_W 5.4 foreshock that occurred on July 5 might have produced
240 noticeable co-seismic displacements. We use the data observed between the M_W 6.4
241 foreshock and M_W 7.1 mainshock to detect possible deformation. The result shows no
242 significant co-seismic displacements at the 2 mm uncertainty level. Furthermore, we
243 also analyze the post-seismic deformation of 2 days following the mainshock, and the
244 result shows that the largest post-seismic displacement is ~2 mm at the station P595.
245 This result confirms that the post-seismic deformation has virtually no effect on the
246 co-seismic displacement solution we have obtained.
247
248 *4.2. High-rate kinematic GNSS solutions*
249
250 Most of the GNSS stations in the study region have high-rate (1-sec sampling) data
251 recorded. We use the TRACK module of the GAMIT/GLOBK software package to
252 generate 1-hour high-rate kinematic GNSS solutions associated with the M_W 6.4
253 foreshock and M_W 7.1 mainshock. The kinematic data processing scheme includes the
254 estimation of temporal variation of station positions and tropospheric delays as
255 stochastic random-walk processes and solution of carrier-phase ambiguities. We
256 adopt IGS precise satellite ephemerides, station pre-earthquake positions, and total
257 atmospheric delay estimates obtained from the static processing to help estimate
258 ambiguities and constrain tropospheric delays. The IGS ionospheric delay model is
259 also used to reduce the disturbance caused by the ionospheric delay.
260
261 TRACK follows the GAMIT processing mode and uses the double-difference
262 observations to model the carrier-phase data. Therefore, the distances from the
263 reference station to the "roving" stations and the data quality of the reference station

are critical. After tests of several candidate stations, we choose the stations B623 and P508 as the reference stations for the kinematic solutions of the M_W 6.4 foreshock and M_W 7.1 mainshock, respectively. Station B623 is about 310 km away from the epicenter of the M_W 6.4 foreshock, and no obvious seismic signal was observed at the station. Station B508 is about 340 km away from the epicenter of the M_W 7.1 mainshock, and the seismic signal common to all the "roving" stations arrived at the station ~100 sec after the event, which is beyond the time window we finally use to select data included in the inversion. Finally, we obtain the kinematic solutions of 5 and 25 stations for the two events, respectively.

The formal errors for the kinematic solutions are about 20, 20, and 40 mm for the east, north, and up components, respectively. We also estimate the static offsets for the kinematic solutions using time-series before and after the seismic signals. Comparison between the static offsets from the kinematic solutions and the static co-seismic displacements reveals that except for the station CPBN, the differences are within a few millimeters for the horizontal and less than 3 cm for the vertical components, respectively. These differences are not systematic, indicating again that the static co-seismic displacement fields do not contain significant post-seismic deformation, and our formal error estimates are large enough. The north and vertical differences of the station CPBN for the mainshock are about 15 mm and 75 mm, respectively, which may be due to a serious multipath effect at the site.

5. Joint inversion of rupture processes

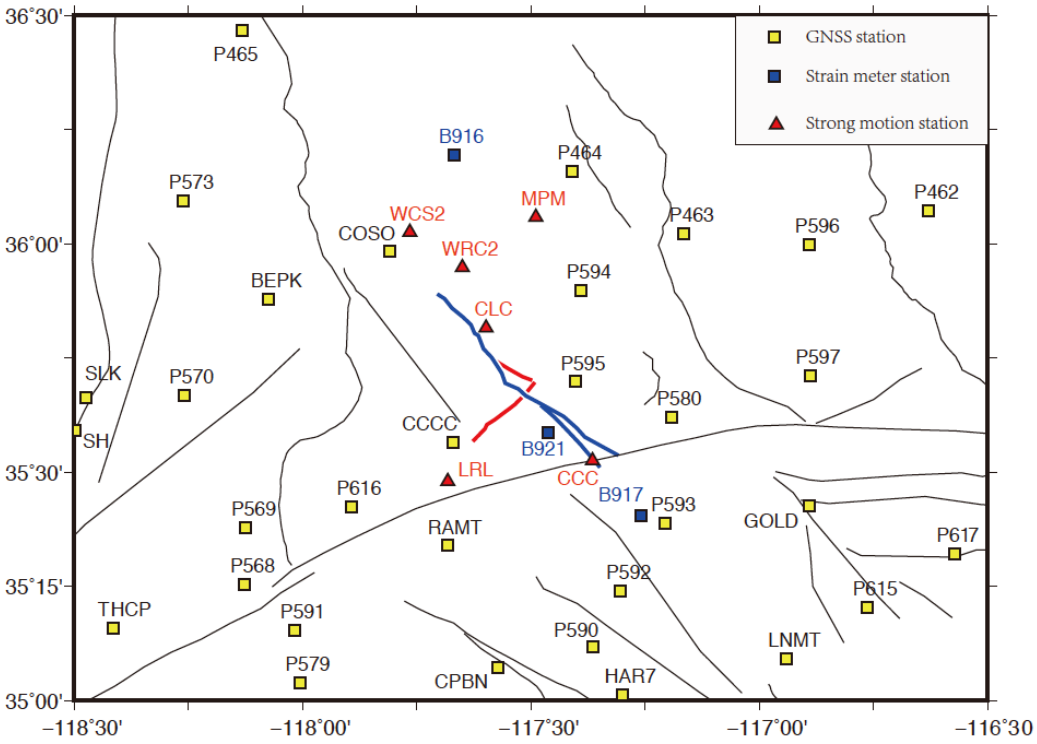

Fig. S5. Distribution of stations whose data are used in inversion. GNSS, strong motion, and strainmeter stations are plotted as yellow filled squares, blue filled squares, and red filled triangles, respectively. Regional fault traces are plotted as thin black curves. Foreshock and mainshock surface traces are plotted as blue and red curves.

Seismic waves of both the M_W 6.4 foreshock and the mainshock were recorded at regional strong-motion and high-rate GNSS (hr-GNSS) stations, and their static co-seismic displacement fields are measured by GNSS and SAR. We perform a joint inversion to exploit the temporal and spatial resolution of all the data and achieve the highest spatial and temporal resolution (Yokota et al., 2011). Among all the available data sets, SAR images provide the highest spatial resolution; however, the deformation fields of the M_W 6.4 foreshock and the mainshock are not separated in SAR images, introducing a challenge of using the SAR data together with other data in source inversion. Based on a traditional multi-time-window inversion algorithm (Hartzell and Heaton, 1983), we further develop a joint inversion algorithm. This

algorithm uses waveform and GNSS static displacement data to constrain the dynamic rupture process of individual events, while still keeping summation of their co-seismic displacements to be consistent with InSAR observations. We parameterize the ruptured faults as the foreshock (m_{fore}) and mainshock (m_{main}) segments, and use the multi-time-window algorithm to parameterize the rupture process as a sequence of triangles in the time domain. We then calculate Green's functions of each observation or each inversion parameter. The Green's functions are then constructed as partial derivative matrices (Gmat) for inversion. For typical isolate earthquakes, the inversion problem could be formularized as G_{mat}*m=d, and be inverted with a non-negative linear-least-square approach. For the joint inversion including rupture parameters for both main and foreshocks, we concatenate G_{fore_SAR} and G_{main_SAR} in the row-direction; thus they both contribute to the SAR observations (d_{SAR}). For other observations, we place the G_{fore} and G_{main} in the diagonal of the inversion matrix, thus their contributions to individual datasets (d_{Fore_dyn}) and (d_{main_dyn}) are accounted for separately. The structure of the Green's function matrix is summarized in Fig. S6. With this construction, the rupture process of the foreshock and mainshock (m_{fore} and m_{main}) can be inverted at the same time.

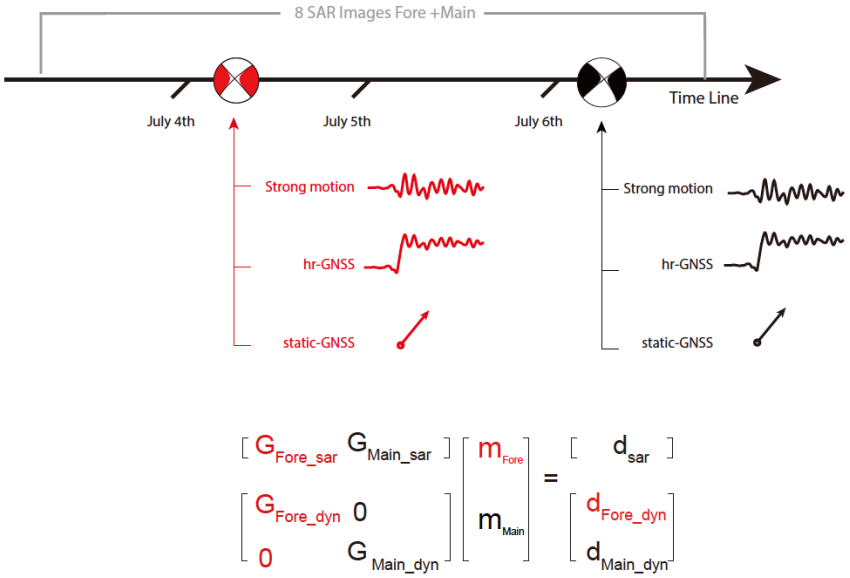

Fig. S6. Schematic view of the inversion algorithm. The M_W 6.4 foreshock and the mainshock and associated observations are plotted in the same time-line. Dynamic (strong motion and hr-GNSS) and static (static GNSS) observations are available for each earthquake, respectively. 8 SAR images record the total ground deformation field of the sequence. The inversion matrix is constructed as equations shown at the bottom. Slip models of foreshock and mainshock contribute to the SAR observation through concatenated Green's function in the matrix. Foreshock and mainshock models contribute to other observations through associated Green's functions at the diagonal positions of the GF matrix.

It is noted that the foreshock magnitude is smaller than that of the mainshock by 0.7, corresponding to about ten times difference in the magnitudes of coseismic displacements and seismic waves. The waveform data input for the foreshock is also much less than that of the mainshock. Thus in the inversion the contribution from the waveform data of the mainshock would be much larger than that of the foreshock, and the inversion would tend to amplify the errors of the foreshock if no correction is made. We therefore amplify the weight for m_{fore} and the foreshock waveform observations (d_{fore_dyn}) by five times in inversion, thus the weighting for foreshock waveform data is up to a similar scale as that of the mainshock in inversion. The weighting for the foreshock InSAR data remains the same. A full formulation of the Green's function matrix construction is expressed as:

$$\begin{bmatrix} [G_{fore\_sar} & G_{main\_sar}] \\ wt_f * G_{fore\_dyn} & o \\ o & G_{main\_dyn} \end{bmatrix} \begin{bmatrix} m_{fore} \\ m_{main} \end{bmatrix} = \begin{bmatrix} d_{sar} \\ wt_f * d_{fore\_dyn} \\ d_{main\_dyn} \end{bmatrix} \quad \text{(S1)}$$

We test different values of wt_f and find that the choice of the foreshock weighting parameter doesn't significantly impact the inversion result, as long as the scaling factor is similar to the moment difference of the foreshock and mainshock.

We use three-component ground displacement recordings of 20 and 4 hr-GNSS stations for the mainshock and foreshock, respectively. Original ground displacement waveforms are filtered with a band-pass filter of 0.02 - 0.25 Hz, to remove the static displacements, which show as steps (Yue et al., 2017). The band-pass filtered waveforms are then cut at 50 s after the earthquake initiation and down-sampled at 2

points per second. Green's functions of the hr-GNSS data are computed with a wavenumber-frequency integration method (Zhu and Rivera, 2002) and the same band-pass filtering is applied to the Green's functions. Green's function computation utilizes a local velocity model interpolated from the SCEC Southern California Community Velocity Model (UCVMC, CVM-H) (Wang et al. 2006). The same model is used to compute strong motion and static Green's functions.

We use three-component ground acceleration recordings of 6 strong motion stations for both foreshock and mainshock in the inversion. The strong motion stations are operated by the Southern California Seismic Network (SCSN) and data were archived at the Southern California Earthquake Data Center. The original ground acceleration data are integrated to produce ground velocity and then band-passed filtered. For stations located on the sedimentary basin and showing strong resonance waveforms, e.g. SRT, TOW, and GSE, we adopt band-pass frequencies of 0.05 - 0.15 Hz to reduce the resonance effect. We use the same frequency-wavenumber integration method to compute Green's function for strong motion data.

We use three-component ground displacements recorded at 34 GNSS stations for both the foreshock and mainshock in the inversion. Green's functions for static ground displacements are computed using a layered model integration method (Wang et al. 2006). Eight SAR images from both ascending and descending orbits of Sentinel 1 and ALOS 2 satellites are used in the inversion. We down-sample the displacement images using model resolution based algorithms to ensure finer sampling near the fault traces (Yue et al. 2017). 7954 sample points are used in the final inversion.

We adopt an empirical technique to determine the relative weighting between different datasets (*Yue et al. 2017*), which ensures balanced information and weighting in all datasets. In such configuration, we set the weight of one reference data (e.g. static GNSS) to be 1 and determine the relative weighting with respect to the other dataset sequentially using a broad range of relative weighting (0.1~10). An optimized relative weighting can be selected at the bottom of the “U” shaped total RMS curve, which is computed by the product of the respective RMS of each dataset. This algorithm can recover the optimized relative weighting under a numerical test,

when assuming uncertainty of both data are normally distributed, and has been successfully adopted in several previous studies.

We determine rupture velocity by testing inversion with different rupture velocities, and find the turning point of the "L" shaped curve (Fig. S7) (Yue and Lay, 2013). The optimal rupture velocity is determined to be ~2.2 km/s and 2.0 km/s for the mainshock and M_W 6.4 foreshock, respectively. We find no evidence of super-shear rupture velocity. Fitted data from the inversion model are plotted in Fig. S9-S16 below.

We achieve about 50% and 53% variance reduction of the residual root mean square (RMS) for hr-GNSS and strong motion data, respectively. For static GNSS data, we achieve 9% of RMS reduction. Data fitting to SAR images varies by different imaging techniques, which is shown in Fig. S14. The standard deviation of interferogram and range offset residual is close to 10 cm. The standard deviation of azimuth offset residual is close to 20 cm.

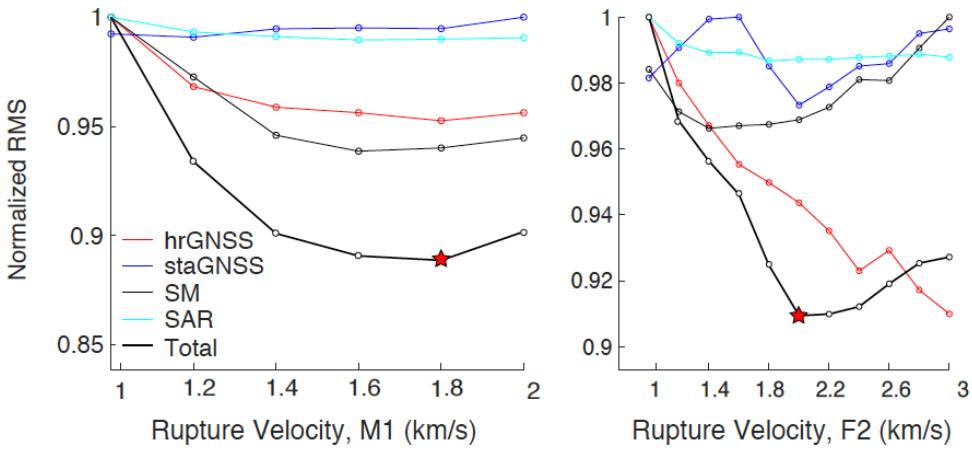

Fig. S7. Root mean square of data fitting residuals vs. rupture velocity for foreshock and mainshock planes are plotted in the left and right panels, respectively. Normalized RMS of hr-GNSS, static-GNSS, strong motion, InSAR, and all combined are plotted in different colors.

We adopt Laplacian regularization to the slip model and different levels of smoothing factors are tested (Fig. S8). The area of slip concentration is stably revealed in all smoothing level results, though the peak slip is reduced and the slip patterns are smeared with a greater level of smoothing. The smoothing parameter is selected to be the inverse of the Laplacian operator, thus patches with smaller Green's function amplitude are loosely smoothed. RMS of each trade-off curve is normalized by the largest RMS in the smooth search values and their products are calculated to represent the total RMS (Fig. S8). We choose the smoothing level near the turning point of the residual curves as the optimized smoothing.

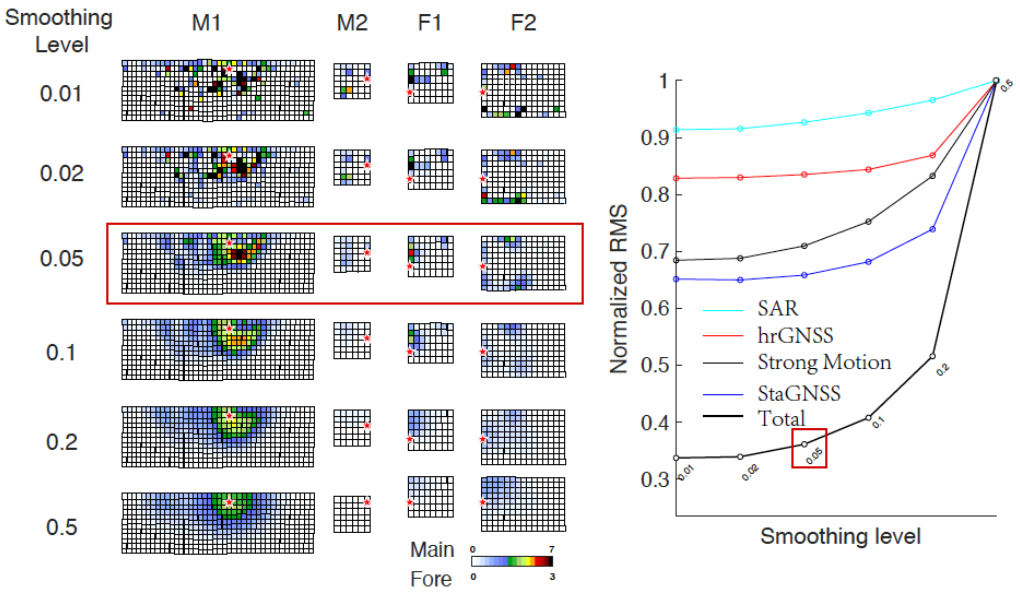

Fig. S8. Slip pattern vs. degree of smoothing. Left panel: slip patterns on fault planes inverted under different levels of smoothing. Right panel: the relative ratio of residual RMS for solutions inverted using different levels of smoothing. The colors of curves denote the data types used in the inversion.

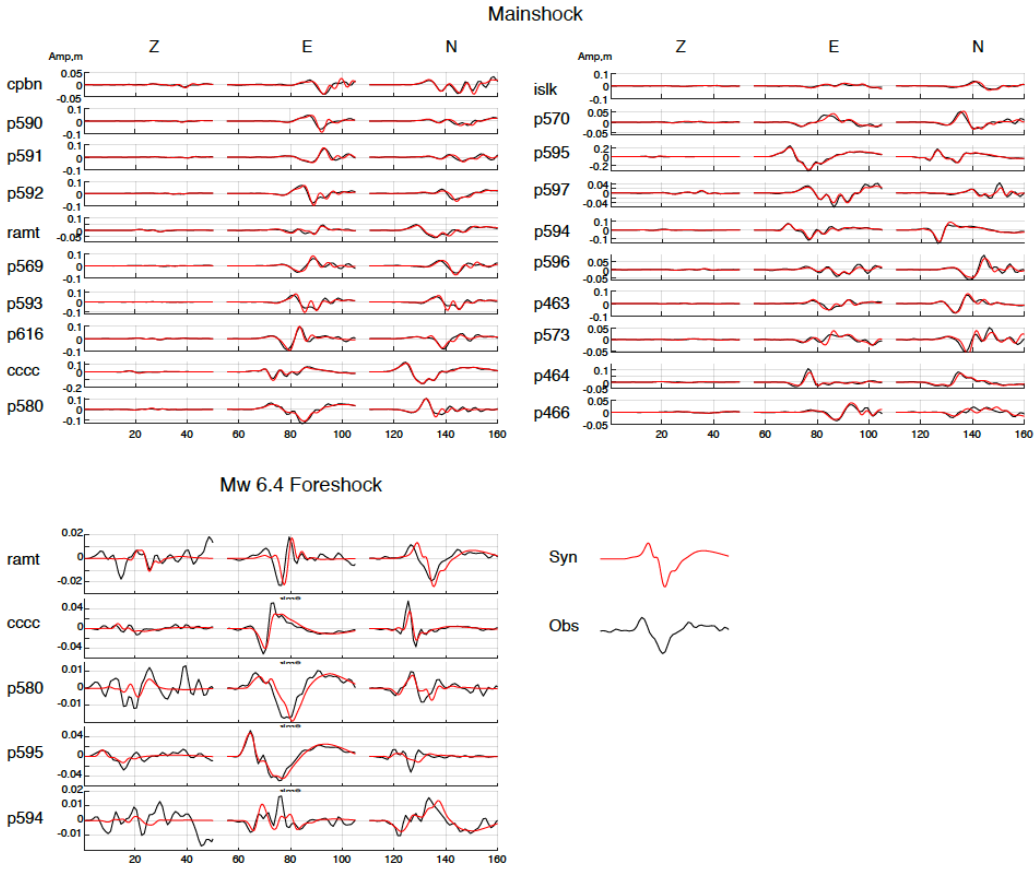

425

426 **Fig. S9.** Data fitting of hr-GNSS waveforms. Results for the mainshock and M_W 6.4
427 foreshock are plotted in the top and bottom panels, respectively. Three-component
428 ground displacement waveforms are shown. Observed and synthetic waveforms are
429 plotted in black and red, respectively.

430

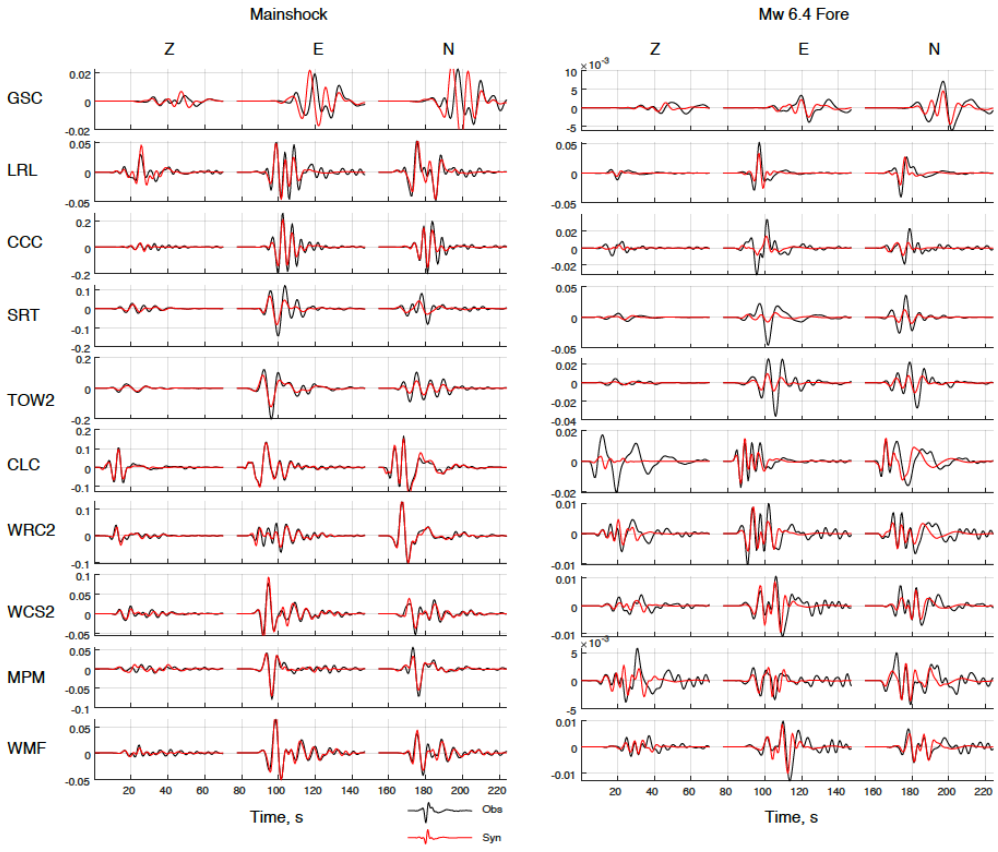

Fig. S10. Synthetic waveform fits to strong motion waveform data. Data fitting results for the mainshock and M_W 6.4 foreshock are plotted in the left and right panels, respectively. Three-component ground displacement waveforms are shown. Observed and synthetic waveforms are plotted in black and red, respectively.

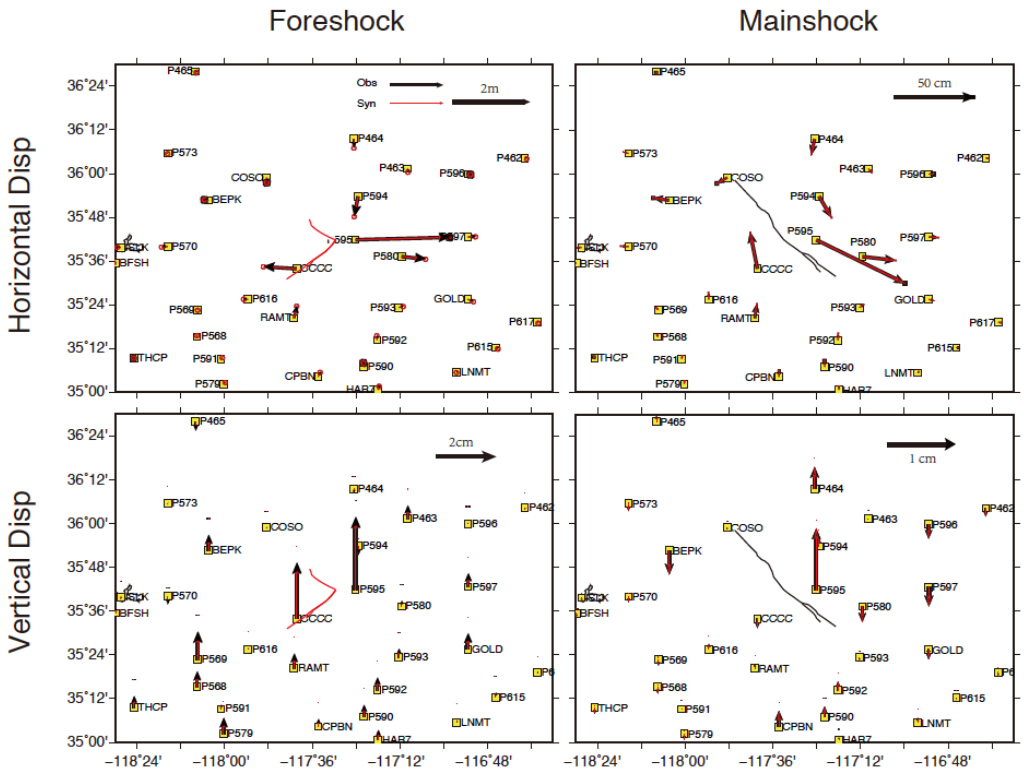

Fig. S11. Static-GNSS ground displacement data fitting results. The left and right panels are for the M_W 6.4 foreshock and mainshock, respectively. Horizontal and vertical ground displacements are shown in the top and bottom rows, respectively. Observed and synthetic ground displacements are plotted in black and red arrows. Notice the scale difference for displacements in each diagram.

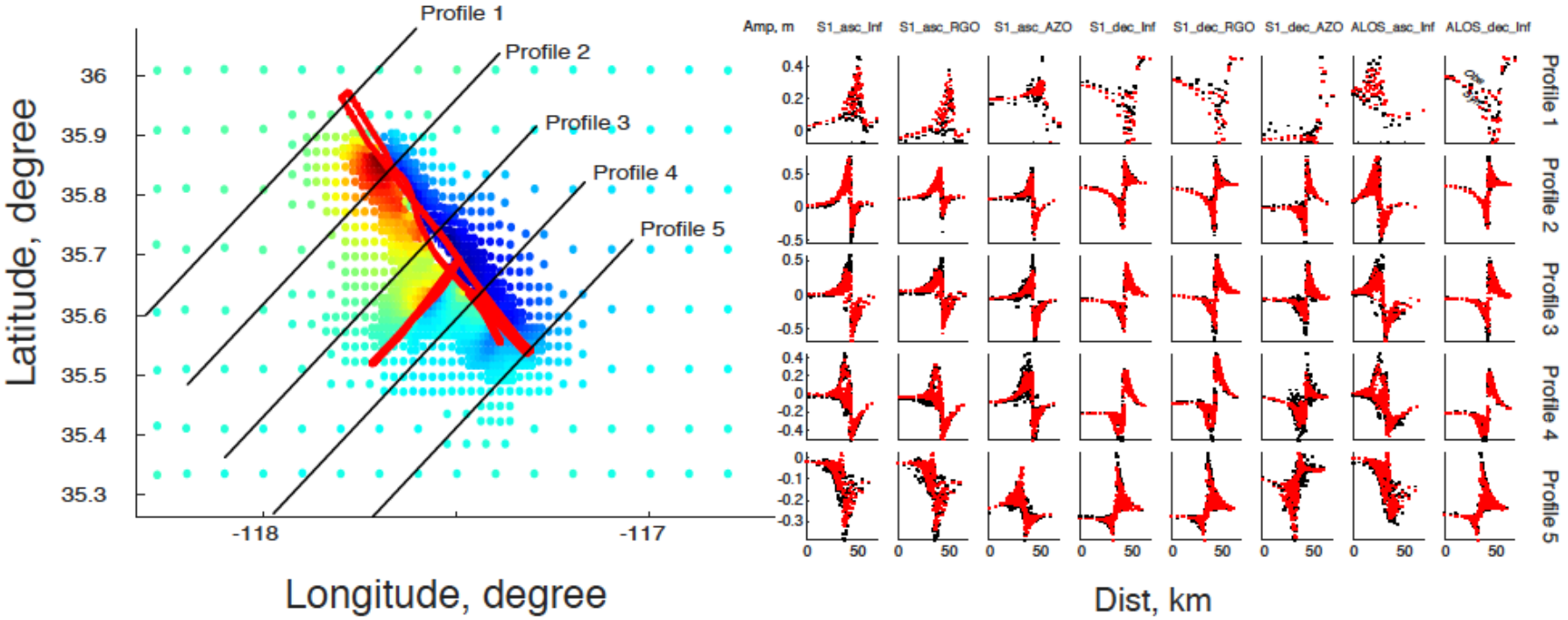

Fig. S12. SAR image data fitting. The SAR observed ground displacement data are plotted along profiles in the strike normal directions. Locations of 5 profiles cutting the mainshock fault traces are plotted in the left panel. Ground displacements of S1 asc INF are plotted in left panel as colored dots in the background. Observed and synthetic ground displacements are shown as black and red dots in right panel. Data along each profile are plotted in the corresponding row. Data from each orbit are plotted in the corresponding column.

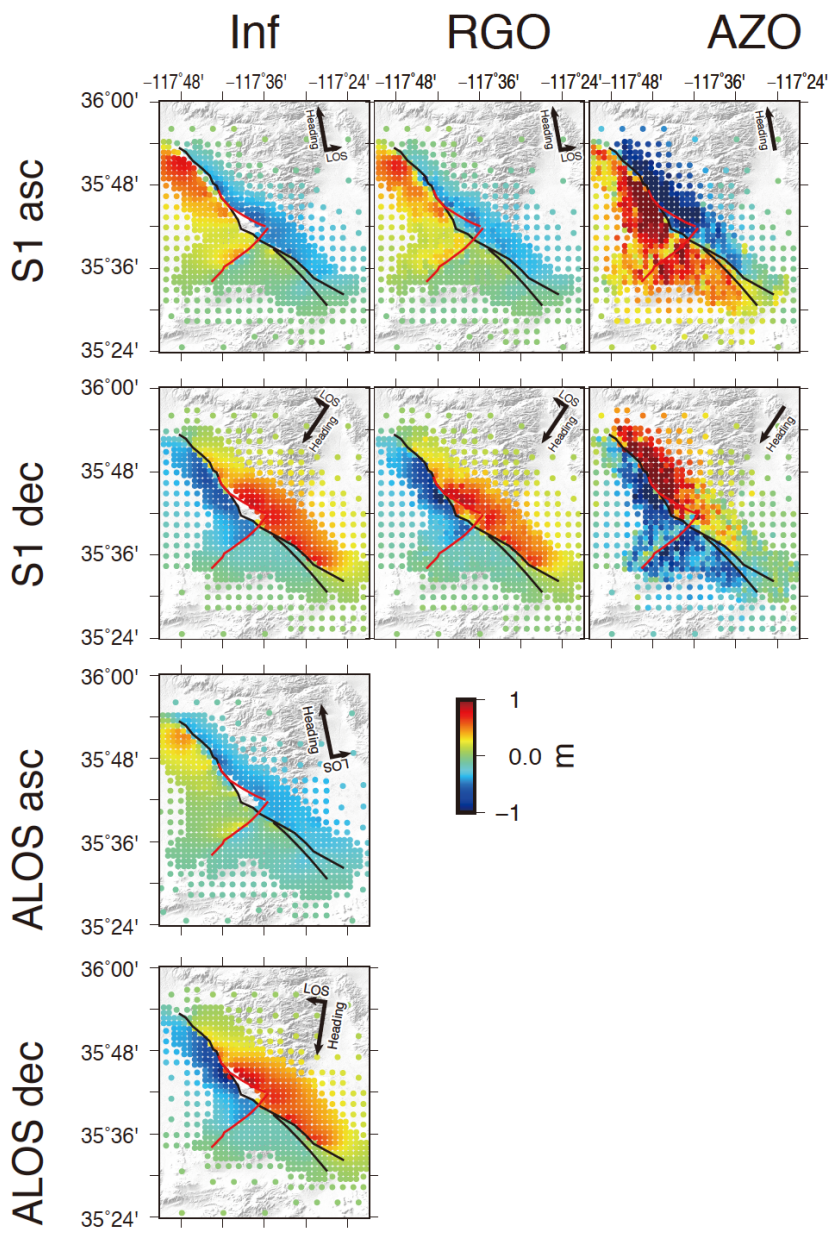

Fig. S13. Observed SAR images. The data are sampled with a resolution based sampling method and plotted for interferometry, RGO and AZO orbits in each column. Images of each satellite are plotted in each row. Satellite heading and looking directions are shown in each image. In each Fig., surface fault traces for the mainshock and the M_W 6.4 foreshock are plotted as black and red curves, respectively.

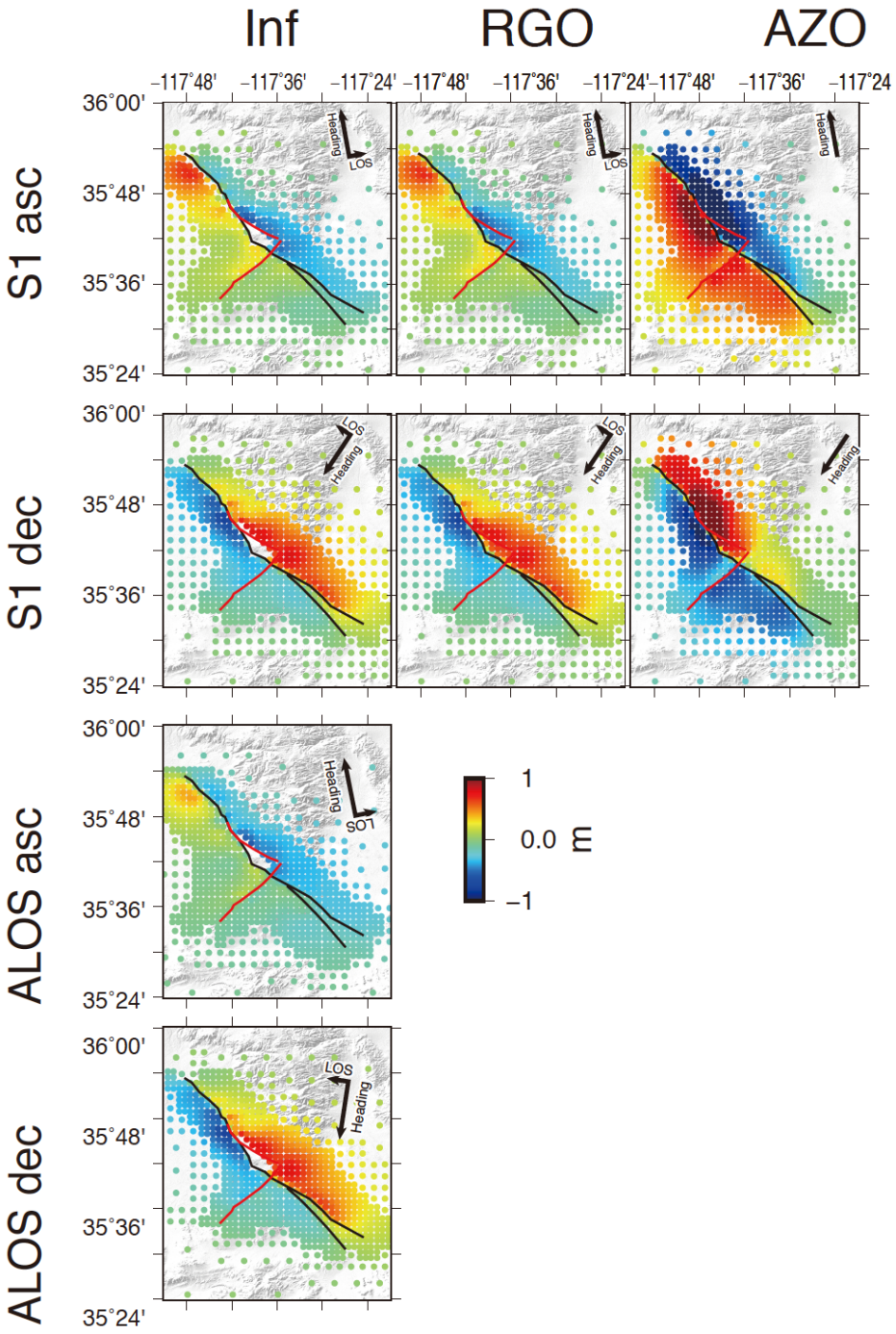

Fig. S14. The same as Fig. S13 except for synthetic SAR images.

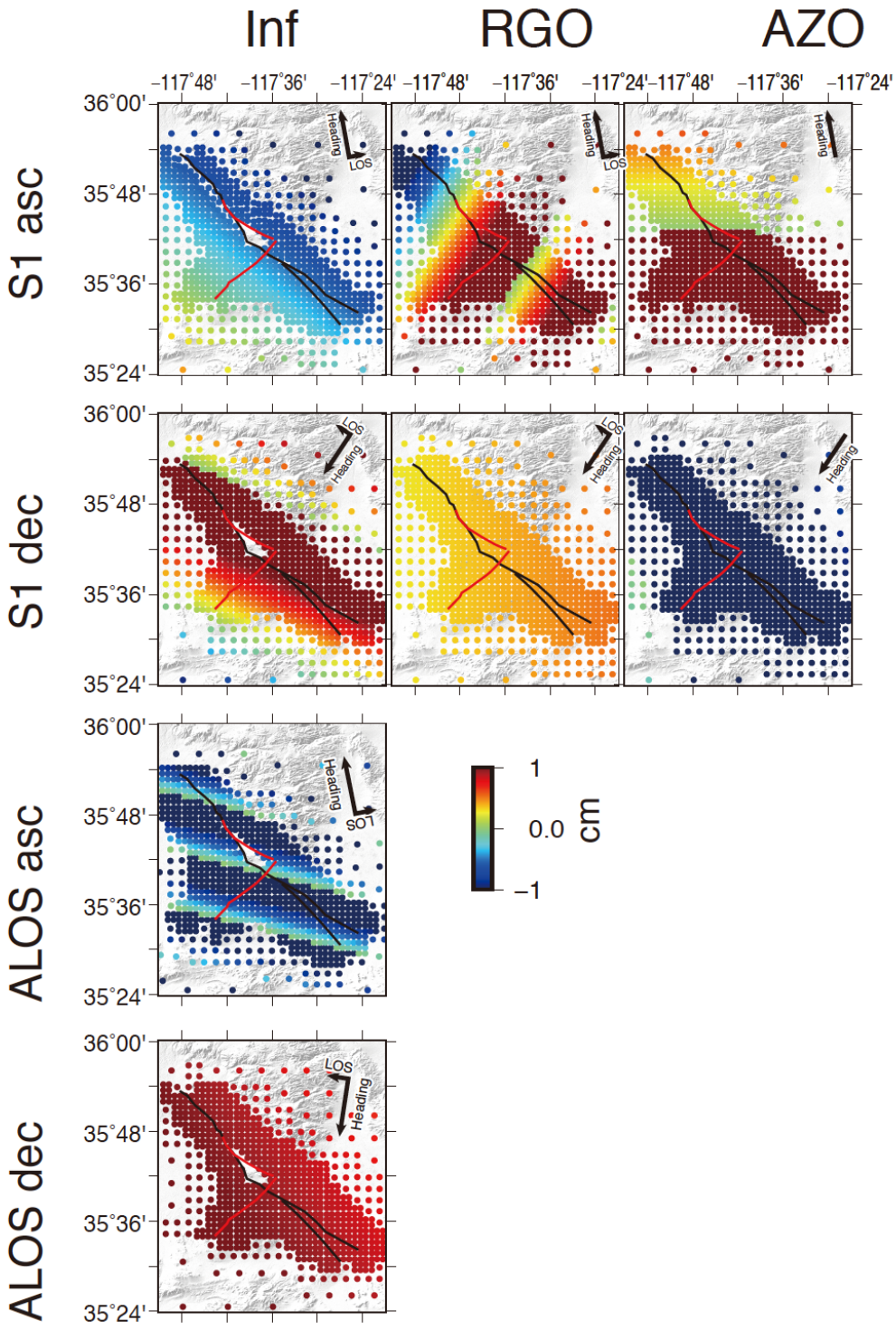

459

460 **Fig. S15.** The same as Fig. S13 except for synthetic orbits of satellites.

461

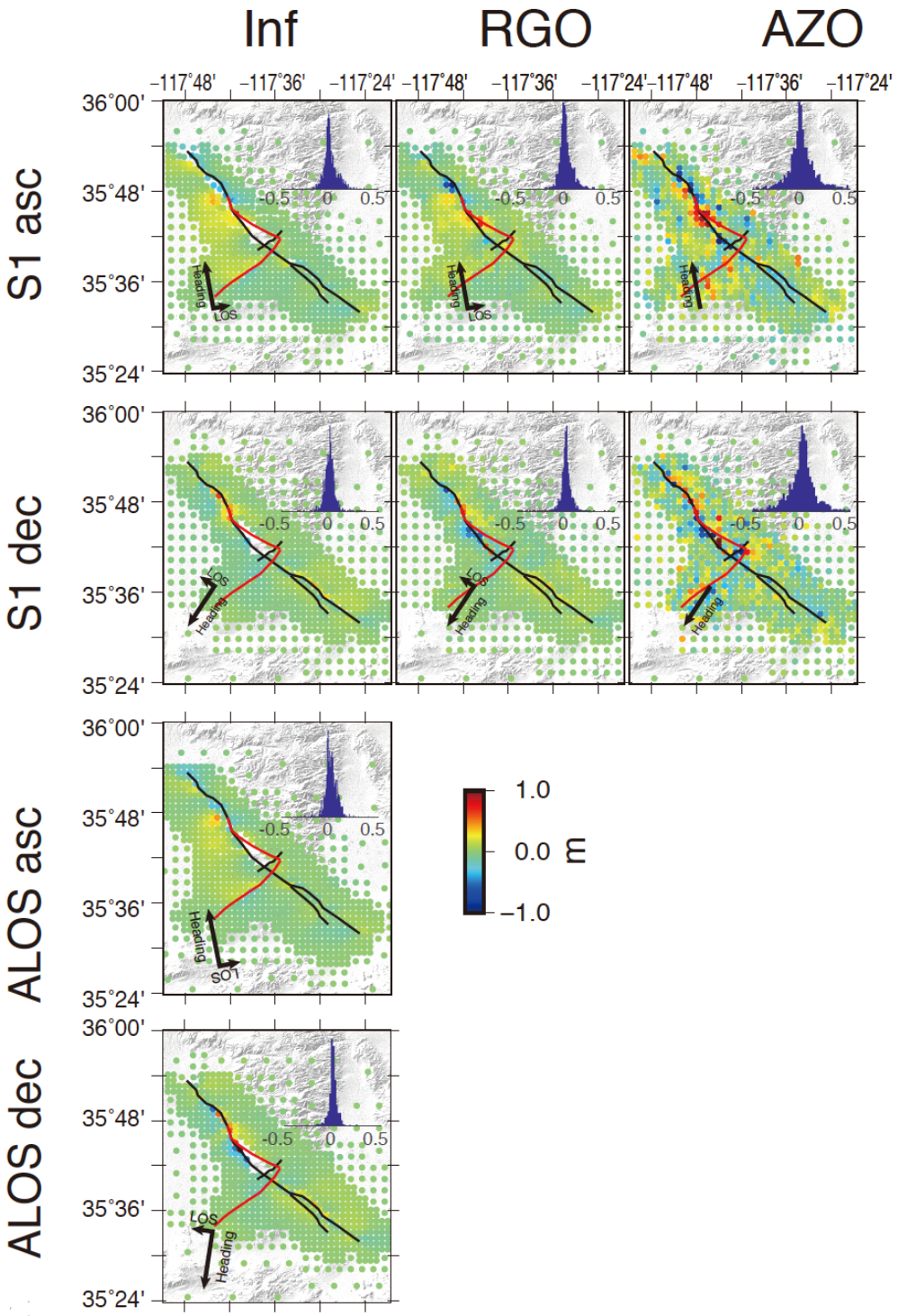

Fig. S16. The same as Fig. S13 except for SAR data post fit residuals. The inset plots are the histograms of residual statistics (in cm).

We also calculate the co-seismic ground displacements of several near field stations and compare them with the campaign GPS displacements (Floyd et al. 2020). Because only lateral displacements are available for these stations, it is not convienent to put them in the joint inversion scheme, so we rely on the forward modeling as a validation test of our slip models. The foreshock displacements are well predicted at 6 near field stations. The predicted and observed mainshock displacements show some discrepancy. The discrepancy is most significant at station PNCL, which is a near fault site. Because the near fault displacement may not be well presented by an elastic medium model, we exclude SAR sample points near the fault trace, thus it is anticipated that the very near fault displacement can not be well predicted. At the same time, near-field displacement may not be well recorved by our fault geometry and meshing techniques, thus we prefer not to invert the detailed near-fault displacements. Three stations (H701, J701 F048) at intermediate distances also present systematic shift by ~0.5 cm. Because we didn't include the NE trending branching (F2) in the mainshock slip model, which locates close to these three stations, co-seismic slip or afterslip that occurred on F2 or its branch structures may influence the displacement fitting for these three stations. In comparison with the large slip that occurred on the main fault traces during the mainshock, we consider these slip as negligible contributions during the mainshock process.

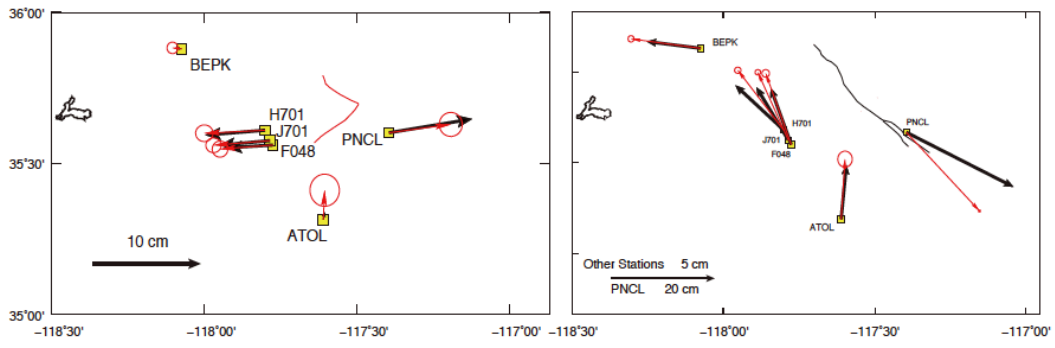

Fig. S17. Comparison between campaign GPS observations (Floyd et al. 2020, red arrows) and forward prediction of co-seismic slip models (black arrows). Foreshock and mainshock co-seismic displacements are plotted in the left and right panels, respectively.

6. Strainmeter data analysis

Strainmeter stations are operated by GAGE facility and the data are made available by UNAVCO (https://www.unavco.org/highlights/2019/ridgecrest.html). Time-series of three plane strain tensor components are provided, i.e. the Eee+Enn, Eee-Enn, and Ene components, together with the solid earth tide strain tensors and barometric stresses provided for the same components. We remove the solid earth tides from the original time-series and perform a running median within 1 minute time window to remove spikes associated with dynamic strains of regional earthquakes. Three strain stations locate near the mainshock, e.g. B0916, B0917, B0921, with B0916 and B0921 closer to F1 and F2, respectively. To investigate the slow-slip slip evolution following the M_W 6.4 foreshock, we focused on these two stations. Original and processed strain time series are plotted in Fig. S18 for evaluation of noise level before and after the foreshock.

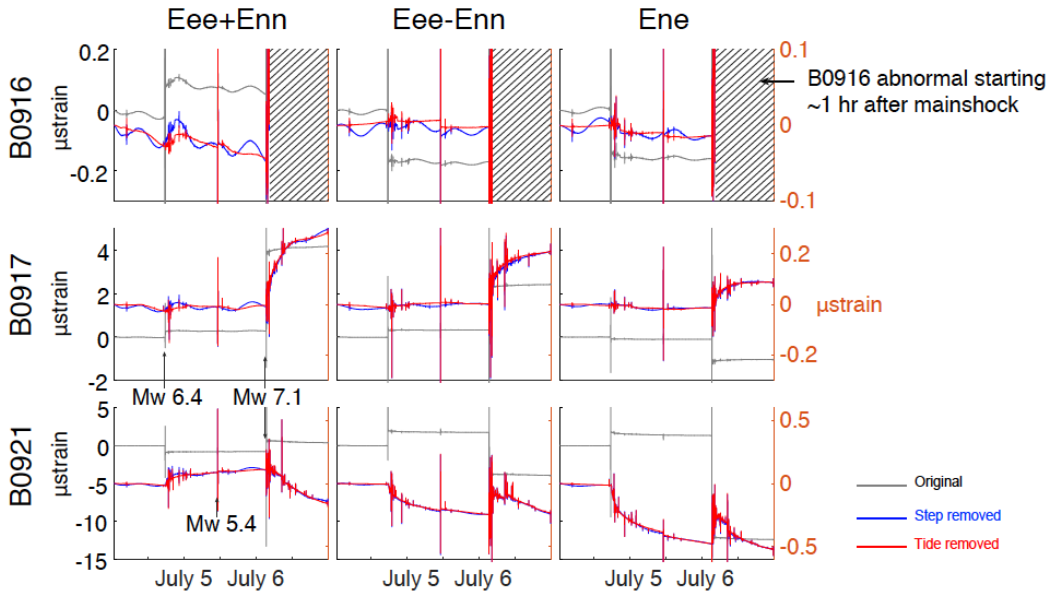

508

509 **Fig. S18.** Strain time series from July 4th 00:00:00 to July 6th 23:59:59. Components
510 of strain tensors Eee+Enn, Eee-Enn, and Ene are plotted in each column, and strains
511 time-series of three stations are plotted in each row. Observed strain time-series are
512 plotted in gray, step-removed (M_W 6.4 foreshock and mainshock) time series are
513 plotted in blue, and tide removed time series are plotted in red, respectively.

514

515

516 We cut the strain time series between July 4, 18:00:00 and July 6, 02:00:00 to
517 investigate the slip processes following the M_W 6.4 foreshock. Processed strain time
518 series of station B0916 and B0921 are plotted in Fig. S19. Abnormal ramps are found
519 in station B0916 starting at July 4, 20:38 and July 5, 16:15. These ramps start
520 abnormally with a logarithmic shape, in contrast to earthquake-related strain jumps,
521 which always initiate with dynamic waves (spikes). We compared the detected
522 catalog and nearby seismic stations and did not find earthquakes whose location and
523 initial time are associated with these ramps. These ramps are not evident in other
524 stations besides B0916. We consider them as localized aseismic signals or instrument
525 noise, which is not related to slip on the foreshock plane. Thus we remove these
526 ramps for further analysis.

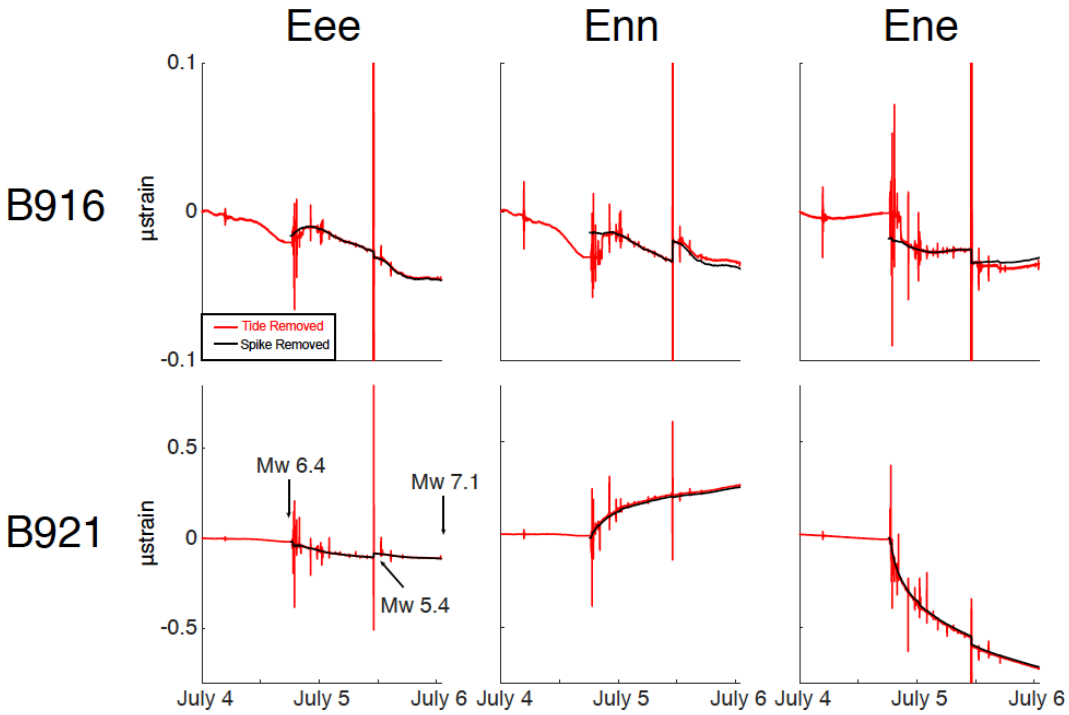

Fig. S19. Strainmeter time series. Data are plotted for each station of B0916 and B0921 in each row and for each component in each column. De-tided strains are plotted as red curves. The initial-time of abnormal ramps of station B0916 is marked in the top panels. Abnormal ramps and spikes are removed from the de-tided signals and plotted as black curves. These strain time series are used to invert for slip processes following the M_W 6.4 foreshock.

7. Inversion and modeling of M_W 5.4 event using strainmeter data

A step of strain change occurred around 11:00:00, July 5, which appears to be related to the M_W 5.4 foreshock. We measure the changes in strain time-series between 10:59:00 and 11:17:00 from two strain stations to derive the co-seismic strain tensors of the M_W 5.4 event (Fig. S20). We then take the focal mechanism and location of the M_W 5.4 foreshock from USGS (lat/lon/dep: 35.7/-117.575°/7.0km, strike/dip/rake 312°/81°/-157°, M_W = 5.4), and assume stress drop of 3 Mpa and shear modulus of 3 x 10^{10} Pa to convert the seismic moment to slip on a planar fault (1.6 x1.6 km^2). Choosing a different fault dimension would not have a significant influence on the strain calculation. The strain tensors at the three regional stations are then calculated using the Okada code (Okada, 1992). The synthetic strain tensors at the three sites appear to be consistent with the observations (Fig. S20).

We take the geometry of a fault plane (F1) derived from the foreshocks to calculate the Green's functions and invert the strainmeter data for the seismic moment release on fault using a linear inversion. The inversion result recovers an M_W 5.39 event at the northwest corner of F1, which is consistent with the location and magnitude of the M_W 5.4 foreshock. These test results suggest that the strain tensor observations could be used to invert for slip on the foreshock fault planes.

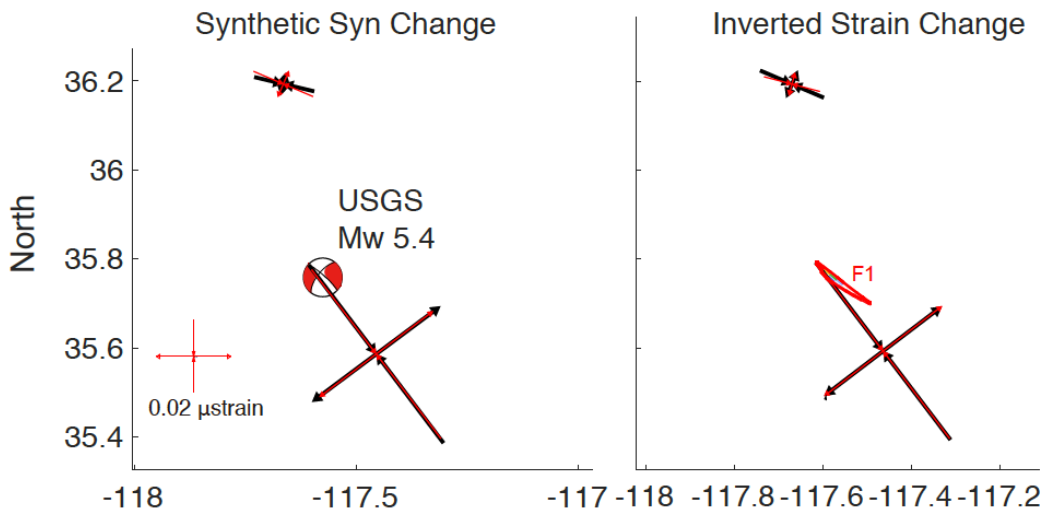

Fig. S20. Strainmeter data fitting result. Left panel: map view of plane strain data fitting for two stations. Synthetic strain tensors are computed using the USGS focal mechanism solution. Observed and synthetic strain tensors are plotted as black and red arrows, respectively. Right panel: strainmeter data inversion result. The observed and inverted strain tensors at the two sites by the inversion model of the M_W 5.37 event are plotted using the same legend as the left panel. The surface projection of F1 is also plotted in red.

8. Post-seismic observations

GNSS postseismic displacement time series

We also use the daily solution of regional GNSS solutions to solve for post-seismic displacements. The original GNSS time series includes tectonic loading (linear trend), co-seismic displacements (Heaviside function) and post-seismic displacements (logarithmic). We construct three types of time series, i.e. linear trend, Heaviside, and logarithmic functions plus a constant, and perform a linear inversion to fit the original GNSS time series. The predictions of a linear trend and the Heaviside functions are then removed from the original GNSS time series to recover the post-seismic displacements. Data for the earthquake days, i.e. July 4 and July 6 are removed from the original dataset, because it requires special treatment of the signals before and after the earthquakes to recover the ground displacements, which is not accounted for

in daily solutions. The processed GNSS postseismic displacements are plotted in Fig. S21.

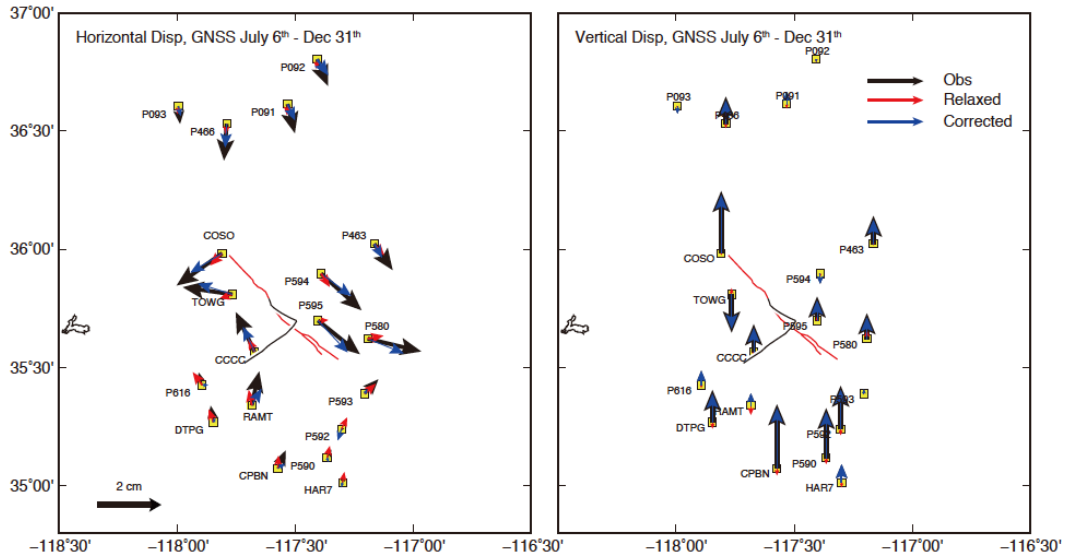

Fig. S21. GNSS postseismic displacements. Stations are plotted as yellow filled squares. Total postseismic displacements (between July 6 and December 31) of observed, relaxed (explained in the following section) and corrected GNSS recordings are plotted as black, red, and blue vectors, respectively. Lateral and vertical displacements are plotted in the left and right panel, respectively. Mainshock and M_W 6.4 fault traces are plotted as black and red curves, respectively.

SAR time series

We retrieve the postseismic deformation in the aftermath of the Ridgecrest earthquake using SAR data acquired by Sentinel-1 satellites from the European Space Agency. The earliest postseismic data in descending track (D071) was acquired on Jul. 16, 2019, just 12 days after the mainshock. The last data we used in track D071 was acquired on Feb. 11th, 2020, so that the postseismic time-series could be formed with 34 SAR acquisitions, with the average temporal sampling of the post-seismic signals being ~6 days (Table 1). The ascending track (A064) data cover the postseismic period from July 10, 2019 to September 2, 2020, and 63 acquistions were collected for deformatiuon analysis. The descending track data (D071) covering the whole co-seismic areas with two consecutive TOPS (Terrain Observation by Progressive Scans) mode SAR frames, starting from the Los

Angeles coast to the Ridgecrest region, hit by both the foreshock and the mainshock, so that any possible signals across the San Andreas fault, Garlock fault, and the seismogenic faults of the Ridgecrest event could be captured following the Ridgecrest earthquake sequence. In contrast, 3-frame data cover the same areas in ascending track (A064), which extend a bit further to the south than the descending track along coast region.

We use Gamma software (Strozzi et al.,2008) for conventional InSAR processing of the SAR data, with a multi-look factor of 8 in range and 2 in azimuth directions for TOPS data co-registration, and the 1-arc-second SRTM DEM (Farr et al., 2007) is used for DEM phase removal and DEM-assistant co-registration. We pick the September 8th, 2019 SAR data as reference date for descending track D071 and February 11, 2020 SAR data for ascending track A064, and form 33 and 62 interferograms respectively for time-series analysis.. It is trivial to select other acquisitions as the reference, given the perfect coherence of the study area due to dry conditions and little vegetation coverage in that areas. After the co-registration process, we deramp all of the data to remove high-frequency fringes in the TOPS SAR data bursts. Then we form full resolution interferograms using the deramped data. We then apply the Stanford Method for Persistent Scatter (StaMPS) matlab code (Hooper et al., 2004) for persistent scatterer identification with an amplitude dispersion threshold of 0.4. High-density point targets (persistent scatterers) were identified as phase stable points and we obtain 636872 and 762279 points in both ascending and descending tracks respectively by applying a downsampling of 300 m spacing. However, the interferograms over the studied areas are also heavily affected by atmospheric propagation errors. This could be due to complicated water vapor distributions around the coastal region of South California. Due to complicated fringe patterns of the entire interferograms, we focus on the earthquake-stricken areas around the seismogenic faults of the Ridgecrest event, for a region large enough to cover the afterslip and transient viscoelastic relaxation affected areas. We, therefore, use these data sets to do afterslip inversion and transient viscoelastic signal estimates. In order to reduce the long-wavelength errors due to inaccuracy of orbit data and the atmospheric propagation errors, we first eliminate a linear phase ramp from the time-series data and then apply two kinds of methods to suppress the atmospheric noise. The first is to use the ERA5 (available at https://www.ecmwf.int) model from

638 the European Centre for Medium-Range Weather Forecasts (ECMWF) to estimate the
639 SAR signal zenith delay using a StaMPS companion software package called TRAIN
640 (Bekaert et al., 2015). However, significant atmospheric delays are still visble from
641 the data. We alternatively apply a spatio-temporal filter integrated with StaMPS
642 software to suppress possible atmoshpheirc errors. After a number of tests, we found a
643 spatial wavelength of 300 m and a temporal wavelength of 30 days could be applied
644 to effectively reduce the atmospheric noise while not weakening the real ground
645 deformation. Finally, we choose a relatively stable point located at [-118° E, 35.60°
646 N] to produce the final time-series deformation map and average velocity field. SAR
647 time series are downsampled with the same grid as co-seismic sampling points. A
648 total of 1373 pixels are used in inversion. 24 and 27 frames from ascending and
649 descending orbits are used in inversion. Details of SAR time series information are
650 listed in Table S4
651

Ascending Orbit A064				Descending Orbit D071			
No	**Date**	**Baseline**	**Sigma**	**No**	**Date**	**Baseline**	**Sigma**
1	10-Jul-2019	-75	11.550	1	16-Jul-2019	36	10.448
2	16-Jul-2019	25	11.268	2	28-Jul-2019	-27	8.827
3	22-Jul-2019	-24	10.302	3	09-Aug-2019	3	7.695
4	28-Jul-2019	-38	10.702	4	15-Aug-2019	45	8.008
5	03-Aug-2019	81	12.561	5	21-Aug-2019	18	7.547
6	09-Aug-2019	-107	12.001	6	27-Aug-2019	-35	6.624
7	15-Aug-2019	49	10.760	7	02-Sep-2019	-8	8.001
8	27-Aug-2019	-15	9.547	8	08-Sep-2019	0	7.909
9	02-Sep-2019	27	9.806	9	14-Sep-2019	-32	6.200
10	08-Sep-2019	-95	11.605	10	20-Sep-2019	-13	6.147
11	26-Sep-2019	-45	9.322	11	26-Sep-2019	78	8.466
12	02-Oct-2019	-33	9.062	12	02-Oct-2019	30	6.509
13	08-Oct-2019	-40	9.322	13	08-Oct-2019	-27	5.932
14	14-Oct-2019	68	10.326	14	14-Oct-2019	20	6.558
15	20-Oct-2019	-4	9.251	15	20-Oct-2019	-55	6.213
16	26-Oct-2019	75	10.271	16	26-Oct-2019	2	6.312
17	01-Nov-2019	4	9.008	17	01-Nov-2019	36	7.306
18	07-Nov-2019	12	8.954	18	07-Nov-2019	-46	6.372
19	13-Nov-2019	29	9.096	19	13-Nov-2019	78	7.869
20	19-Nov-2019	-72	10.423	20	19-Nov-2019	38	7.683
21	25-Nov-2019	81	12.463	21	25-Nov-2019	66	10.146
22	01-Dec-2019	13	25.152	22	01-Dec-2019	60	27.751
23	07-Dec-2019	42	16.722	23	07-Dec-2019	-24	17.404
24	13-Dec-2019	59	14.225	24	13-Dec-2019	106	10.856
				25	19-Dec-2019	-18	10.723
				26	25-Dec-2019	104	17.416
				27	31-Dec-2019	28	22.775

Table S4. Information for SAR time series, including SAR data acquiring dates, perpendicular baselines relative to the reference date and noise level of each date in degrees. (a) SAR data for descending track D071. (b) SAR data for ascending track A064.

9. Visco-elastic relaxation correction for InSAR postseismic time series

Viscous relaxation also contributes to the post-seismic ground deformation. The viscous relaxation produces most contributions in the far-field and presents a similar sense of motion as deep afterslip. The viscous relaxation related displacement fields may be interpreted as deep slip if they are not corrected properly. The visco-elastic behavior of the ECSZ was investigated by Liu et al. (2020), which used long-term post-seismic deformation fields of several large events to invert for the visco-elastic structure of the ECSZ. For the several investigated cases, Liu et al. (2020) obtained a temporal varying upper mantle viscosity, which changes from 6-8$\times10^{17}$ Pas in the first month to 8-20$\times10^{18}$ Pas in 18 years. To simply correct for the visco-elastic relaxation in the first several months, we used the short term estimated relaxation value of the ECSZ to correct for the viscous-elastic relaxation. A preferred visco-elastic model is composed of 11 layers, the elastic parameter of which is consistent with the velocity model. Two sets of visco-elastic parameters are used to parameterize the crustal and upper-mantle rheology. The detailed parameters are listed in Table S5.

Table S5. Visco-elastic structure used to model post-seismic viscous relaxation.

Depth (km)	η_1	η_2	α
0-32	1×10^{24}	1×10^{24}	0.67
32-	1×10^{18}	1×10^{21}	0.67

η_1 and η_2 denotes short term and long term viscosity of a Burgers body. α is the ratio between the effective and unrelaxed shear modulus.

We used a 1-D layer numerical code to calculate the Green's function for relaxation displacements due to slip on each subfault (Wang et al. 2008). We then scale the Green's function by co-seismic slip of each subfault and stack over the fault planes to calculate the relaxed displacement field of the mainshock. The relaxed displacement field is then interpolated at the locations of GNSS stations and SAR time series pixels to estimate the relaxed displacement field at each observation point, as shown in Figs. S21 and S23. The relaxed displacement field is then removed from the observations to recover the contribution of afterslip.

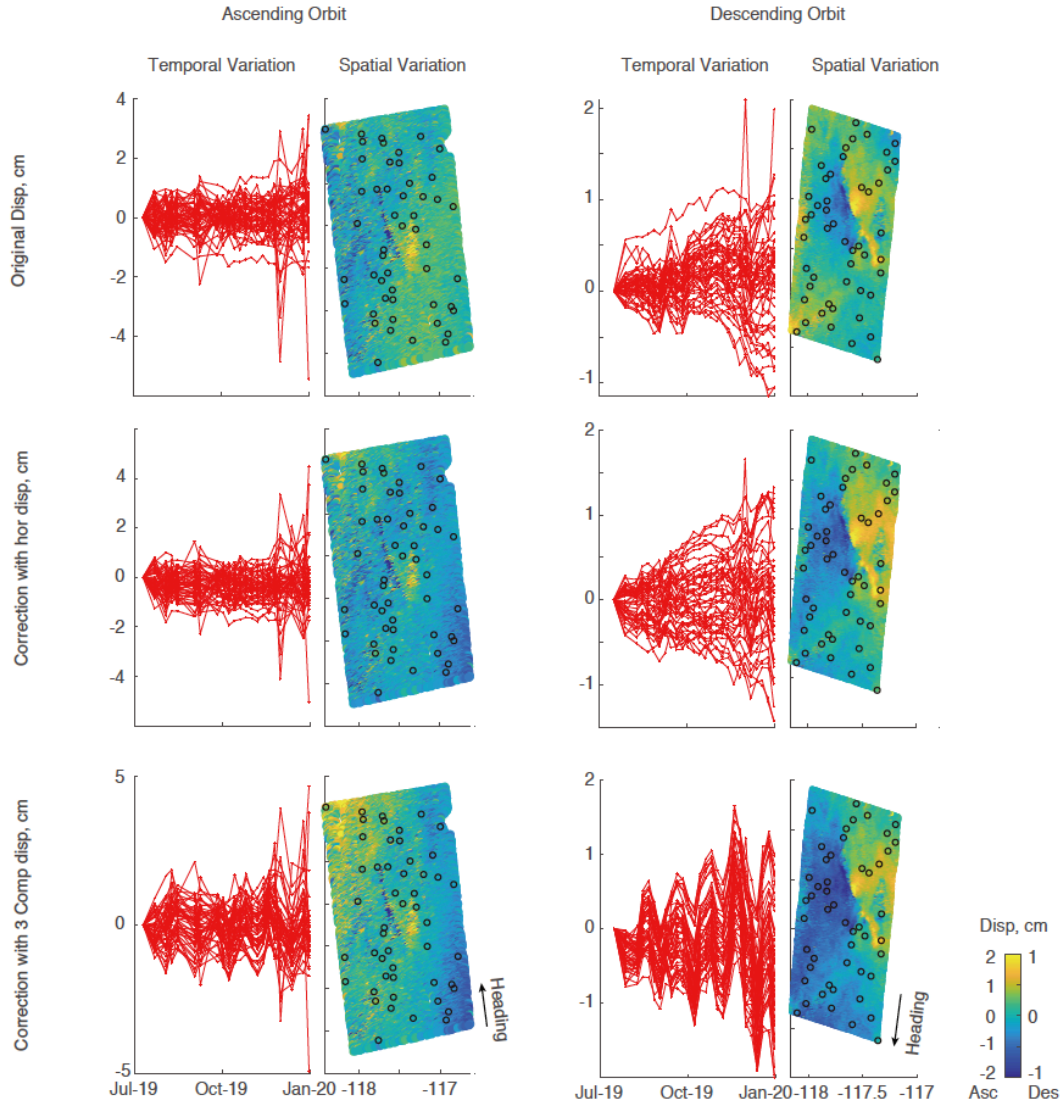

688

689 **Fig. S22.** SAR postseismic time series data. Temporal and spatial variations of SAR
690 time series are plotted in the left and right columns of each sub-figure, respectively.
691 Original and corrected SAR time series with horizontal and 3-component GNSS
692 displacements are plotted in the second and third row panels. In the column plots of
693 each orbit, the left panel shows temporal variations of time series from 50 example
694 pixels. The right panel shows the spatial distribution of the dynamic range of each
695 pixel. The example points used to plot the time series on the left are marked by black
696 circles.

697

698

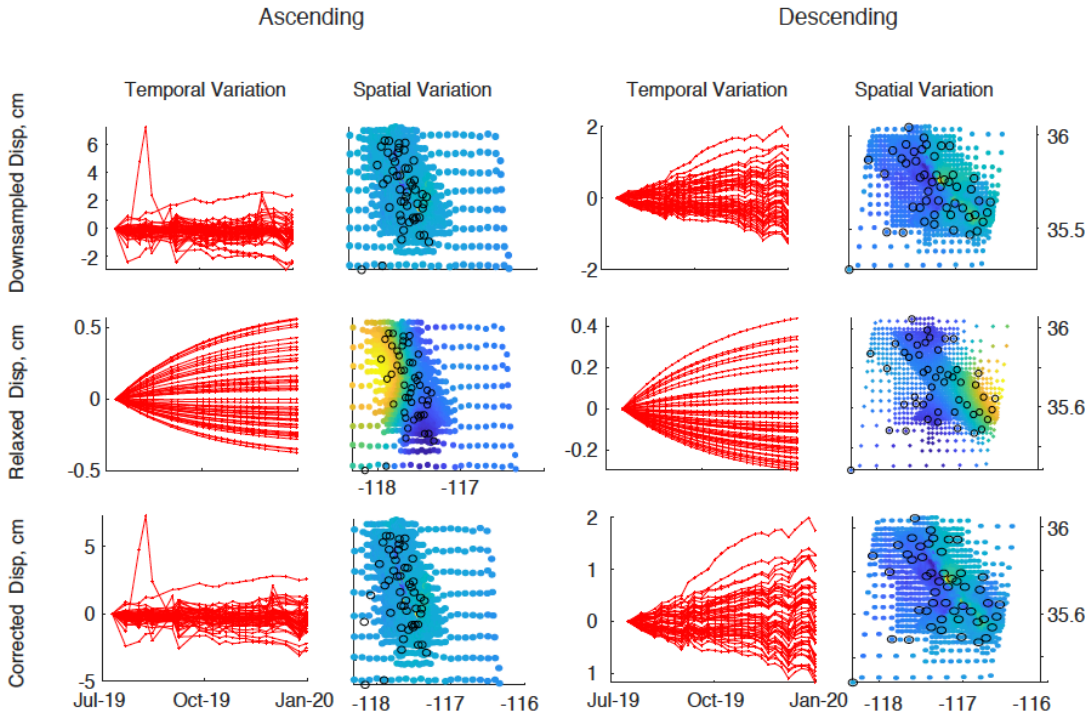

Fig. S23. SAR time series data and relaxation corrections. Downsampled SAR time series, the temporal evolution of relaxed displacements, and corrected SAR time series are plotted in the rows using the same convention as in Figure S24.

10. Full time series inversion algorithm

We develop an inversion algorithm, which linearizes the inversion problem using an assumed slip evolution function. This linear inversion algorithm can use different types of time series, e.g. strainmeter, GNSS, and SAR time series, with different sample rates or time coverage in a joint inversion scheme. We use this full time series inversion (FTI) algorithm to invert for the afterslip following the M_W 6.4 foreshock using strain meter time series and invert for afterslip following the mainshock using GNSS and SAR time series. The FTI inversion algorithm is described as follows.

We assume that slow-slip on the fault plane, e.g. steady creep, afterslip or slow-slip events, involves quasi-static processes; thus the inertial term in the wave equation can be neglected. The quasi-static approximation essentially assumes the medium is in a stress balance at each time epoch, though the source is slowly moving. With this assumption, the displacement at location x can be calculated by:

$$\boldsymbol{D}(\boldsymbol{x},\boldsymbol{t}) = \iint_{\boldsymbol{x}'} \boldsymbol{G}(\boldsymbol{x}',\boldsymbol{x})\,\boldsymbol{S}(\boldsymbol{x}',\boldsymbol{t}) \qquad \text{(S2)}$$

Where $\boldsymbol{x}'$ is the source location, $\boldsymbol{G}(\boldsymbol{x}',\boldsymbol{x})$ is the Green's function of displacement/strain at location $\boldsymbol{x}$ produced by a source $\boldsymbol{S}(\boldsymbol{x}',\boldsymbol{t})$ at location $\boldsymbol{x}'$ and time t. The integration is made over all fault planes. The quasi-static approximation relates displacement at time t to the source history at the same time, which neglects the propagation effect of the displacement field. Therefore the displacement field and source terms share similar evolution functions under this approximation. Discretely, the spatial integration can be replaced by a summation of all sub-faults over a presumed fault plane:

$$\boldsymbol{D_{kl}}(\boldsymbol{t}) = \sum_{\boldsymbol{i=1}}^{\boldsymbol{i0}} \sum_{\boldsymbol{j=1}}^{\boldsymbol{2}} \boldsymbol{G_{ijkl}} \boldsymbol{S_{ij}}(\boldsymbol{t}) \qquad \text{(S3)}$$

Where i and j denote the j^{th} component slip on the i^{th} subfault, k and l denotes the k^{th} displacement/strain component of the l^{th} location. If the slip evolution over the whole fault plane is uniform, but the slip amounts are different, $S_i(t)$ can be simplified as $m_i S_0(t)$. The uniform evolution $S_0(t)$ for all subfaults can be extracted out of the summation and the displacement can be calculated by:

$$\boldsymbol{D_{kl}}(\boldsymbol{t}) = \sum_{\boldsymbol{i=1}}^{\boldsymbol{i0}} \sum_{\boldsymbol{j=1}}^{\boldsymbol{2}} \boldsymbol{G_{ijk}} \boldsymbol{m_{ij}} \boldsymbol{S_0(t)} \qquad \text{(S4)}$$

In most useful time series observations, the sampling time is known, thus if we assume an analog form of $S_0(t)$, its amplitude can be calculated at the sampling time and the right side of equation S4 becomes a linear operation of m_{ij}. We use static Green's functions from the point source (G_{ijk}) and source evolution function $S_0(t)$ to calculate temporal varying Green's function by :

$$\boldsymbol{G_{ijklt}} = \boldsymbol{G_{ijkl}} * \boldsymbol{S_0}(\boldsymbol{t}) \qquad \text{(S5)}$$

When substituting equation S4 to equation S3, we obtain:

$$\boldsymbol{D_{klt}} = \sum_{\boldsymbol{i=1}}^{\boldsymbol{i0}} \sum_{\boldsymbol{j=1}}^{\boldsymbol{2}} \boldsymbol{G_{ijklt}} \boldsymbol{m_{ij}} \qquad \text{(S6)}$$

Where t in equation S6 is a time domain index instead of a variable. Note that equation S6 is a standard linear form and parameters m_{ij} can be inverted with a linear inversion algorithm, so that equation S6 can be written as

$$\boldsymbol{Gm} = \boldsymbol{d} \qquad \text{(S7)}$$

where G is a 2D matrix, which sorts each sample point (t), component (l) and station (k) in the column dimension and sorts the slip direction (j) on each subfault (i) in the row dimension. For afterslip the analytic form of $S_0(t)$ can be parameterized with an empirical logarithmic function:

$$\boldsymbol{S(t) = S(t, t_0, \tau)} = \begin{cases} \boldsymbol{0}, & \boldsymbol{for\ t < t_0} \\ \boldsymbol{log(\frac{t-t_0}{\tau} + 1)}, & \boldsymbol{for\ t > t_0} \end{cases} \qquad \textbf{(S8)}$$

where $\boldsymbol{t_0}$ is the earthquake initiation time and $\boldsymbol{\tau}$ is the characteristic releasing time. For afterslip inversions, the earthquake initial time is known and the characteristic releasing time can be obtained by a grid search method: we assume different characteristic times to perform linear inversion and select the preferred value from the residual curve similar to Vr determination in the multi-time-window inversion. A similar strategy of using assumed logarithmic source time functions to linearize the time series inversion was initially proposed by Liu et al., (2019), which combines a step function and logarithmic function to perform joint inversion of co-seismic and post-seismic slip using SAR time series.

The FTI inversion scheme allows exploring slow-slip processes with different initial time and decay time. Although equations S3-S8 only present the FTI inversion method using a single slip evolution function, including extra evolution functions simply involves laterally concatenating the G matrix, and equation S7 can be transformed to :

$$\boldsymbol{G * m} = [\boldsymbol{G(t_{0i}, \tau_i)}, \boldsymbol{G(t_{02}, \tau_2)}, \dots] \begin{bmatrix} \boldsymbol{m_1} \\ \boldsymbol{m_2} \\ \vdots \end{bmatrix} = \boldsymbol{d} \qquad \text{(S9)}$$

where $\boldsymbol{G}(\boldsymbol{t_{0i}}, \boldsymbol{\tau_i})$ represents the Green's function matrix produced by the i^{th} process, whose slip function is calculated by initial time $\boldsymbol{t_{0i}}$ and releasing time $\boldsymbol{\tau_i}$. m_i is the slip model associated with the i^{th} process. The i^{th} evolution function is not necessarily a slow-slip process, but can also involve co-seismic steps or transient slip. Parameterizing the slip evolution function with co-seismic and post-seismic functions returns to the form presented by Liu and Xu (2019). Another empirical strategy to design $S_0(t)$ is to average GNSS time series with significant afterslip signal, and then interpolate $S_0(t)$ for other types of data. In this work, we do not adopt this strategy because errors of averaged GNSS time series result in large uncertainty in the interpretation of early afterslip.

11. Afterslip inversion and data fitting

While introducing a presumed source evolution function of full time series inversion, we also adopt other corrections to achieve stable and precise inversion results. These corrections includes initial displacement correction and orbit corrections to the SAR time series, which are described as following.

1. Initial displacement correction

SAR time series are converted to relative motion with respect to the first frame, thus the displacement of the 1st frame is zero. Synthetic ground displacements are generated at each frame and the initial displacement of the 1st frame is subtracted from other frames to recover relative ground displacements. The relative displacement operation reduced the complexity to estimate displacement field of the 1st frame, however, such configuration essentially assumes the error of the 1st frame is zero, though each frame is supposed to include similar level of noise. Subtracting the 1st frame data from other frames also add the error of the 1st frame to the other frames. This "systematic error" in all frames probably will bias the inversion results. Thus we adopt initial displacement correction in the inversion matrix, and reconstruct the inversion matrix and slip model set up as:

$$\boldsymbol{G_{mat}} = \left[\boldsymbol{G_{slip}},\ \boldsymbol{G_{ini}}\right] \quad \textbf{and} \quad \boldsymbol{m} = \begin{bmatrix} \boldsymbol{m_{slip}} \\ \boldsymbol{m_{ini}} \end{bmatrix} \qquad \textbf{(S10)}$$

Where G_{slip} is the matrix built up by the Green's function of sub-fault slip. m_{ini} is the parameter depicting the error of the first frame, and the m_{ini_i} is the initial frame error of the i^{th} pixel. G_{ini}*m_{ini} is the initial displacement correction applied to all pixels. There are N (pixel number) corrections applied to the time series of each pixel, thus the dimension of G_{ini} is (data dimension * pixel number). To build up the i^{th} column of G_{ini} , we set the elements of all frames related to the i^{th} pixel as ones and set the rest of the elements to be zero. Such a setting adopts a constant displacement change of all time samples of one pixel. The inverted initial correction m_{ini} has a dimension of the pixel number.

2. Ramp correction of each SAR frame

Though linear ramps of the SAR time series are removed through the comparison with GNSS data, such ramp signal can also be inverted simultaneously with the slip parameters. A dense sampling of all SAR pixels reduces the errors of ramp signal correction using a few GNSS stations. The performance of ramp correction is most significant when 3 component GNSS data were initially used for correction, which introduces large errors from vertical displacements (Fig. S22). Such correction resembles the method used for co-seismic inversion except that a set of ramp parameters is estimated for each frame of SAR time series. A set of ramp correction can be estimated with constant (1 parameter), linear ramp (3 parameters) and quadratic ramp (6 parameters). In the afterslip inversion work of the Ridgecrest earthquake, we found constant correction to each frame is enough to correct the baseline shifts, though adding extra ramp parameters does not influence the inverted slip model.

We assume the SAR data are fitted by ground displacement, initial correction and ramp corrections, which can be expressed as the following equation:

$$\boldsymbol{G_{slip}}\times\boldsymbol{m_{slip}} + \boldsymbol{G_{ini}}\times\boldsymbol{m_{ini}} + \boldsymbol{G_{ramp}}\times\boldsymbol{m_{ramp}} = \boldsymbol{d} \quad \textbf{(S11)}$$

or in linear form of matrix product as $G_{mat} \times m = d$, where

$$\boldsymbol{G_{mat}} = [\boldsymbol{G_{slip}}, \boldsymbol{G_{ini}}, \boldsymbol{G_{ramp}}] \quad \textbf{and} \quad \boldsymbol{m} = \begin{bmatrix} \boldsymbol{m_{slip}} \\ \boldsymbol{m_{ini}} \\ \boldsymbol{m_{ramp}} \end{bmatrix}$$

3. Smoothing damp and characteristic releasing time

Hyper-parameters of FTI include characteristic decay time and Laplacian smoothing parameters. We determine the optimized hyper-parameters by residual trade-off curves (Figure S26 and S27).

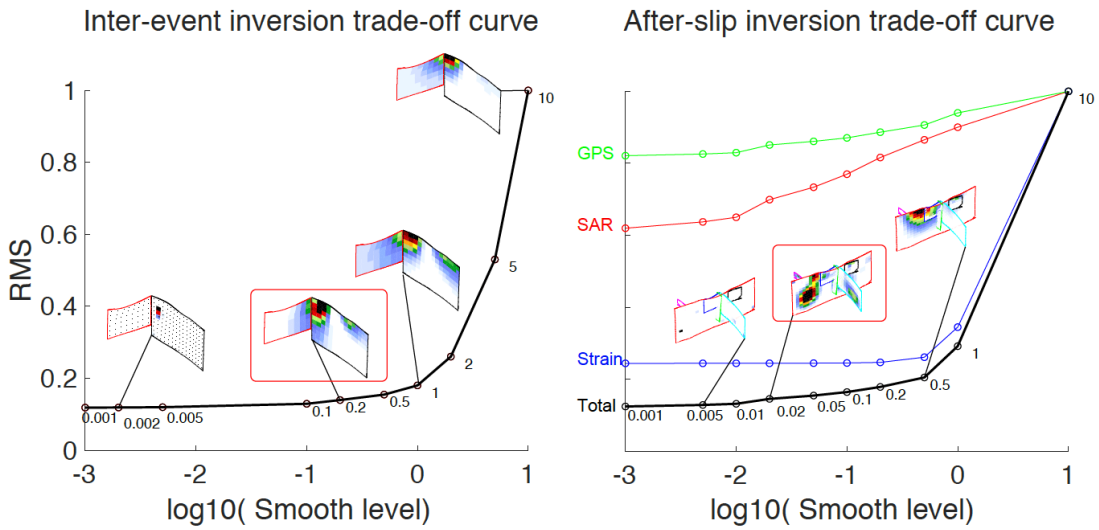

Fig. S24. Trade-off between smooth level and residual RMS. The smooth level versus residual RMS curves of the afterslip inversions following the M_W 6.4 foreshock and the mainshock are plotted in the left and right panels, respectively. Examples of associated slip models are plotted. The preferred slip models are marked by red boxes.

For the afterslip inversion, although the total RMS shows a turning point near weighting level between 0.5 and 1, such shapes are mostly controlled by the strainmeter data, which has low spatial resolution. The turning point of the SAR and GNSS data occurs near smooth weighting of 0.02, which is the preferred smoothing parameter finally used to determine afterslip models.

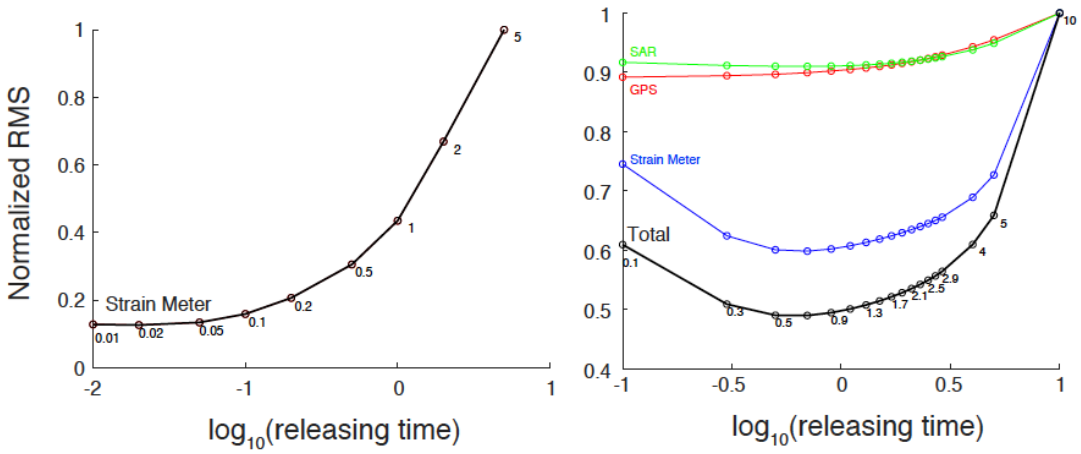

Fig. S25. Trade-off between characteristic decay time and residual RMS. The characteristic decay time versus residual RMS of the afterslip models are plotted in the left and right panels, respectively. For the afterslip model, RMS curves of the GPS, SAR, strainmeter and total data are plotted as red, green, blue and black curves, respectively.

For the foreshock period, we choose the characteristicdecay time of $\tau = 0.2$ day, while for the afterslip model, we choose the characteristic decay time of $\tau = 1$ day.

12. Afterslip inversion results

In the afterslip inversion of the Ridgecrest earthquake, we only invert for a constant shift for each frame of the SAR time series. The fits to GNSS and SAR time series of the afterslip model are plotted in Fig. S26-S30.

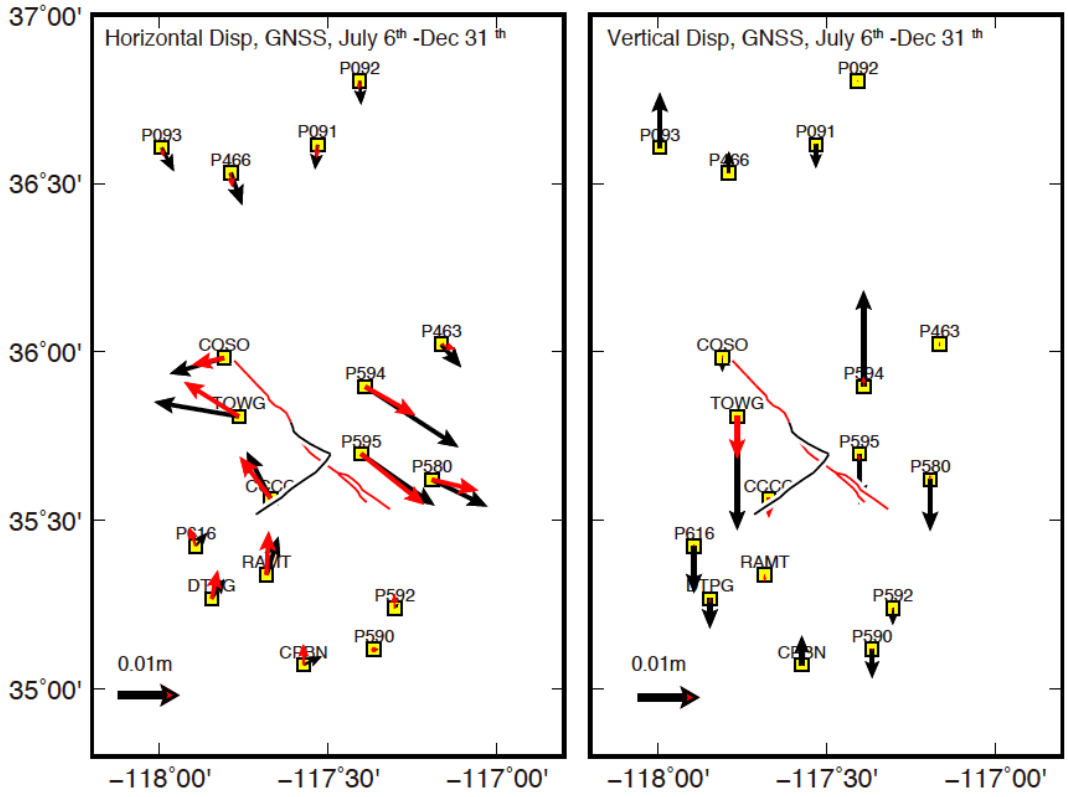

879

880 **Fig. S26.** Static GNSS postseismic data fitting result. Observed and synthetic static
881 ground displacements (June 19 to December 31) are plotted as black and red arrows,
882 respectively. Horizontal and vertical displacements are plotted in the left and right
883 panels, respectively. Mainshock and foreshock traces are plotted as red and black
884 curves, respectively.

885

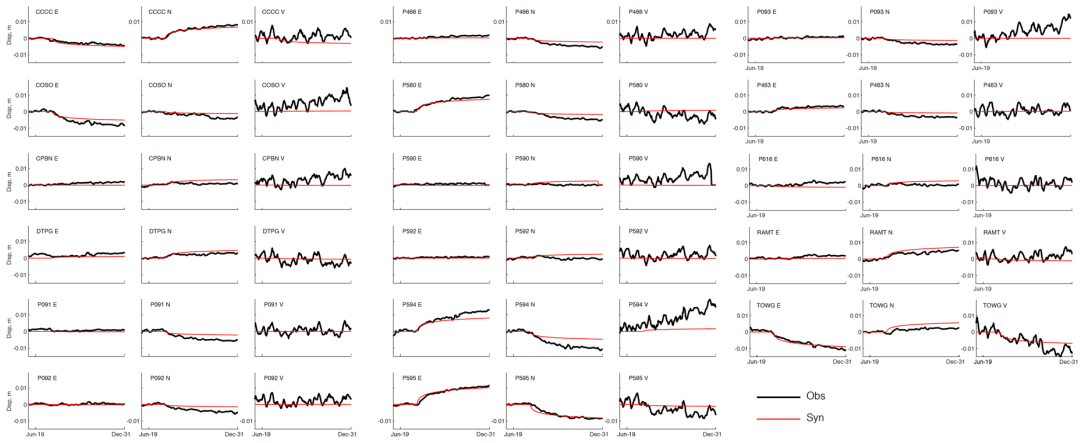

Fig. S27. 3D GNSS time-series data fitting result. Observed and synthetic ground displacement time series are plotted as black and red curves, respectively. Data from each station are plotted in each row. Data of east, north and up components are plotted in 3 columns.

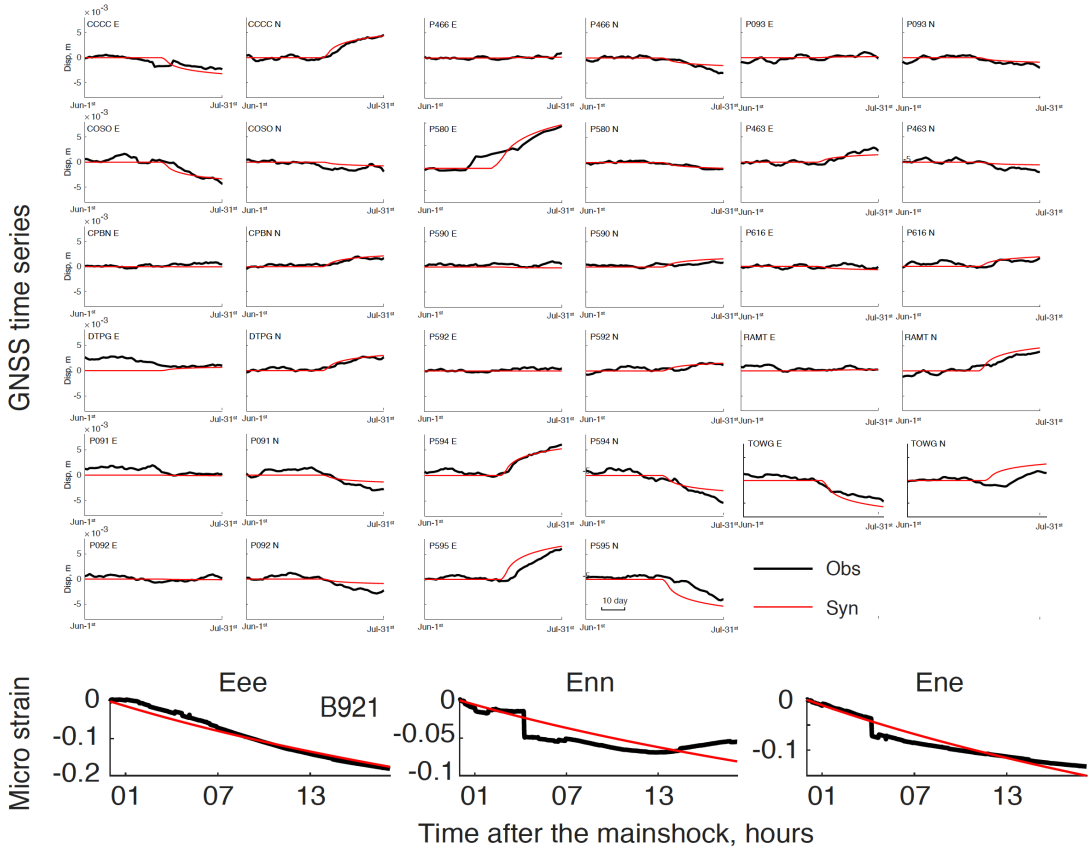

894

895 **Fig. S28.** Deformation data fitting result for the period following the M_W 6.4
896 foreshock. Upper panel: Observed and model predicted GNSS ground displacements
897 are plotted as black and red curves, respectively. Lower panel: Observed and model
898 predicted strainmeter time series are plotted in black and red, respectively.

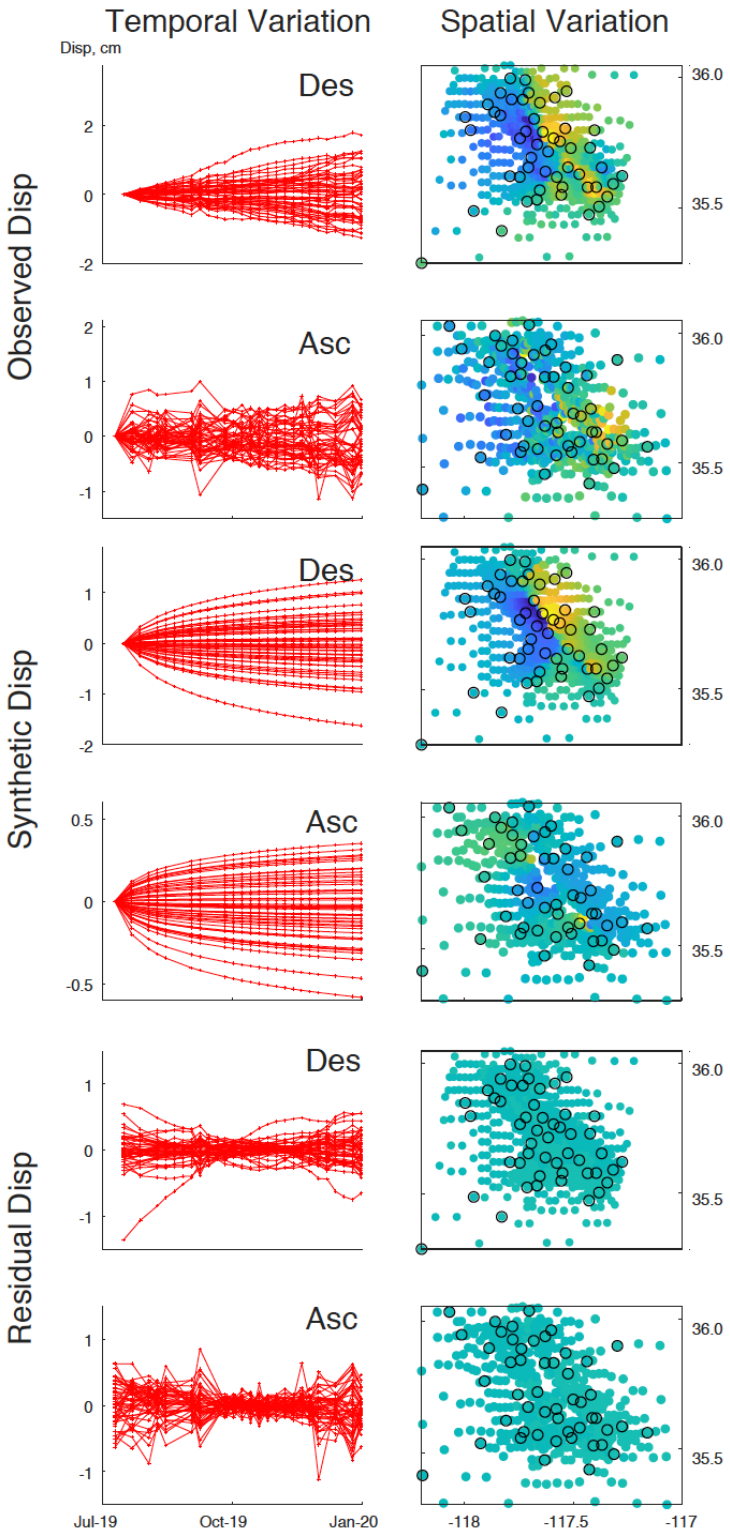

Fig. S29. SAR postseismic data fitting result. Observed, model predicted, and residual SAR time series are plotted in the top, middle, and bottom panels, respectively. Temporal variations of 50 example pixels are plotted in the left column. The spatial variations of all pixels are plotted in the right column.

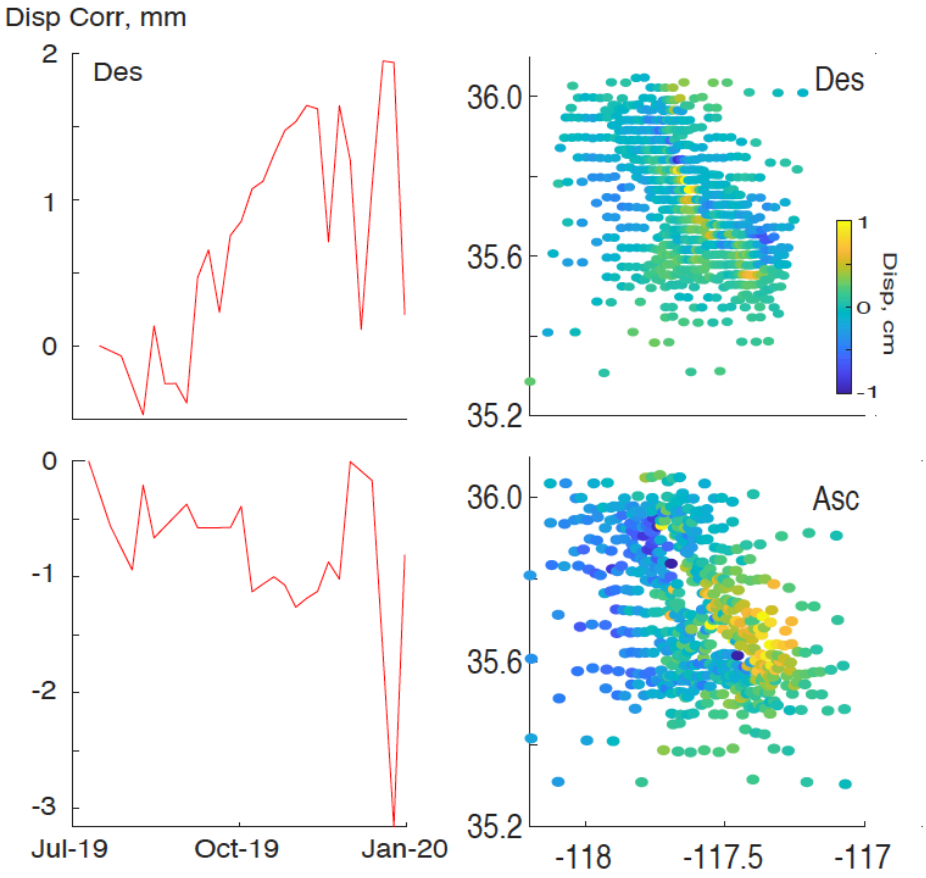

FigS30. Temporal corrections of SAR postseismic data fitting. Temporal evolutions of mean displacement correction of SAR frames are plotted as a red curve in the left panels. Initial displacement corrections for the pixels are plotted in a blue to yellow color scale in the right panels.

1 Afterslip concentrated near rupture ends

We investigate several afterslip models of continental strike-slip events, and find that afterslip is commonly observed to be concentrated at the ends of co-seismic slip, such as following the 2010 M_W 6.9 Yushu Earthquake (Zhang et al., 2016), 2004 M_W 6.0 Parkfield earthquake (Barbot et al., 2009), 2014 M_W 6.1 South Napa earthquake (Floyd et al, 2016; Wei et al., 2015); 2017 M_W 7.0 Kumamoto earthquake (Moore et al., 2017), 1992 Landers earthquake (Liu et al. 2020), and 1999, M_W 7.5 Izmit earthquake (Reilinger et al., 2000). However, afterslip is also found right beneath the co-seismic slip, such as after the 1999 M_W 7.1 Hector Mine earthquake (Liu et al.

2020) and 1997 M_W 7.6 Manyi earthquake (Ryder et al., 2007). Afterslip on the fault plane is controlled by both co-seismic stress changes and frictional properties of the fault plane. Although stress changes are concentrated at the lateral ends and bottom edge of the co-seismic slip, lateral variation of frictional properties may cause afterslip to be released faster on "weak" segments under the same amount of stress loading. These weak segments commonly behave as a stress barrier. For example, the 2016 Kumamoto earthquake was stopped by the Aso volcano, meanwhile, the volcano area presented significant afterslip and visco-elastic deformation (Yue et al. 2017; Moore et al. 2017). The 2019 Ridgecrest earthquake also stopped at the Coso geothermal area (Ross et al. 2019), where the most significant afterslip occurred. This observation resembles that of the 2016 Kumamoto earthquake and reflects the influence of a "barrier" introduced by weak materials.

The afterslip pattern on the orthogonal fault (F2) is intriguing, as it is primarily located on the southwest end of F2 following the M_W 6.4 foreshock (Fig. 6). The foreshock, and afterslip patterns on F2 complement each other, covering the whole fault plane. The foreshocks and aftershocks are mostly located on the margin of co-seismic slip at the transition zone to afterslip. The southwest end of F2 is dominated by shallow and deep afterslip and lacks many seismic events, indicating that this part of the fault is not seismogenic. This phenomenon is opposite to that near the junction of M1 and F2, which is a mingling of slow-slip and seismic events. These differences may be caused by several mechanisms including: fine-scaled seismic asperities embedded in aseismic fault planes; aseismic faults (F2) connected with abundant off-fault fractures; or conditional stable sliding, which presents either seismic or aseismic release depending on stress conditions. Further analysis will require studies involving fault slip dynamics. Slip behavior on these orthogonal structures is important to evaluating seismic hazard of strike-slip fault systems.

2.Afterslip model using two processes

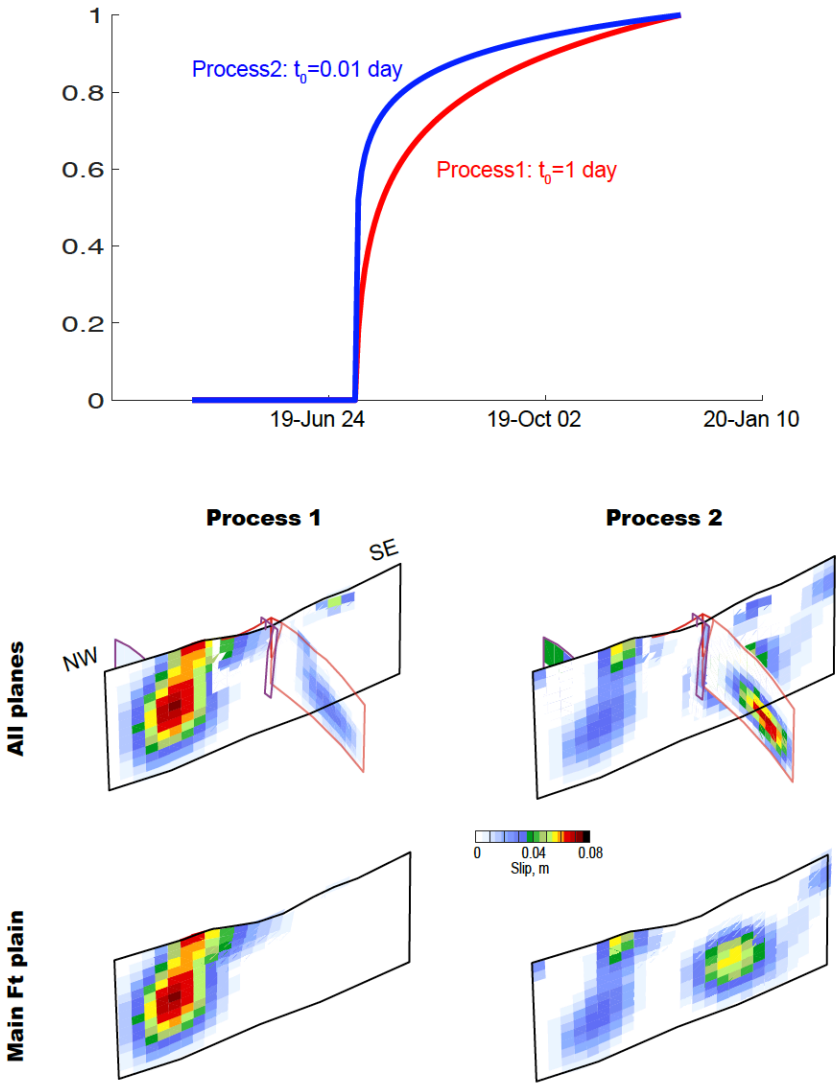

951

952 **Fig. S31** Slip evolution functions of two processes using characteristic releasing time
953 of t_0=1 and 0.01 day are plotted in the top panels. Slip distributions associated with
954 each process are plotted in each row of the bottom panels. Slip on all fault planes is
955 plotted in each row using identical color scales.

956

957 Our analysis demonstrates that the deormation in the Ridgecrest sequence is
958 dominated by seismic and aseismic modes of slip, and the seismic moment release is
959 greater in the early post-seismic stages. We thus explore use of two characteristic
960 decaying processes to invert for the mainshock afterslip processes. The first evolution
961 function uses identical characteristic decay time as the single process afterslip
962 inversion (t_0=1 day), while the second process use a much shorter decay time of
963 t_0=0.01day. The slip patterns associated with each characteristic decay time scale are

plotted in Figure S30. The slip patterns show slight differences, which is most obvious on the main fault plane (M1). The slower process (first process) is more concentrated in the northwestern end, while the shorter process (second process) is more concentrated to in the southeastern part of the main fault plane. The northwest end of the main fault plane is near to a geothermal area and special thermal and pore-pressure conditions may influence the characteristic decay time to be distinct from other fault segments. However, we also notice the faster releasing process only exists when strain meter station (B0921) , which is close to the southeast slip patch, is included in the inversion. Two-process inversions without the strain-meter station shows scattered distribution for the "fast process", since the GPS and SAR timeseries do not have resolution of very early processes. Therefore, we cannot conclude if this difference is caused by real physical properties or data resolution limitations. Exploring this behavior further requires using different types of evolution functions from theoretical or empirical approaches.

References:

Bekaert, D. P. S., Walters, R. J., Wright, T. J., Hooper, A. J., & Parker, D. J. (2015). Statistical comparison of InSAR tropospheric correction techniques. Remote Sensing of Environment, 170, 40-47.

Farr, T. G., Rosen, P. A., Caro, E., Crippen, R., Duren, R., Hensley, S., ... & Seal, D. (2007). The shuttle radar topography mission. Reviews of geophysics, 45(2).

Hartzell S. H. , T. H. Heaton,(1983), inversion of strong ground motion and teleseismic waveform data for the fault rupture history of the 1979 Imperial Valley, California, earthquake. Bulletin of the Seismological Society of America 73, 1553-1583.

Herring T., R. King, S. McClusky,(2010), GAMIT reference manual, release 10.4. Massachusetts Institute of Technology, Cambridge.

Hooper, A., H. Zebker, P. Segall, and B. Kampes, (2004) A new method for measuring deformation on volcanoes and other natural terrains using InSAR persistent scatterers, Geophys. Res. Lett., 31.

Kanamori H. , D. L. Anderson, (1975), Theoretical basis of some empirical relations in seismology. Bull.seism.soc.am 65, 1073-1095.

Okada Y., (1985), Internal deformation due to shear and tensile faults in a half-space. Bulletin of the Seismological Society of America 75, 1018-1040 (1985).

Peng, Z., & Zhao, P. (2009). Migration of early aftershocks following the 2004 Parkfield earthquake. Nature Geoscience, 2(12), 877-881.

Ross, Z. E., White, M. C., Vernon, F. L., & Ben□Zion, Y. (2016). An improved algorithm for real□time S□wave picking with application to the (augmented) ANZA network in Southern California. Bulletin of the Seismological Society of America, 106(5), 2013-2022.

Small, P., Gill, D., Maechling, P. J., Taborda, R., Callaghan, S., Jordan, T. H., ... & Goulet, C. (2017). The SCEC unified community velocity model software framework. Seismological Research Letters, 88(6), 1539-1552.

Strozzi, T., Kouraev, A., Wiesmann, A., Wegmüller, U., Sharov, A., and Werner, C., (2008). Estimation of Arctic glacier motion with satellite L-band SAR data. Remote Sensing of Environment, 112(3), 636-645.

Wang R., F. Lorenzo-Martín, F. Roth, (2006), PSGRN/PSCMP—a new code for calculating co- and post-seismic deformation, geoid and gravity changes based on the viscoelastic-gravitational dislocation theory. Computers & Geosciences 32, 527-541

Waldhauser F., W. L. Ellsworth,(2000), A Double-Difference Earthquake Location Algorithm: Method and Application to the Northern Hayward Fault, California. Bull.seismol.soc.am 90, 1353-1368.

Yokota, Y., Koketsu, K., Fujii, Y., Satake, K., Sakai, S. I., Shinohara, M., & Kanazawa, T. (2011). Joint inversion of strong motion, teleseismic, geodetic, and tsunami datasets for the rupture process of the 2011 Tohoku earthquake. Geophysical Research Letters, 38(7).

Yue, H., Simons, M., Duputel, Z., Jiang, J., Fielding, E., Liang, C., ... & Samsonov, S. V. (2017). Depth varying rupture properties during the 2015 M_W 7.8 Gorkha (Nepal) earthquake. Tectonophysics, 714, 44-54.

Zhu L. and L. A. Rivera, (2002), A note on the dynamic and static displacements from a point source in multilayered media. Geophysical Journal International 148, 619-627.